

Study on the effect of curvature on the aerodynamic properties of drone rotor blades

Riccardo Cagnato

Thesis to obtain the Master of Science Degree in

Aerospace Engineering

Supervisor: Prof. Filipe Szolnoky Ramos Pinto Cunha

Examination Committee

Chairperson: Prof. Fernando José Parracho Lau

Supervisor: Prof. Filipe Szolnoky Ramos Pinto Cunha

Member of the Committee: Prof. João Manuel Gonçalves de Sousa Oliveira

June 2020

I declare that this document is an original work of my own authorship and that it fulfils all the requirements of the Code of Conduct and Good Practices of the *Universidade de Lisboa*.

To my parents, friends, and teachers I met throughout my path

Acknowledgements

I would like to thank professor Filipe Cunha for the possibility he gave me to work on this master thesis at IST Técnico Lisboa. The advices he gave me throughout this period helped me clarify the mind and his support was of great help in all the circumstances I had to face. I want to thank also professor Relógio Ribeiro which gave me great advices regarding the 3D printing, helping me moving the first steps onto this technology, and Nuno Frutuoso for the constant support during the 3D prints. I want to thank Pedro, his help during the development of the test bench calibration as well as for the experimental measurements has been fundamental.

During this period, I had the possibility of appreciating all the teachings I received throughout my academic life, so I would like to thank everyone who made me grow as a student and especially as a person.

Finally, without the constant and relentless support from my family, I would not be at the end of the academic experience, so I want to thank each one of them: my father Stefano, my mother Emanuela, and my two sisters Irene and Arianna.

Abstract

The present work aims to study the effect of a curved leading edge in drone rotors blades, to see whether it can bring performance improvements. Four different rotors are studied, having different blade geometries: the straight blade, the single curved blade, and two totally curved blades, having different tip shapes. The curvature is inserted both in forward and backward direction. At first, a Matlab code implementing the Blade Element Theory and the Blade Element and Momentum theory has been realized. With this tool, it is possible to make comparison between different rotors, changing various geometrical parameters. The obtained results showed good agreement in the analysis of full-scale rotors. The need of taking into consideration 3D and low Reynolds number effects in the aerodynamic parameters led to the development of CFD simulations. The Moving Reference Frame method is the method chosen for the simulations, and a sensitivity study on how various parameters affect results is made. Then, the performances of the four rotors while producing different amounts of thrust are studied, at first in hovering condition, and then in ascending flight conditions. The straight blade appears to be the best configuration for most of the cases, even though there are some particular conditions in which the total curved blade with the tip shape TE2 behaves better. This study also shows that the backward curved blades operate better than the forward curved blades, so a preference in the curvature direction is found. In order to isolate the curvature effect, a tip modification is inserted and analyzed. Different 3D printing methods have been tested to produce the rotors, which are tested experimentally to verify the simulations results.

Keywords

Drone rotors, curvature, Blade Element Theory, Computational fluid dynamics simulations, 3D printing

Resumo

O presente trabalho tem como objetivo estudar o efeito de bordo de ataque curvo nas pás dos rotores de drones, para ver se pode trazer melhorias no desempenho. São estudados quatro rotores diferentes, com diferentes geometrias da pá: a pá reta, a pá curva única e duas pá totalmente curvas, com diferentes formas na ponta da pá. A curvatura é inserida na direção frontal e traseira. Numa primeira fase, um código Matlab implementando a Teoria dos Elementos de pá e a Teoria conjunta elementos de pá/momento linear foi realizado. Com esta ferramenta, é possível fazer comparação entre diferentes rotores, alterando vários parâmetros geométricos. Os resultados obtidos mostraram boa concordância na análise de rotores em escala real. A necessidade de levar em consideração efeitos 3D e baixo número de Reynolds nos parâmetros aerodinâmicos levou ao desenvolvimento de simulações de CFD. O método de referência móvel é o método escolhido para as simulações e é feito um estudo de sensibilidade sobre como vários parâmetros afetam os resultados. Em seguida, são estudadas os desempenhos dos quatro rotores enquanto produzem diferentes quantidades de propulsão, primeiro em condições de pairar e depois em condições de vôo ascendentes. A pá reta parece ser a melhor configuração para a maioria dos casos, embora existam algumas condições particulares em que a pá curva total com a forma de ponta TE2 se comporte melhor. Este estudo também mostra que as pás curvas para trás funcionam melhor que as pás curvas para frente, portanto, é encontrada uma preferência na direção da curvatura. Para isolar o efeito da curvatura, uma modificação da ponta é inserida e analisada. Diferentes métodos de impressão 3D foram testados para produzir os rotores, que são testados experimentalmente para verificar os resultados das simulações.

Palavras-chave

Rotores de Drone, curvatura, Teoria dos Elementos de pá, simulações computacionais de dinâmica de fluidos, impressão 3D

Table of contents

List of figures	xiv
List of tables	xvii
Acronyms	xviii
Symbols	xx
1 Introduction	1
1.1 Overview.....	1
1.1.1 Drones development sectors	1
1.1.2 Analyses of small-scale propellers	2
1.1.3 Analyses of Low Reynolds aerodynamics	3
1.1.4 CFD analysis of rotating systems.....	6
1.2 Objectives	6
1.3 Thesis outline.....	7
2 Theoretical background	8
2.1 Momentum theory	8
2.1.1 Dimensional analysis, thrust and power coefficients.....	10
2.1.2 Power requirements.....	10
2.1.3 Figure of Merit	11
2.1.4 Tip losses.....	11
2.1.5 Axial flight	12
2.2 Blade Element Theory	14
2.2.1 Tip loss factor	17
2.3 Blade Element and Momentum Theory.....	18
2.3.1 Forward flight.....	19
2.3.2 Modeling the inflow	21
3 Matlab implementation of BET and BEMT theories.....	23
3.1 Insertion of the curvature variation in the BEMT	23
3.2 Calculation of aerodynamic properties.....	26
3.3 Method 1	27
3.3.1 Hovering and axial flight.....	27
3.3.2 Forward flight.....	28
3.3.3 Method 1 verification.....	29
3.4 Method 2	30
3.5 BET for small scale propellers.....	32

3.5.1	Interpolation of XFOIL data.....	32
3.5.2	Non-linearity of lift polar	33
3.5.3	Constant Reynolds approach	35
3.5.4	Blade division in segments.....	37
4	CFD simulations	39
4.1	CFD RANS.....	39
4.2	Turbulence models	40
4.3	Solving the boundary layer.....	41
4.4	Flow around rotating objects	43
4.4.1	Moving reference frame.....	43
4.4.2	Equation for a rotating reference frame	44
4.4.3	Moving mesh method	45
4.5	Geometrical model	46
4.6	Mesh.....	49
4.6.1	Mesh topology	50
4.6.2	Mesh quality	50
4.6.3	Mesh method, sizing and inflation.....	52
4.7	Setup	53
4.7.1	Solver and solution controls	53
4.7.2	Spatial discretization	55
4.7.3	Initialization	56
4.7.4	Boundary conditions	57
4.8	Analysis of moving domain dimensions.....	58
4.8.1	Geometry.....	58
4.8.2	Mesh.....	59
4.8.3	Results	60
4.9	Analysis of mesh sensitivity.....	62
5	Results.....	63
5.1	Rotational velocity variation	63
5.2	Untwisted blades-backward curvature	64
5.3	Twisted blades – backward curvature	66
5.4	Untwisted blades – forward curvature	67
5.5	Twisted blades – forward curvature	69
5.6	Comparison between BET and CFD results	71
5.7	Comparison between CFD and experimental results	71
5.8	Axial flight results.....	73
5.9	Tip modification results.....	74

6	Conclusion and future developments	76
6.1	Conclusions.....	76
6.2	Future developments	77
	Bibliography	78
A	Annex	I
A.1	3D printing	I
A.1.1	Fused Deposition Modeling	I
A.1.2	Materials.....	II
A.1.3	Parameters influencing printing.....	IV
A.1.4	Shell and infills	IV
A.1.5	Support material	V
A.1.6	Printing procedure	V
A.1.7	Printing tests	VI
A.1.8	SLA.....	VIII
A.1.9	Printing process.....	IX
A.1.10	Union of the printed blades	XII
A.2	Experimental tests	XII
A.2.1	Experimental results.....	XIII
A.3	CFD extended results	XVI

List of figures

Figure 1.1: Tip vortices and boundary layers merging, taken with PIV technique. Picture taken from [5] .	3
Figure 1.2: Change of aerodynamic performances at various Re number. Image from McMaster [13]	4
Figure 1.3: Formation of the laminar separation bubble. Picture from [10]	4
Figure 1.4: Non linear behavior of the lift coefficient for NACA 0012 airfoil at Re = 50,000. From [20].	5
Figure 2.1: Control volume for the momentum theory. From [24].....	8
Figure 2.2: Power ratio vs climb velocity ratio, as predicted by the momentum theory. From [24]	13
Figure 2.3, plot of the aerodynamic efficiency with respect to the induced-losses coefficient, parametrized by FM. Adapted from [9]	14
Figure 2.4: Decomposition of velocities and forces acting on a generic blade element. Image taken from [24].....	15
Figure 2.5: Distribution of induced velocity with or without the consideration of the tip loss factor	18
Figure 2.6: Angle convention for hovering and forward flight. From [24].....	20
Figure 2.7: Reverse flow in forward flight. From [24]	21
Figure 3.1: Calculation/Modeling/Results of curvature with two circumferences. The green line represents the total blade curvature, sum of the two circumferences (black and red lines respectively)	23
Figure 3.2: Inclination of a generic blade element with respect to the radial direction	24
Figure 3.3: Determination of the velocity component perpendicular to the LE for a curved blade	25
Figure 3.4: Aerodynamic efficiency vs angle of attack at different Reynolds numbers for NACA 0012 airfoil. Data obtained with the program XFOIL	26
Figure 3.5: Distribution of induced velocity and thrust coefficient for three different types of blade, having different rate of twisting amounts	28
Figure 3.6: Comparison between BEMT results obtained by Leishman and the Matlab code developed. Edited from [24].....	29
Figure 3.7: Comparison between experimental data and theoretical data for the Wessex helicopter in hover condition.....	29
Figure 3.8: Comparison between experimental data and simulation data for UH60A main rotor	30
Figure 3.9: Different lift polar for various Re values. The profile is NACA 0012	32
Figure 3.10: Lift and Drag polars interpolation with different polynomials	33
Figure 3.11: Lift polar for NACA 0012 at Re=30,000. From [18]	33
Figure 3.12: To the left, pressure coefficient distribution for the NACA 0012 airfoil at Re=30,000 (adapted from [17]). To the right, recirculation region near the TE of the airfoil (from [18]).....	34
Figure 3.13: Pressure coefficient distribution for NACA 0012 at Re=100,000. From [17]	34
Figure 3.14: Development of vortices at the upper airfoil surface, Re=23,000. From [15]	35
Figure 3.15: (a)-angles of attack for the straight untwisted blade with a root pitch angle of 16° and for the straight twisted blade for a root pitch angle of 24.5°; (b)-Aerodynamic efficiency at different Re numbers	36
Figure 3.16: FM vs thrust coefficient/solidity calculated with the BEMT	36
Figure 3.17: Re development along the blade in the case of five or ten divisions.....	37
Figure 3.18: FM behavior evaluated with three different approaches for the low RE regime	37
Figure 4.1: Pictures of a waterfall with different exposure times. From [52].....	40
Figure 4.2: Velocity profile inside a turbulent boundary layer. From [51]	41
Figure 4.3: Different approaches for boundary layer description. From [51].....	42
Figure 4.4: Moving Reference Frame method. From [31]	43
Figure 4.5: Total curved TE1 rotor, with location of the maximum point	47

Figure 4.6: Examples of fixed and moving domains.....	48
Figure 4.7: traslation of the body at the origin of the new frame of reference	49
Figure 4.8: skewness scale and element quality.....	50
Figure 4.9: Mesh metrics of the AR parameter, for the total curved blade TE1.....	51
Figure 4.10: Sphere of influence method, for the meshing of fixed domain. The moving domain is depicted in grey	52
Figure 4.11: Inflation near the rotor. Notice how the element dimensions changed with the surfaces curvature.....	52
Figure 4.12: Types of solver available in Ansys. From [50] Fluent. From [34]	54
Figure 4.13: rate of convergence achievements when using pseudo-transient approach. Image from [36]	54
Figure 4.14: discretization schemes. Image from [50]	56
Figure 4.15: utility of using the hybrid initialization against the standard initialization [36].	56
Figure 4.16: Examples of moving domains tested. The domain 1 is represented in the left, while the domain 5 is in the right.	58
Figure 4.17: FM and thrust coefficient for the five domains tested	60
Figure 4.18: Power coefficient for the five domains tested (left). On the right, table showing the percentage discrepancies between the domain 4 and the others.....	60
Figure 4.19: Velocity contour for domain 1, plotted on the YZ plane.....	61
Figure 4.20: Induced velocity distribution 15 mm below the rotor, parametrized for different domain dimensions	61
Figure 4.21: Thrust (a) and FM (b) trend varying the number of elements.....	62
Figure 5.1: Thrust (a) and Power (b) for the straight blade at different rotational velocities	63
Figure 5.2: Thrust coefficient, Power coefficient and FM for the straight blade at various rotational velocities	Errore. Il segnalibro non è definito.
Figure 5.3:FM behavior for untwisted blades, in case of backward curvature.....	65
Figure 5.4: FM behavior for twisted blades, in the case of backward curvature.....	66
Figure 5.5: Effect of inserting the twisting variation for the straight blade rotor and the backward curved rotors.....	66
Figure 5.6:Comparison between the contour of the region at constant swirling strength for the straight blade (a) and the single forward-curved blade at 19° (b) and 25° (c) of root pitch angle	67
Figure 5.7: Comparison between the single curved blade performance with backward and forward curvature direction	67
Figure 5.8: Region at constant swirling strength equal to 0.01 in the case of single curved blade SCF (a), TE1F (b) and TE2F (c) for a 19° root pitch angle.....	68
Figure 5.9: Comparison between the forward and backward curvature for the total curved blade TE2...68	68
Figure 5.10: FM behavior for untwisted blades, in case of forward curvature.....	69
Figure 5.11: Comparison of induced velocities between the 19° untwisted blade and the 26.5° twisted blade, having a twist variation of 10°.....	69
Figure 5.12: Effect of inserting the twisting variation for the straight blade rotor and the forward curved rotors.....	70
Figure 5.13: FM behavior for twisted blades, in the case of forward curvature.....	70
Figure 5.14: Comparison between BEMT and CFD data for the rotor studied	71
Figure 5.15: FM vs rotational speed; comparison between CFD and experimental data.....	72
Figure 5.16: Thrust and power coefficients versus climbing ratio	73
Figure 5.17: Climbing power ratio and climbing FM plotted versus the climbing ratio	74
Figure 5.18: Comparison between the tip modified rotors and the standard tip rotors	75

Figure 5.19: Comparison between SB3, TE3B and TE3F rotors.....	75
Figure A.1: FDM printing procedure, adapted from [38]	II
Figure A.2: Resume of ABS and PLA characteristics. From [41]	III
Figure A.3: Positioning the SB rotor for the FDM printing	VI
Figure A.4: Particular of the surface quality after the support removal for the case 1.....	VII
Figure A.5: Airfoil shape for case 2. It is noticeable the effect of vibrations in the airfoil shape.....	VII
Figure A.6: Single curved blade printed with method 2. On the right, particular of the tip profile.....	VIII
Figure A.7: Blade printed with Ideamaker (left), and particular of the blade tip (right). The presence of a small step near the TE all along the blade is noticeable.....	VIII
Figure A.8: Example of Prusa slicer display. In this case the blade is the total curved TE2 with presence of twisting. The program automatically builds a support for the tip of the blade.	IX
Figure A.9: Example of support material at the blade root.....	X
Figure A.10: Total curved blades TE1, TE2 printed with the SLA technology. The presence of the support material contributed to obtain the desired geometry.	XI
Figure A.11: FM behavior versus rotational speed. Comparison between experimental data and CFD simulations for the SB rotor with 15° root pitch angle.....	XIII
Figure A.12: Thrust and Power behavior versus rotational speed. Comparison between experimental data and CFD simulations for the SB rotor with 15° root pitch angle	XIII

List of tables

Table 1: UH-60A main rotor characteristics	30
Table 2: Computer characteristics	46
Table 3: Rotor prototypes and nomenclature	48
Table 4: Setup of the CFD simulations	57
Table 5: Meshing parameters for the moving domain analysis	59
Table 6: AR and Skewness statistic distribution	59
Table 7: AR e Skewness statistic distribution	59
Table 8: Statistic parameters for the mesh sensitivity analysis.....	62
Table 9: Discrepancies between results with different meshes.....	62
Table 10: Thrust comparison between the backward untwisted rotors. The percentages are calculated with respect to the straight blade	65
Table 11: Different infill tipologies	V
Table 12: Rotors printed with the SLA technology	XII
Table 13: Comparison between CFD and experimental results for SB rotor	XV
Table 14: Backward curvature – untwisted case - hovering conditions	XVI
Table 15: Backward curvature - twisted case - hovering conditions	XVI
Table 16: Forward curvature - untwisted case - hovering conditions	XVII
Table 17: Forward curvature - twisted case - hovering conditions	XVII

Acronyms

ABS	Acrylonitrile Butadiene Styrene
AD	Additive Manufacturing
AR	Aspect Ratio
BEMT	Blade Element & Momentum Theory
BET	Blade Element Theory
CAD	Computer Aided Design
CFD	Computational Fluid Dynamics
DL	Disk Loading
EVTOL	Electric Vertical Take Off and Landing aircraft
FDM	Fused Deposition Modeling
FM	Figure of Merit
FMG	Full MultiGrid initialization
IPA	Isopropyl Alcohol
LE	Leading Edge
MAV	Micro Air Vehicle
MRF	Moving Reference Frame method
MUSCL	Monotone Upstream Centered Schemes for Conservation Laws
PA	Polyamide
PC	Polycarbonate
PIV	Particle Image Velocimetry
PL	Power Loading
PLA	Polylactic Acid
PRESTO	Pressure Staggering Option

PVA	Polyvinyl alcohol
QUICK	Quadratic Upwind Interpolation
RANS	Reynolds Averaged Navier Stokes equations
RNG	Re-Normalization group
RP	Rapid Prototyping
SIMPLE	Semi-Implicit Method for Pressure-Linked Equations
SLA	Stereolithography Apparatus
SST	Shear Stress Transport
TE	Trailing Edge
UV	Ultra-Violet

Symbols

Roman symbols

A	Rotor disk area
A_{eff}	Effective rotor area
$A_{vena\ contracta}$	Vena contracta area
B	Tip loss factor
c	Airfoil chord
c_D	Airfoil drag coefficient
c_L	Airfoil lift coefficient
$c_{L\alpha}$	Lift slope
C_P	Power coefficient
$C_{P,i}$	Induced power coefficient
$C_{P,0}$	Profile power coefficient
C_Q	Torque coefficient
C_T	Thrust coefficient
$C_{T,obj}$	Desired thrust coefficient in the Blade Element Theory
dC_P	Infinitesimal power coefficient
$dC_{P,i}$	Infinitesimal induced power coefficient
$dC_{P,PROFILE}$	Profile power in forward flight
$dC_{P,REVERSE}$	Infinitesimal contribute for the reverse power in forward flight
dC_Q	Infinitesimal torque coefficient
dC_T	Infinitesimal thrust coefficient
dD	Infinitesimal drag contribute
dQ	Infinitesimal torque contribute

dR	Infinitesimal aerodynamic resultant
dr	Blade element length
$d\bar{S}$	Infinitesimal surface element
dT	Infinitesimal thrust contribute
dy	Infinitesimal radial length
E_{ij}	Mean tensor of velocity deformation
F	Prandtl tip loss factor
f	Prandtl tip loss coefficient
f'	Equivalent wetted area
F_x	In the experimental tests, equal to the thrust
F_y	In the experimental test, force orthogonal to the thrust
i	Index which controls the number of iteration in the Blade Element Theory
j	Index which controls the blade element selected for a calculation in the Blade Element Theory
k	Turbulent kinetic energy
k'	Rotor induced power factor
k_x	Parameter for obtaining the inflow equation in forward flight
M	Mach number
\dot{m}	Mass flow rate
M_x	In the experiment, torque required to put the rotor in rotation
N	Total number of blade elements
n_B	Number of blades
P	Power

\bar{P}	Averaged pressure
P_{climb}	Climbing power
Q	Torque
r	dimensionless radius
r_0	Root cut out parameter
R	Blade radius
R_{eff}	Effective radial length
r_m	Radius linking the center of the blade element with the center of rotation
\vec{r}_p	Position vector of the calculation point in the Moving Reference Frame method
r_s	Dimensionless blade radius
$R_{venacontracta}$	Radius of the vena contracta region
R_1, R_2, R_3	Bridge reading for the experimental tests
\vec{T}	Thrust
U	Air velocity at the generic blade element
u'_i	Velocity fluctuations
\bar{u}_i	Averaged velocity
u^+	Ratio between the real velocity and the viscous velocity
U_P	Velocity component perpendicular to the rotor disk
u_T	Viscous velocity
U_T	Velocity component parallel to the rotor disk
$V_{optimal\ cell}$	Optimal cell volume in Skewness definition
V_{cell}	Cell volume in Skewness definition

\vec{v}	Velocity vector
\vec{v}_{abs}	Absolute velocity in Moving Reference Frame method
\vec{v}_{rel}	Relative velocity in Moving Reference Frame method
\vec{v}_{trasl}	Traslational velocity in Moving Reference Frame method
v_i	Induced velocity
v_{inc}	Velocity perpendicular to the leading edge in BEMT for curved blades
v_c	Climbing velocity
v_h	Induced velocity in hovering condition
v_{tip}	Blade tip velocity
w	Velocity below the vena contracta region
W	Work done by the rotor on the airflow
y	Radial coordinate along the blade
y^+	Parameter used to define the position of a point inside a boundary layer

Greek symbols

α	Aerodynamic angle of attack
α_0	Zero-lift angle of attack
β	Angle between the vector linking the center of rotation with the center of the blade element and the radial direction
β'	Flapping angle
β''	Coefficient for the spatial discretization in the CFD
Γ	Diffusion coefficient
δ	Angle between the direction of a generic blade element and the vector linking the center of rotation with the center of the blade element
δ_{ij}	Kronecker delta

ϵ	Dissipation rate
ζ	Inclination of the generic blade element with respect to the radial direction
ζ'	Generic flow property in the CFD computational domain
θ_0	Root pitch angle
θ	Pitch angle
θ_{max}	Angle needed for the Skewness definition
θ_e	Angle needed for the Skewness definition
θ_{rate}	Rate of twist
λ_0	Induced velocity obtained with the momentum theory
λ_c	Dimensionless climbing velocity
λ_{inc}	Dimensionless velocity perpendicular to the leading edge
λ_i	Dimensionless induced velocity
μ	Air viscosity
μ_f	Forward ratio
μ_x	Forward ratio parallel to the rotor plane
μ_z	Forward ratio perpendicular to the rotor plane
ν	Kinematic viscosity
ν_T	Turbulent viscosity
ξ	Construction angle to obtain the velocity perpendicular to the curved blade
ρ	Air density
σ	Blade solidity
τ_{ij}	Reynolds stress tensor

τ_w	Viscous shear stress
ϕ	Induced angle
χ	Wake skew angle
ψ	Blade azimuth angle
Ω	Angular velocity
ω	Specific dissipation rate

1 Introduction

The drone sector is expanding almost exponentially, and for many reasons these light air vehicles will be present more and more in everyday life. Controls of agricultural fields, surveillance, transportation of objects and video registration are only some examples of the high number of civil applications to which drones can be used. One of the greatest concerns about their use is the autonomy that strongly depends on the quality of batteries as well as on the power consumption of the devices installed. From an aerodynamic point of view, it is very important to reduce the power to a minimum that is required for flight. This can be done by reducing the parasitic drag of the drone itself and by improving the performance of the rotor(s) used as propellers. The latter point is treated in this work. Different studies were made in the last years to understand how changing the rotors geometric parameters may affect their performances. To the knowledge of the author no studies were made inserting a curvature of the blades, thus this became the main purpose of the thesis.

1.1 Overview

1.1.1 Drones development sectors

While the use of drones in the military field is well established, thanks to the possibility of carrying first aid supplies, scanning remote regions with high-tech cameras, and cooperate with trucks for surveillance aim, in the last few years interest spread in using them also for civil purposes. In particular, the importance of drone in cargo transportation seems to be the next step that this technology will achieve in the short time period. The e-commerce has become one of the faster improving business fields, and this is demonstrated by the rise of companies such as Amazon, or Uber. The delivery speed is crucial in this sector, and drone transportation seems to shorten this parameter. Amazon launched the project Prime Air through which it will guarantee the delivery of a good to the customer in less than 30 minutes, with the first test flight done in 2016. At the current date, the project has not started yet. However, other companies are already using drones. In 2017, the delivery company AHA started a partnership with Flytrex to expand the delivery network and shorten delivery time of products in the Iceland capital Reykjavik [1]. The city is divided by a river so that transporting a good from one side to the other could take about twenty minutes. With the use of drones, the time was reduced up to just four minutes. Other examples of drones transportation utility can be found in Switzerland, where the EOC hospital group and Matternet, a Silicon Valley-tech company, built a joint project to transport laboratory samples and extra bloods bags between laboratories and hospitals with drones having a 20 km range and a 2 kg maximum carriage [1]. This project was the first used in a strongly urbanized region, while in rural areas the usage of drones for transportation of medical goods were already in use, especially in the East Africa, namely Tanzania and Rwanda.

The interest in this new transport typology is also pushed by the potential low cost, and the low environmental effect. D'Andrea [2] showed the low operative cost of delivery with drones, taking into account the aerodynamic efficiency, the payload mass, the cruising velocity and the power consumption of electronics. Goodchild and Toy [3] compared the CO₂ emissions of a truck-based and a drone-based delivery system for the city of Los Angeles. Their conclusions were that drones tend to emit a lower amount of CO₂ when the service zones are close to the depot, while trucks behaved better in the case of longer trips because of their greater capability in delivering different goods at the same time.

Another sector that is foreseen to live a great development in the next years is the one of Electric Vertical Take Off and Landing aircraft (EVTOL). The technology advancements in term of batteries, motors, and automatic navigation, as well as the possibility of reducing the aircraft weight by using composite materials are the background for this new type of mobility. In fact, EVTOL are vehicles with dimensions that fit between the drones and the normal scale airplanes, and their propulsion is guaranteed by small-size rotors which are electrically driven. They should be used for the transportation up to a maximum of five people at the same time. Conceptually, they are similar to helicopters, but not needing the presence of a tail rotor to counterbalance the tendency of the cabin to rotate in the opposite direction of the main rotor make them interesting for the use in densely populated areas, while the motor electrification brings a decrease in the maintenance cost with respect to normal scale helicopters.

Both startups and major companies are investing in this sector. Among the startups, the german Volocopter produced the Volocopter 2X model that has a gross weight of 290 kg, and is capable of transporting two people by means of 18 small rotors driven by lithium-ion batteries [4]. Airbus flight-tested the one-seater model Vahana, and the four-seater model City Airbus to verify the feasibility of this new technology [5]. Moreover, it started a partnership with Audi and Italdesign, the Pop-up next project, with the aim of making the EVTOL passenger cabin adapted to fit on a wheel-based section, thus transforming it to a classical road car [6].

1.1.2 Analyses of small-scale propellers

One of the first studies realized with small-scale rotors was done by McVeigh & McHugh [7]: they conducted an experimental test campaign with subscale rotors, focusing on the effects of tip shape on the Figure of Merit (FM) and aerodynamic efficiency. They focused on four different types of rotor, with rectangular tip, swept tip, swept-tapered tip, tapered tip. The blade with tapered tip resulted in a 10% better lift-to-drag ratio with respect to the rectangular blade. However, the rectangular blade seemed to have better performances with respect to the blades with a swept tip.

In more recent years, Brandt [8] experimentally studied 79 micro propellers, having a diameter between 9 and 11 inches, and inside a Reynolds (Re) interval between $5 \cdot 10^4$ and $1 \cdot 10^5$. The tests were realized for different advance ratios. A great efficiency variability was found, thus underlining the importance of selecting the proper rotor shape for each application.

Benedict & others [9] studied how the variation of different rotor parameters modify the performances. They focused on the effect of changing the airfoil shape, the twisting rate, the presence of tapering, the number of blades, the presence of tip winglets, arriving to the definition of an optimum hovering rotor. This rotor is characterized by a very thin cambered profile, a long chord, and the presence of tapering. An important finding was the role of winglets in reducing the tip vortices.

Ramasamy [10], [11] measured thrust and power for several rotor blades at Re equal to $3.5 \cdot 10^4$, changing the blades planform, twisting rate and airfoil shape. Moreover, the Particle Image Velocimetry (PIV) technique was used to understand how these geometric parameters influenced the wake region. He stated that the reduction of wake losses may be fundamental in increasing small-scale rotors efficiencies and suggested that a sharp leading edge (LE) and trailing edge (TE) may help in this sense. Thanks to PIV he detected the following important features:

- Formation of eddies at the merging point between upper and lower boundary layers
- The vortex sheets are much thicker and more turbulent than rotors at higher Re
- The helicoidal vortex sheets fold down on each other, thus occupying a substantial part of the vena contracta, the wake region immediately below the rotor.

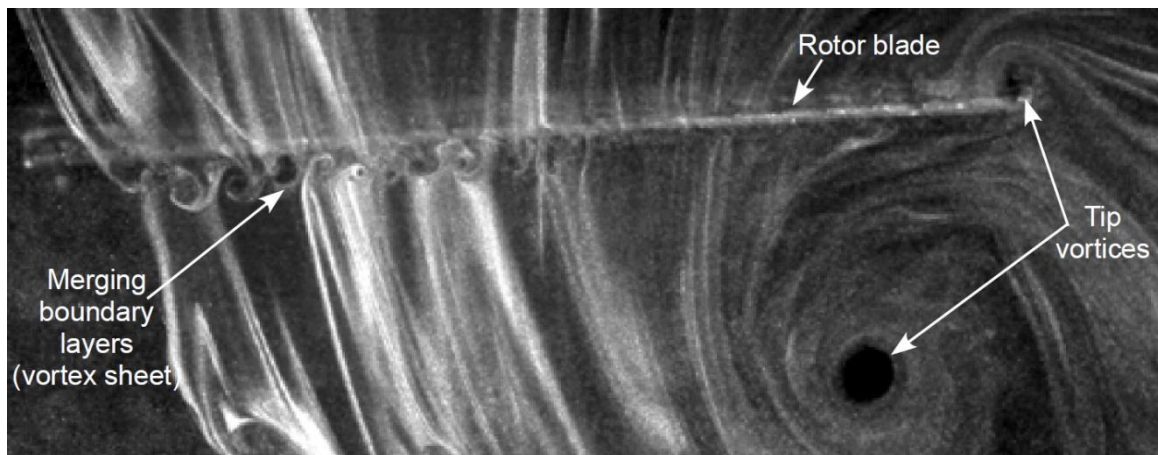


Figure 1.1: Tip vortices and boundary layers merging, taken with PIV technique. Picture taken from [10]

1.1.3 Analyses of Low Reynolds aerodynamics

One of the most important differences between helicopter scale rotors and small-scale rotors is the Re operative interval. The Re is used as discriminant to classify a flow as laminar or turbulent. A flow around an obstacle is considered turbulent if $Re > 2 \cdot 10^4$, but the passage between the two regimes depends on different factors, and it can happen also at different Re values. What happens in the low Re regime has interested researchers throughout the last century, and there are still some phenomena to be completely understood. The first studies of low Re regime were made by Schmitz [12]. He measured forces generated by a thin flat plate, a thin cambered plate, and a thick cambered airfoil, slowly increasing the Re number in the range $2 \cdot 10^4 < Re < 2 \cdot 10^5$. He found out that there was a critical value of the Re after which the lift produced dramatically increased, while the drag decreased, thus causing a

big improvement in the aerodynamic performance. McMaster & Henderson [13] extended the work by studying several airfoils, plotting their $\frac{c_L}{c_D}$ at different Re.

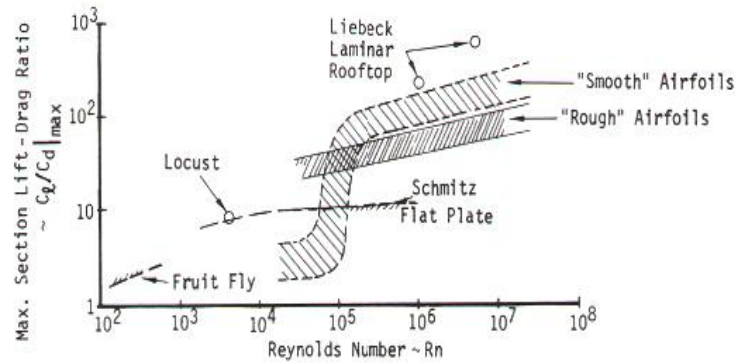


Figure 1.2: Change of aerodynamic performances at various Re number. Image from McMaster [13]

Their work showed that smooth airfoils, which have higher aerodynamic performances at high Re regimes, poorly behave when the Re is lower ($\approx 4 \cdot 10^4$): in this last regime, it seemed better for airfoil surfaces to be rough, because they didn't show the sudden decrease for the ratio lift to drag (L/D).

Laitone [14] operated measurements of forces with a force balance characterized by an accuracy of 0.1 mN for a cambered plate, the NACA 0012 airfoil, and a thin wedge airfoil. He obtained a variety of interesting results: in fact, the 5% cambered plate seemed to be the best configuration at low Re number. Moreover, he tested the NACA 0012 normally oriented, and reversing its orientation (that is, the usual trailing edge was used as leading edge for the experiment). The reversed profile behaved better than the NACA 0012 normally oriented, producing more lift at the same angle of attack: this led the author to the conclusion that having a sharp leading edge could bring some positive results in this regime. The

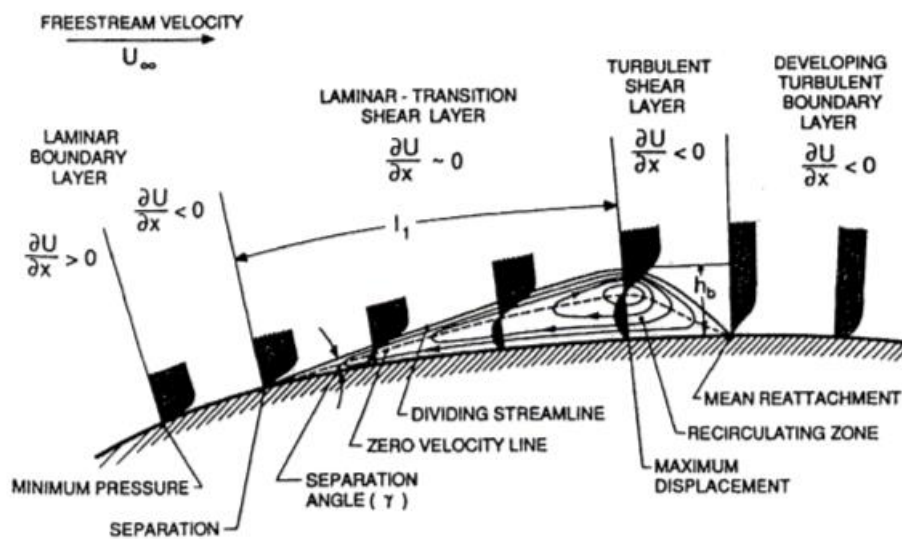


Figure 1.3: Formation of the laminar separation bubble. Picture from [53]

physical phenomena of “laminar separation bubble” formation, transition to turbulent regime, and flow reattachment to the airfoil were considered as the cause of the results above mentioned. This bubble is generated when a laminar boundary layer encounters an adverse pressure gradient which causes its separation. After the separation, the flow becomes turbulent and it recirculates. This turbulence transports the momentum from the free-stream region towards the airfoil surface, till a point where it reattaches. It must be noticed that, for particularly low Re , the reattachment of the separated shear layer may not happen. However, as the Re increases, the reattachment point moves towards the leading edge of the airfoil, thus reducing the region interested by recirculation. The characteristics of the separation bubble strongly depend also on the angle of attack, the type of profile, and the surface quality, as noted by Dong-Ha Kim & others [15] in their experimental work: they studied a NACA 0012 airfoil of 180 mm chord at 0° , 3° , 6° of angle of attack, and at three different Re : $2.3 \cdot 10^4$, $3.3 \cdot 10^4$, $4.8 \cdot 10^4$.

An interesting and counter-intuitive characteristic for the NACA 0012 profile has been found experimentally by Ohtake & others [16]. When the Re is inside the interval $1 \cdot 10^4 < Re < 1 \cdot 10^5$ the lift coefficient presents a strongly nonlinear behavior with the angle of attack, and a negative lift production between the angles from 0° to around 2° . The authors studied experimentally this Re interval, with an increment of 10,000 Re , and changing the angle of attack from -20° to 20° in steps of 0.2° . Five different angle of attacks intervals were isolated, each one presenting flow features addressed as responsible for the airfoil aerodynamic properties.

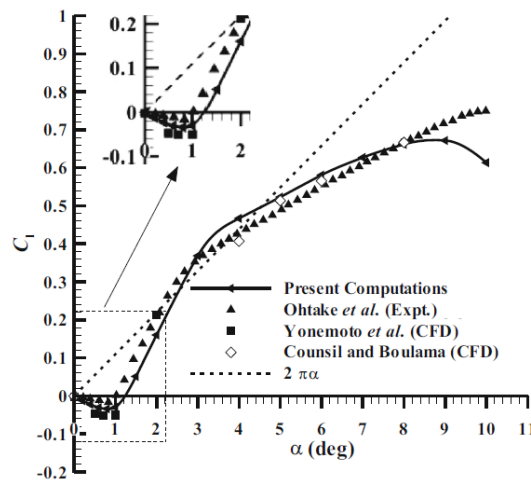


Figure 1.4: Non linear behavior of the lift coefficient for NACA 0012 airfoil at $Re = 50,000$. From [18].

Yonemoto, Takato and Ochi [17] obtained similar results by numerically solving the Navier-Stokes equations at these Re regimes, confirming the presence of a negative lift region, as well as the violation of Kutta condition at the trailing edge of the airfoil: in fact, the flow at the lower airfoil surface turns around the trailing edge, moving towards the upper surface, thus developing a recirculation region. The computational work of Pranesh & others [18] linked the negative lift production for the NACA 0012 to the flowfield, stating a relation with an equivalent negative-cambered profile. In chapter 3 a more detailed analysis of this phenomenon will be given.

1.1.4 CFD analysis of rotating systems

The experimental analysis of small-scale propellers is the most precise technique to evaluate the performance of a rotor geometry but is not always affordable. This, in union with the great development that computational fluid dynamics (CFD) achieved in the last years, made the computational simulations one of the most used tools for predicting aerodynamic characteristics of a system. Two of the main methods for the CFD study of rotating objects are the Moving Reference Frame method (MRF) and the sliding mesh method. In the past years, many studies were made using these methods, to verify whether the results were reliable.

Kutty & Rajendran [19] studied the performances of an APC propeller at different advance speeds, keeping the rotational velocity fixed. The comparison of simulations results with experimental data showed a good agreement thus approving the MRF which they used for the analysis of small-scale rotating propellers.

Atmaca, Cetin & Yilmaz [20], modeled the flow characteristics of small-scale aircrafts moving together. They chose to model the phenomenon by means of both an MRF and sliding mesh approach, concluding that the simulations settings were reliable for the study of drone behavior.

Subhas and others [21] studied the flow around a marine propeller with the MRF method. The results of thrust and power coefficients were in good agreement with experimental results, thus allowing the author to suggest the usage of CFD for the prediction of flow characteristics.

Stajuda, Karczewski et others [22] focused on the effect of changing some MRF parameters to check how they affected the results. They concluded that the domain dimensions should be calibrated with experimental data once fixed the rotational speeds, since they could change the results in term of thrust and power.

Franzke, Sebben and others [23] studied an axial cooling fan by making use of the MRF approach, with focus on how the moving domain dimensions influence the distribution of properties such as temperature, pressure and velocities along the flow field. They concluded defining the importance of imposing a correct moving domain dimension also for well capturing the diffusion of these scalar quantities in the flow field.

1.2 Objectives

From the literature research done, it seems that the effect of inserting a curvature for the blade planform has not been investigated, because scientists focused more on tip shape, tapering and pitch angle variation. This work aims to study if the insertion of a curved leading edge could bring benefits in small rotor performances with focus on the hovering flight condition, and ascending flight conditions. In order to do so, a Matlab code implementing the Blade Element Theory (BET) and the Blade Element and

Momentum Theory (BEMT) is developed. Moreover, an extension of the program is prepared, to take into account the effect of having a curved blade shape, and it must be verified if it is possible to use this program also at small scale. The development of a correct procedure for the CFD analysis of the problem is then required. A rounded tip shape is introduced to check if it is possible to decouple the curvature and tip influences on rotor performances. Another thesis objective is to test different 3D printing procedures, to understand which could be used for the printing of models to be experimentally tested. Finally, the printed rotors are tested experimentally to verify the accuracies of the CFD results.

1.3 Thesis outline

In the present Chapter 1, a bibliographic research regarding the current knowledge about small rotors performances is presented, with emphasis on the experimental studies done to understand how geometric modifications affects rotor behavior, and on the aerodynamics at low Re number. Moreover, studies which used CFD simulations to capture the rotors behavior are presented. This chapter contains also the thesis objectives, as well as the thesis organization. Chapter 2 deals with the theoretical background of the thesis, introducing the Momentum theory, the BET and the BEMT. In Chapter 3 the implementation of these theories in a Matlab code are presented, together with the analytical definition of a procedure to take curvature into account. Moreover, the details of the Matlab analysis are presented.

Chapter 4 contains the development of CFD simulations, starting from some theoretical aspects of this technique, which justify the assumptions later made. The description of the geometrical model, the meshing procedure and the simulations setup are part of this chapter, as well as the analysis of mesh sensitivity and moving domain sensitivity.

Chapter 5 is dedicated to the simulations results, which are critically discussed, while Chapter 6 is dedicated to the conclusions and to the suggestions for future works in this field. In the Appendix, the different 3D printing techniques tested are presented, together with the results from the experimental analysis.

2 Theoretical background

This chapter deals with the description of the main analytical theories which can be used for the description of rotating blades.

2.1 Momentum theory

Throughout the years, many theories have been developed for the description of the performances of rotating blades. One of them is the so-called Momentum theory which through a mono-dimensional treatment of the physics can provide an interesting insight to understand the overall performances of rotating blades at various flight conditions. Moreover, with certain assumptions, this theory takes many tridimensional effects into account, such as tip and root losses for the thrust coefficient. This theory is based on the application of fluid conservation laws on a control volume that is precisely defined. Following the approach of Leishman [24], in the case of hovering flight the hypothesis at the basis of this theory are:

- 1D development of fluid characteristics (the fluid properties can vary only along the vertical line)
- constant fluid properties in planes parallels to rotor disk
- incompressible fluid
- quasi-stationary regime

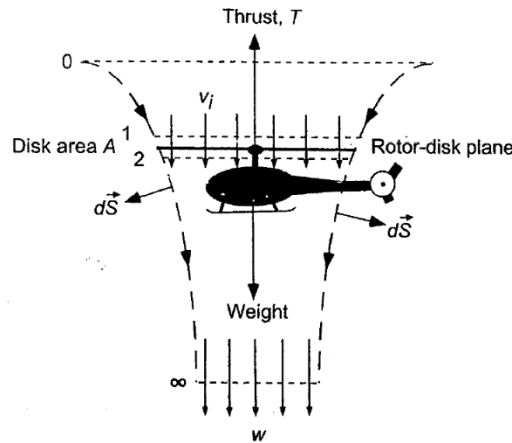


Figure 2.1: Control volume for the momentum theory. From [24]

The control volume contains the rotor, the wake region, and has a normal $d\vec{S}$ that according to the conventions always points outwards. The conservation laws for this control volume in the case of a time-invariant analysis can be written as follows, considering the vertical direction:

$$\int \rho \vec{v} d\vec{S} = 0 \quad (2.1)$$

$$\int \int p d\vec{S} + \int \int \rho \vec{v} \cdot \vec{v} d\vec{S} = \vec{T} \quad (2.2)$$

$$\frac{1}{2} \int \int \rho \vec{v} |\vec{v}^2| \cdot d\vec{S} = W \quad (2.3)$$

Where ρ is the air density, \vec{v} is the air velocity, $d\vec{S}$ is the infinitesimal domain surface, p is the pressure, \vec{T} is the thrust produced and W is the work needed to obtain the thrust.

Equation 2.1 states that the mass flow entering in the control volume from the upper surface is always equal to the mass flow exiting the volume (from the lower surface). From [24] it can be written $abs(\vec{T}) = T = \dot{m}w$, in which \dot{m} represents the mass flow rate, and w is the velocity of the fluid elaborated by the rotor at a sufficient far distance from the rotor itself (below the region called vena contracta). Equation 2.3 shows that $w = 2v_i$, i.e. the velocity in the wake region (w) equals two times the rotor-induced velocity (v_i). This last variable is very important since it influences almost every presentational parameter of a rotor. In the case of hovering condition, it can be shown that the induced velocity assumes the following value:

$$v_i = \sqrt{\frac{T}{2\rho A}} = \sqrt{\frac{DL}{2\rho}} \quad (2.4)$$

in which A is the rotor disk area and $DL = \frac{T}{A}$ is the disk loading and represents another important helicopter's parameter.

The relation found between the velocity at the rotor section and in the vena contracta implies another significant relation between the areas of these two regions. Through the continuity equation it can be shown that $A_{vena\ contracta} = A/2$. From this relation, the relation between the radiuses is readily obtained: $R_{vena\ contracta} = R\sqrt{2}$, in which R is the rotor radius.

Thus, the streamlines follow converging paths after the rotor disk till a point in which the velocity is equal to w and the section is half of the disk area. Since power can be expressed as $P = T v_i$, a relation for the power required for the flight in hovering condition can be obtained, according to the Momentum theory and without considering the profile drag losses:

$$P = \frac{T^{\frac{3}{2}}}{(2\rho A)^{\frac{1}{2}}} = 2\rho A v_i^3 \quad (2.5)$$

This relation demonstrates that the power P is proportional to the induced velocity elevated to the power of 3. Therefore, a low range of the induced velocity is crucial in order to maintain power under certain values: considering the thrust as a fixed requirement and analyzing equation (2.4), it is obvious that the rotor area should increase. In summary, the performances of small-scale rotors may not be optimal, due to the requirement of having a reduced dimension for the rotor.

Another very important parameter is the Power Loading PL that gives reason to the rule just stated:

$$PL = \frac{T}{P} = \frac{1}{v_i} = \sqrt{\frac{2\rho}{DL}} \quad (2.6)$$

The expression for PL shows an important characteristic for helicopters that represents the reason why the helicopter's design process must be a compromise: the Power Loading and the Disk Loading are inversely proportional, so that a maximization of the specific ability to produce thrust cannot be achieved without compromising the consumption of power needed to produce that thrust.

2.1.1 Dimensional analysis, thrust and power coefficients

Starting from the Buckingham dimensional analysis both the thrust coefficient and the dimensionless induced velocity can be obtained:

$$C_T = \frac{T}{\rho A v_{tip}^2} \quad (2.7)$$

$$\lambda_i = \frac{v_i}{v_{tip}} = \sqrt{\frac{C_T}{2}} \quad (2.8)$$

Helicopter performances can be described by these two parameters. Further, they are used to calculate the ideal power coefficient. The ideal power coefficient represents the power required to stay in hovering condition without considering any kind of friction and assuming a uniform flow in input:

Numerically, both power and torque coefficient have the same value (being Q the torque):

$$C_{P,i} = \frac{C_T^{\frac{3}{2}}}{\sqrt{2}} = C_T \lambda_i \quad (2.9)$$

$$C_Q = \frac{Q}{\rho A \Omega^2 R^3} \quad (2.10)$$

2.1.2 Power requirements

The results of the Momentum theory regarding the power required to hover don't match experimental data, due to non-considering skin friction and other loss factors [24]. To take them into account, first an empirical parameter k' is introduced. By considering a constant value of the drag coefficient along the blade c_{D0} , the power requested to supply the profile drag can be determined:

$$P_o = \Omega n_b \int D y dy = \Omega n_b \int \frac{1}{2} \rho v^2 c_D c y dy = \frac{1}{8} \rho n_b \Omega^3 c_{D0} c R^4 \quad (2.11)$$

in which Ω is the rotational velocity, n_b indicates the number of blades, y is the radial coordinate along the blade.

Applying the adimensionalization, the profile power coefficient is readily obtained:

$$C_{P0} = \frac{1}{8} \frac{n_b c r}{A} c_{D0} = \frac{1}{8} \sigma c_{D0} \quad (2.12)$$

where σ represents the rotor solidity and equals the blade area divided by the rotor disk area. Conclusively, the total power coefficient required for a rotor in hovering, according to the Momentum theory is

$$C_P = C_{P0} + C_{Pi} = \frac{\sigma c_{D0}}{8} + \frac{k' C_T^{\frac{3}{2}}}{\sqrt{2}} \quad (2.13)$$

2.1.3 Figure of Merit

The Figure of Merit (FM) is a parameter that describes the rotor efficiency in hovering flight conditions [24] It is the ratio between the ideal power required to hover (the induced power) and the actual power required to hover, that comprises the effects of the aerodynamic forces on the blades surfaces.

$$FM = \frac{C_{P,ideal}}{C_{P,real}} = \frac{\frac{C_T^{\frac{3}{2}}}{\sqrt{2}}}{\frac{\sigma c_{D0}}{8} + \frac{k' C_T^{\frac{3}{2}}}{\sqrt{2}}} \quad (2.14)$$

It expresses how efficient a rotor is in terms of thrust generated using a given amount of power. FM can only be used as a way of comparison between two different rotors if they have the same disk loading DL. In fact, with DL growing, FM increases as the induced power grows faster than the profile power. Therefore, considering two rotors with different DL, the one with greater disk loading will also have a greater FM. This relation is clearly stated by the following equation:

$$FM = \frac{P_{ideal}}{k' P_{ideal} + P_0} = \frac{1}{k' + \frac{P_0}{P_{ideal}}} = \frac{1}{k' + \frac{\sqrt{2\rho} P_0}{T\sqrt{DL}}} \quad (2.15)$$

The FM defines the aerodynamic quality of the rotor design. Nowadays, the best helicopter rotors can reach a FM of approximately 0.82, while the maximum value in the case of subscale rotors is still relatively low, due to phenomena that will be discussed later in chapter 3.

2.1.4 Tip losses

The presence of vortices at the end of the blade implies a reduction in the lift with respect to the ideal case of infinite blade. By considering the blade shorter than the reality at factor B , that side effect is incorporated into the equations for obtaining thrust and power [24].

$$R_{eff} = B \cdot R, \quad B < 1 \quad (2.16)$$

Similarly, the introduction of the non-dimensional parameter r_0 underlines the fact that the sections near the root do not produce lift. Merging these two effects, the following expression for the effective area can be obtained:

$$A_{eff} = (B^2 - r_0^2)A \quad (2.17)$$

This effective value for the area has significant consequences such as the increasing of the disk loading value, the induced velocity and the induced power. It is obvious that B gets lower in two cases: for a rotor with less blades because there is less blade-to-blade interference, and if the thrust gets higher as the vortex lines are pushed far below the rotor. Many scientists developed different relations for the determination of B , among them Gessow and Myers who suggested a semi-empirical expression for this parameter [24]:

$$B = 1 - \frac{c}{2R} \quad (2.18)$$

2.1.5 Axial flight

The case of axial flight can be studied with the Momentum theory, ensuring that there is the clear definition of a control volume to which the conservation equations will be applied. This is straightforward in the case of ascending flight, while for the descending flight it limits the validity of the Momentum theory to descending velocities $v_c < -2v_h$, where v_c is the climbing velocity and v_h represents the induced velocity in hovering conditions, calculated in equation 2.4. For the application of conservation laws to the control volume around the rotor the same hypothesis made for the hovering case are kept valid. The momentum equation states again $T = \dot{m}w$, with the velocity $w = 2v_i$, as in the hovering case.

Following the approach described by Leishman [24], an equation showing how the axial induced velocity changes with the climbing velocity is readily obtained:

$$\text{Ascending flight} \quad \frac{v_i}{v_h} = -\frac{v_c}{2v_h} + \sqrt{\left(\frac{v_c}{2v_h}\right)^2 + 1} \quad (2.19)$$

$$\text{Descending flight} \quad \frac{v_i}{v_h} = -\frac{v_c}{2v_h} - \sqrt{\left(\frac{v_c}{2v_h}\right)^2 - 1} \quad (2.20)$$

Analyzing 2.20, it is noticeable how an increase of the ascensional velocity v_c leads to a decrease in the induced velocity, this modifying the induced power required to the rotor. In conclusion, the induced power requirement to obtain a certain thrust is lower in climbing than in hover [24]. However, in the case of axial flight, there is an additive power requirement to increase the helicopter potential energy:

$$P_{climb} = T(v_c + v_i) \quad (2.21)$$

It is possible to compare a rotor that is producing the same thrust amount in hovering condition and steady climbing condition. This leads to the following relations, for both ascending and descending case:

$$\frac{P_{climb}}{P_h} = \frac{v_c}{2v_h} + \sqrt{\left(\frac{v_c}{2v_h}\right)^2 + 1} \quad (2.22)$$

$$\frac{P_{climb}}{P_h} = \frac{v_c}{2v_h} - \sqrt{\left(\frac{v_c}{2v_h}\right)^2 - 1} \quad (2.23)$$

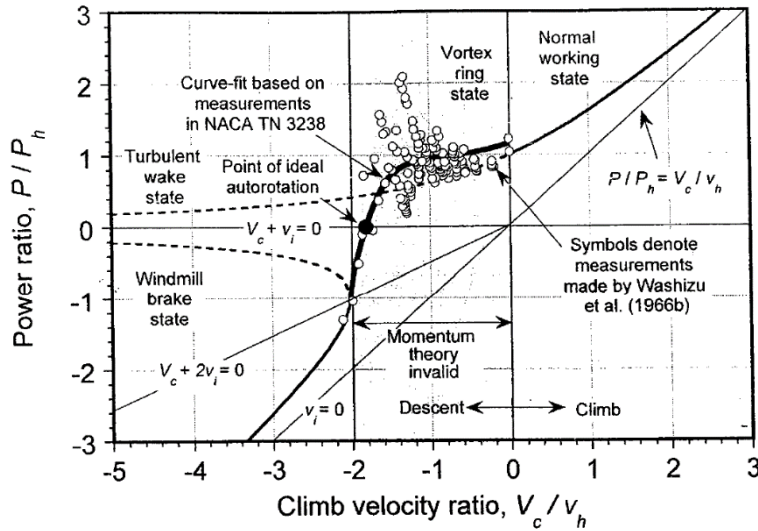


Figure 2.2: Power ratio vs climb velocity ratio, as predicted by the momentum theory. From [24]

For high descending velocities, the rotor operates as a windmill, extracting energy from the air, and thus requiring less power than in the hovering case. As the ascending velocity increases, there is an increase in the total power requirement, even if the induced power is decreasing due to the behavior of v_i described in 2.19. Further information about the operative conditions for a rotor in axial flight can be found in [24].

The FM introduced in section 2.1.3 is defined strictly for hovering condition, however a similar parameter to compare performances of different rotors in axial flight can be expressed as the ratio between the ideal power requirement versus the actual requirement. The ideal power requirement can be expressed from equation 2.22-2.23, while the real one has to be defined from computational or experimental tests.

$$FM_{climb} = \frac{P_{climb,ideal}}{P_{climb,real}} \quad (2.24)$$

Through the Momentum theory it is possible to determine also the rotor performances in case of forward flight, these arguments will not be covered in this chapter. For further information refer to [24].

Considering the results of the Momentum theory, it is possible to plot the FM as function of k' , a parameter used to describe the induced losses, and $\frac{c_L}{c_D}$, that represents the aerodynamic efficiency of the profile. From graph 2.3, in order to reach high values of FM, there is the need to reduce both the profile losses and induced losses. If the induced losses are high, there is no airfoil design able to recover the performance. In this graph, the area inside the blue circle is occupied by the modern full-scale helicopter rotors, while the area inside the green circle is occupied by the drones' rotors: the aim of drones designers is to move towards the left part of the graph, i.e. reduce the induced losses.

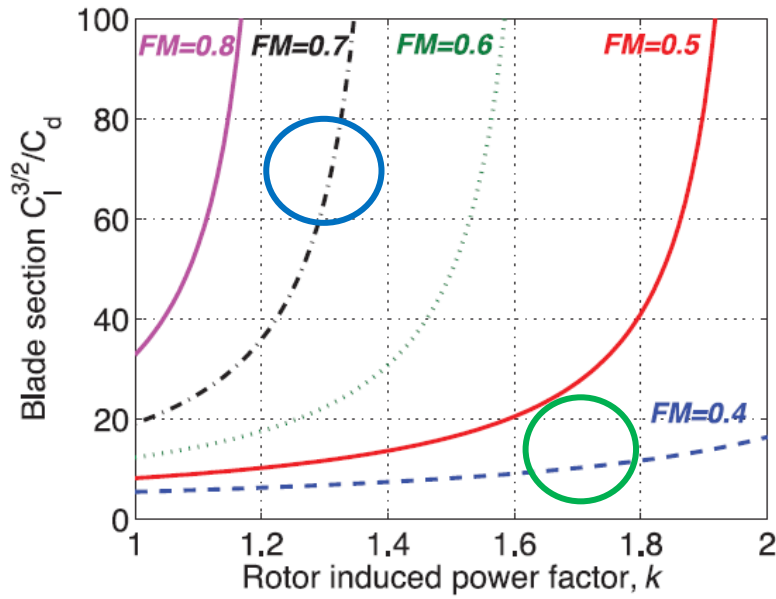


Figure 2.3, plot of the aerodynamic efficiency with respect to the induced-losses coefficient, parametrized by FM. Adapted from [9]

2.2 Blade Element Theory

The blade element theory (BET) is a common way to approach the preliminary design of a rotor because it has some undoubtable advantages [24]:

- It gives the possibility of a complete sight on the overall rotor performances,
- it has a very low computational cost compared to other aerodynamics procedures of analysis such as CFD,
- the results are quite accurate compared to experiments, and

- it is possible to consider effects such as tip, root and compressibility as well as other mechanisms of performance losses inserting the modeling defined by previous studies.

This theory permits the determination of aerodynamic loads at predefined stations and obtains the total value through integration along the blade. It is based on the principle that successive blade elements are independent, so that the aerodynamic characteristics of the flux over a station can be considered bidimensional. It is however possible to take into account the 3D effects with the tip loss theories and considering that the induced-velocity field varies along the radial coordinate of the blade (BEMT).

Another assumption made is that the aerodynamic forces are influenced only by the component of the velocity orthogonal to the blade LE. Keeping the presence of an induced angle as a result of the velocity that the rotor induces to the air flow in mind, the effective aerodynamic angle of attack differs from the blade pitch angle (see figure 2.4). A component of the lift force acts along the chord of the blade station considered and is responsible of the induced drag.

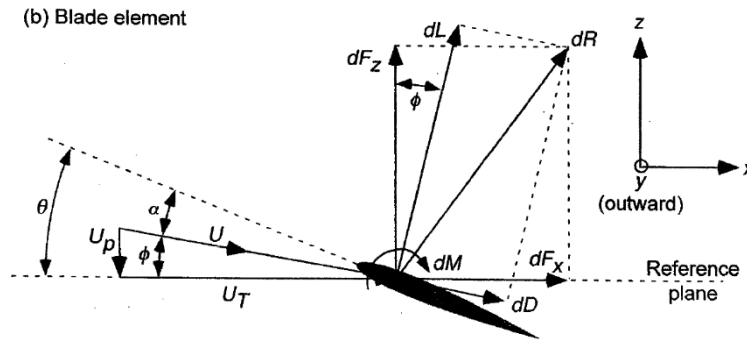


Figure 2.4: Decomposition of velocities and forces acting on a generic blade element. Image taken from [24]

Assuming a generic blade station, the aerodynamic resultant dR can be decomposed in dL and dD or dF_z and dF_x . In general, the integration of dF_z states the definition of the thrust, that in hovering condition must equal the weight of the aircraft. Looking at figure (2.4), the following equations can be established:

$$dF_x = dL \sin(\phi) + dD \cos(\phi) \quad (2.25)$$

$$dF_z = dL \cos(\phi) - dD \sin(\phi) \quad (2.26)$$

Where ϕ is the induced angle, responsible of the difference between the pitch angle θ and the aerodynamic angle of attack α .

In hovering condition, the field of induced velocity is axisymmetric, which results in:

$$dT = n_b dF_z \quad (2.27)$$

$$dQ = n_b y dF_x \quad (2.28)$$

Generally, the value of the angle ϕ can be assumed small, so that $\cos \phi \approx 1$, $\sin \phi \approx \phi$, and dD two orders of magnitude smaller than dL [24]. In this way, equation 2.27 represents a simplified but still accurate definition of the thrust contribute. The definition of the infinitesimal contributes of thrust and moment can be written as:

$$dT = n_b dL \quad (2.29)$$

$$dQ = n_b \gamma (dL\phi + dD) \quad (2.30)$$

As already mentioned in the current chapter, it is quite useful to utilize dimensionless coefficients instead of the actual values of thrust, moment or power. Therefore, the following steps define the infinitesimal value of thrust, moment and power coefficient as well as the induced ratio and the dimensionless blade radius:

$$dC_T = \frac{dT}{\rho A (\Omega R)^2} \quad , \quad dC_Q = \frac{dQ}{\rho A (\Omega R)^2 R} \quad , \quad dC_P = \frac{dP}{\rho A (\Omega R)^3} \quad , \quad \lambda = \frac{v_i + v_c}{\Omega R} = \phi r \quad , \quad r = \frac{y}{R}$$

In the expression above, v_c represents the climbing velocity in the case of axial flight. λ is the dimensionless induced velocity, while r represents the dimensionless radial coordinate.

By simply substituting the values of dT , dQ , dP in the expressions above, equations (2.31) and (2.32) can be expressed:

$$dC_T = \frac{1}{2} \sigma c_L r^2 dr \quad (2.31) \quad dC_Q = dC_P = \frac{1}{2} \sigma (\phi c_L + c_D) r^3 dr \quad (2.32)$$

In the definition of the power coefficient, the presence of an induced term (ϕc_L) and the presence of the profile term (c_D) can be underlined, like in the Momentum theory.

By integrating the contributes of every blade station, the global rotor coefficients then can be obtained. However, in order to calculate these integrals, it is necessary to know the following parameters:

- $\lambda = \text{function}(v_c, v_i)$
- $c_L, c_D = \text{function}(Re, M, \alpha)$
- $\alpha = \text{function}(\theta, v_c, v_i)$
- $v_i = \text{function}(r)$

Often, there is a numerical solution chosen for their determination. Another simplification in the determination of the lift coefficient can be made, writing $c_L \approx \frac{dc_L}{d\alpha} (\alpha - \alpha_0) = c_{L\alpha} (\theta - \alpha_0 - \phi)$. In the following analysis the presence of α_0 which is the angle for which a profile generates no lift, is included inside the value of the twist angle. Following the simplifications just made, the thrust coefficient is now ready to be calculated:

$$C_T = \frac{1}{2} \sigma \int c_{L\alpha} (\theta - \phi) r^2 dr \approx \frac{1}{2} \sigma \int c_{L\alpha} \left(\theta - \frac{\lambda}{r} \right) r^2 dr \quad (2.33)$$

By taking σ out of the integral, the assumption that the blade chord does not vary along the blade is clarified, i.e. the tapering is not considered. Further, considering the pitch angle constant along the blade ($\theta = \text{constant} = \theta_0$):

$$C_T = \frac{1}{2} c_{L\alpha} \left(\frac{\theta_0}{3} - \frac{\lambda}{2} \right) \quad (2.34)$$

It is possible to solve this equation in order to find the value of thrust achievable having a known value of pitch angle. Additionally, recalling that $\lambda = \sqrt{\frac{C_T}{2}}$ for the hovering case, the value of pitch angle required

in order to obtain a certain thrust coefficient value can be obtained. The last strategy is the more common one in the design procedure of rotors.

A linear twist variation along the blade, that is $\theta(r) = \theta_0 + r\theta_{rate}$ could be considered. Substituting in the integral leads to:

$$C_T = \frac{1}{2} c_{L\alpha} \left(\frac{\theta_0}{3} + \frac{\theta_{rate}}{4} - \frac{\lambda}{2} \right) \quad (2.35)$$

An interesting result may be obtained if the reference angle for the twist distribution is taken at the 75% of the blade, $\theta = \theta_{0.75} + (r - 0.75)\theta_{rate}$. In this case the thrust coefficient turns out to be:

$$C_T = \frac{1}{2} c_{L\alpha} \left(\frac{\theta_{0.75}}{3} - \frac{\lambda}{2} \right) \quad (2.36)$$

From equation (2.36), it can be seen how a linear twisted blade produces the same amount of thrust as a straight blade having a constant pitch angle equal to $\theta_{0.75}$.

2.2.1 Tip loss factor

Previously, the parameter B was introduced to consider the loss of lift production in the blade sections near the tip. This implies the evaluation of the integral for the thrust coefficient in a smaller interval:

$$C_T = \int_0^B \frac{1}{2} \sigma c_L r^2 dr = \frac{1}{2} \sigma c_{L\alpha} B^2 \left(\frac{\theta_0 B}{3} - \frac{\lambda}{2} \right) \quad (2.37)$$

The use of B causes a reduction in the produced thrust of about 6%-10% [24]. A more correct approach for modeling the tip losses is to make use of the Prandtl tip loss factor which allows a variation in the induced velocity distribution [25]. In his work, Prandtl modeled the helicoidal vortex sheet representing the wake region as a series of parallel vortex sheets at a distance d_f . Then, with the use of conformal mapping, Prandtl studied the problem in a simplified geometrical domain. Finally, his work can be resumed in two important formulas, defining the Prandtl tip loss factor F and the parameter f :

$$F = \frac{2}{\pi} \arccos(\exp(-f)) \quad (2.38)$$

$$f = \frac{n_b}{2} \arccos \frac{1-r}{\lambda(r)} \quad (2.39)$$

It can be derived from the equations 2.38-2.39 that F decreases for rotors having less blades. Due to the tip effects, a real rotor has an induced velocity greater than the ideal value, which implies a growth in the induced power and leads to a decrease of the FM. This fact can be verified by implementing the BET in Matlab. The graph of figure 2.5 shows the different distribution of induced velocity along the blade due to the tip loss factor. Since F is a function of the induced velocity, its determination comes from an iterative scheme, which will be treated in the next section.

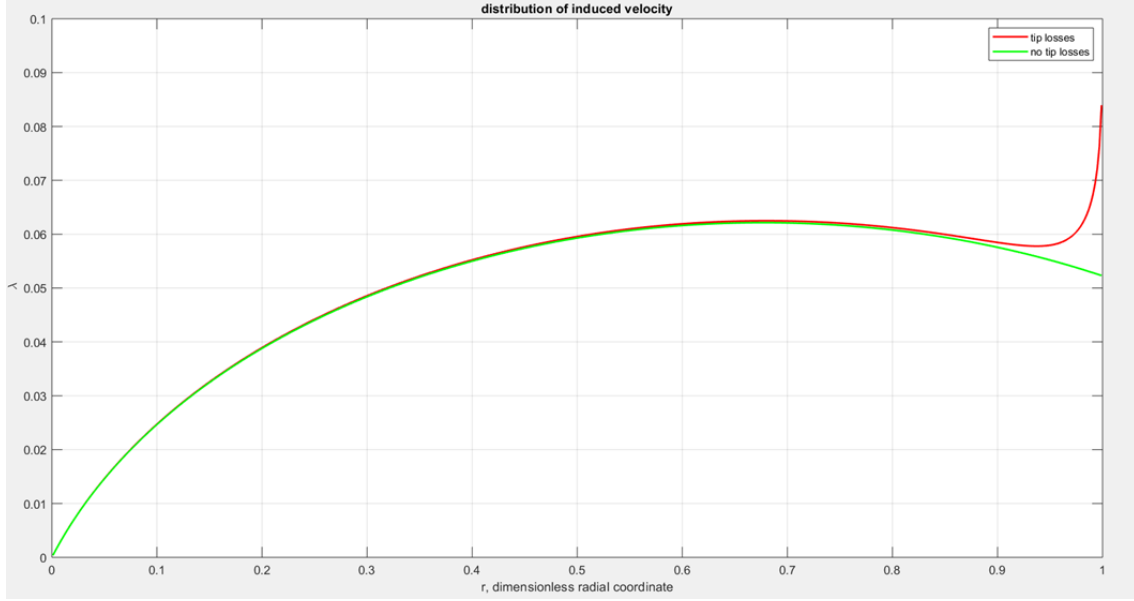


Figure 2.5: Distribution of induced velocity with or without the consideration of the tip loss factor

2.3 Blade Element and Momentum Theory

The union of the BET with some aspects of the Momentum theory gives us a way to numerically determine the induced velocity distribution, and therefore to obtain the geometric characteristics of a blade to fulfill known requirements. First, a generic ring of the rotor disk shall be assumed. The momentum theory states that $dT = 2d\dot{m}v_i$ where $d\dot{m} = \rho(v_c + v_i)2\pi y dy$, so that the equation becomes $dT = 4\rho\pi(v_c + v_i)v_i y dy$. With applying the dimensionless quantities [24]:

$$dC_T = 4\lambda\lambda_i r dr; \text{ hovering case} \rightarrow dC_T = 4\lambda^2 r dr \quad (2.40)$$

$$dC_{P,i} = \lambda dC_T = 4\lambda^3 r dr \quad (2.41)$$

The integration along the entire blade results into equations (2.42) for hovering case:

$$C_T = \int 4\lambda^2 r dr, \quad C_{P,i} = \int 4\lambda^3 r dr \quad (2.42)$$

These two expressions have universal value and are valid for a generic induced-velocity distribution. Now it is possible to compare the infinitesimal thrust coefficient obtained with the momentum theory and with the BET. As a result, a formulation for the determination of the induced velocity field will be obtained.

$$dC_T = \frac{1}{2}\sigma c_L r^2 dr = \frac{1}{2}\sigma c_{L\alpha} \left(\theta - \frac{\lambda}{r} \right) r^2 dr = 4\lambda\lambda_i r dr \quad (2.43)$$

Substitution into function of λ leads to:

$$\lambda^2 + \lambda \left(\frac{\sigma c_{L\alpha}}{8} - \lambda_c \right) - \frac{\sigma c_{L\alpha}}{8} \theta r = 0 \quad (2.44)$$

$$\lambda(r, \theta, \lambda_c) = -\left(\frac{\sigma c_{L\alpha}}{16} - \frac{\lambda_c}{2}\right) + \sqrt{\left(\frac{\sigma c_{L\alpha}}{16} - \frac{\lambda_c}{2}\right)^2 + \frac{\sigma c_{L\alpha} \theta r}{8}} \quad (2.45)$$

By inserting the tip losses through the Prandtl factor, the latter expression appears in the following form:

$$\lambda(r, \theta, \lambda_c) = -\left(\frac{\sigma c_{L\alpha}}{16F} - \frac{\lambda_c}{2}\right) + \sqrt{\left(\frac{\sigma c_{L\alpha}}{16F} - \frac{\lambda_c}{2}\right)^2 + \frac{\sigma c_{L\alpha} \theta r}{8F}} \quad (2.46)$$

The numerical routine for solving the BEMT permits to determine the rotor characteristics, having a thrust coefficient to be reached and the basic rotor geometry: blade length, root chord, twisting rate, as input.

2.3.1 Forward flight

At this point, the focus lies on the BET treatment of the forward flight. The aircraft will be moving in the space, so that the forward velocity needs to be taken into account when using a generic blade station. The assumptions made previously are still valid: for the determination of aerodynamic loads only the velocity perpendicular to the leading edge will be considered, and the actual angle of attack will differ from the simple pitch angle [24]. Keeping figure 2.4 in mind, the following relations for the velocities acting on a generic blade element and for the developed aerodynamic forces are applicable:

$$U = \sqrt{U_T^2 + U_P^2} \approx U_T \quad (2.47)$$

$$\alpha = \theta - \phi = \theta - \arctan \frac{U_P}{U_T} \approx \theta - \frac{U_P}{U_T} \quad (2.48)$$

$$dL = \frac{1}{2} \rho c c_{L\alpha} (\theta U_T^2 - U_P U_T) dy \quad (2.49)$$

$$dD = \frac{1}{2} \rho U^2 c c_D dy \quad (2.50)$$

where U is the air velocity at a generic blade element, that can be decomposed in the component parallel to the rotor disk U_T and in the component perpendicular to the rotor disk U_P .

In this case, the assumption that the lift coefficient is linearly dependent from the angle of attack is kept. Decomposing the aerodynamic resultant with respect to x-axis and z-axis, results into the two following expressions:

$$dF_x = dD \cos \phi + dL \sin \phi \approx dD + \phi dL \approx \frac{1}{2} \rho c c_{L\alpha} \left(\frac{c_D}{c_{L\alpha}} U^2 + \theta U_P U_T - U^2 \right) dy \quad (2.51)$$

$$dF_z = dL \cos \phi - dD \sin \phi \approx \frac{1}{2} \rho c c_{L\alpha} (\theta U_T^2 - U_P U_T) dy \quad (2.52)$$

velocity ΩR .



(b) Forward flight, $\mu = 0.3$

$$U_T(y, \psi) = \Omega y + v_\infty \sin \psi = \Omega y + \mu \Omega R \sin \psi \quad (2.53)$$

$$U_p = (\lambda_i + \lambda_c)\Omega R + y\dot{\beta}(\psi) + \mu\Omega R\beta(\psi)\cos\psi \quad (2.54)$$

$$U_R = \mu\Omega R \cos\psi \quad (2.55)$$

their dimensionless form:

$$\frac{U_T}{\Omega R} = r + \mu \sin \psi \quad (2.56)$$

$$\frac{U_P}{\Omega R} = \lambda \quad (2.57)$$

$$\frac{U_R}{\Omega R} = \mu \cos \psi \quad (2.58)$$

Substituting these formulations in the equations of the thrust coefficient, leads to:

$$dC_T = \frac{1}{2} \sigma c_L \cos \phi (r + \mu \sin \psi)^2 dr - \frac{1}{2} \sigma c_D \sin \phi (r + \mu \sin \psi)^2 dr \quad (2.59)$$

In forward flight there are some other sources of power consumption. In fact, apart from the profile power and the induced power, the presence of reverse flow at certain regions of the blade has to be considered when it is on the retreating side of rotation. The reason for that lies in the increase of the power consumption due to the incoming airflow from the trailing edge at some parts of the blade for certain values of forward velocity (see figure 2.6). This region of reverse flow increases when the speed of the flight increase. Moreover, the parasitic drag of the aircraft fuselage must be considered.

$$dC_{P_{PROFILE}} = \frac{1}{2} \sigma (r + \mu \sin \psi)^3 (c_L \sin \phi + c_D) \quad (2.60)$$

$$dC_{P_i} = \frac{1}{2} \sigma (r + \mu \sin \psi)^2 \lambda c_L dr \quad (2.61)$$

$$dC_{P_{REVERSE}} = -\frac{1}{2} \sigma (r + \mu \sin \psi)^3 c_D dr \quad (2.62)$$

These three terms must be integrated along the blade as well as for every azimuthal position of the blade itself. Then, the parasitic contribute must be added:

$$dC_{P_{PARASITIC}} = \frac{1}{2} \left(\frac{f'}{A} \right) \mu^3 \quad (2.63)$$

here, A is the rotor disk area, while f' is the equivalent wetted area and accounts for the drag of all the aircraft parts.

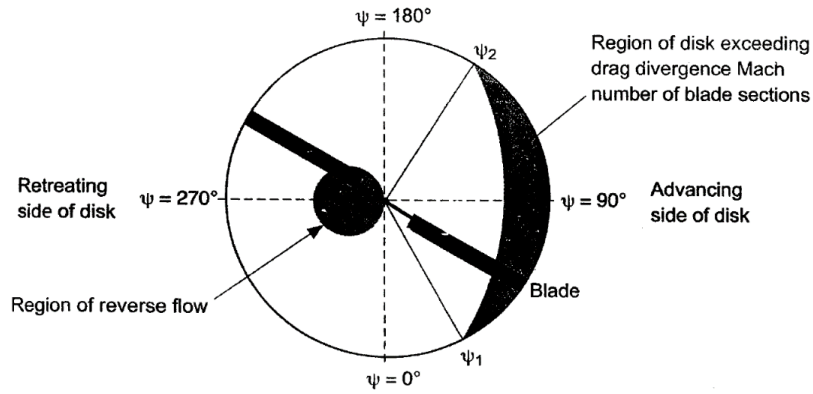


Figure 2.7: Reverse flow in forward flight. From [24]

2.3.2 Modeling the inflow

In order to obtain a preliminar performance estimate for the forward flight, the modeling of the inflow is required. These models derive from extrapolation of experimental data. This is due to the fact that the induced velocity greatly depends on the complex aerodynamic configurations of the wake region. At the center of the rotor disk, the value derived by means of the Momentum theory is taken [24]:

$$\lambda_0 = \frac{c_T}{2\sqrt{\mu^2 + \lambda_i^2}} \quad (2.64)$$

Then, a linear development of the inflow is assumed. Glauert proposed the following formulation:

$$\lambda_i = \lambda_0 (1 + k_x r \cos \psi) \quad (2.65)$$

Many different ways of calculating the parameter k_x have been presented in the past. A very common one is

$$k_x = \tan\left(\frac{\chi}{2}\right), \text{ where } \chi = \tan^{-1}\left(\frac{\mu_x}{\mu_z + \lambda_i}\right) \quad (2.66)$$

χ represents the wake skew angle which gives information about the inclination of the wake region with respect to the advancing direction, μ_x is the advance ratio projected onto the rotor plane, while μ_z is the advance ratio projected orthogonally to the rotor plane.

Other models consider a variation of the induced velocity field not only along the direction of the rotor $\psi = 0^\circ - 180^\circ$ but also along the direction $\psi = 90^\circ - 270^\circ$ (lateral variation of the inflow). In this case, the introduction of a new parameter k_y is needed, for example the Dree's model in which $k_x = \frac{4}{3} \left(\frac{1 - \cos\chi - 1.8\mu^2}{\sin\chi} \right)$ and $k_y = -2\mu$. The model chosen for the Matlab implementation of the BEMT applied to the forward flight is Pitt & Peter's, as suggested in [24], in which $k_x = \frac{15\pi}{23} \tan \frac{\chi}{2}$ and $k_y = 0$.

3 Matlab implementation of BET and BEMT theories

Two Matlab programs were implemented using the BET as well as the BEMT in order to predict the performances of rotors and to understand the effect of changing different geometrical parameters. At first, the validity of the written program was checked for normal scale rotors, comparing the results with data taken from [24], and supplemented by experimental data taken from the UH-60A helicopter [26], and from other experimental tests [27]. Then, the program 2 was tested for sub-scale rotors by modifying the way of treating the low Re number, that becomes very important at these scales.

3.1 Insertion of the curvature variation in the BEMT

At first an analytical approach is developed in order to include the curvature effect on the BET. The requirements for that are the following:

- possibility of changing the curvature parameters in a quick way for the sensitivity analysis
- easy linking with Matlab BEMT code

There are different ways available of introducing a curved blade, for example by inserting a union of two ellipses, two parabolas, two circumferences or a mix of these conics to represent the mid-chord points spatial development. It is decided to use two circumferences, since in this way it is easier to calculate the component of the velocity that is locally perpendicular to the leading edge in radial directions. Moreover, by changing the radius of the circumferences, it is possible to change the type of curvature of the blade, thus having the possibility of checking different configurations. The position of the maximum

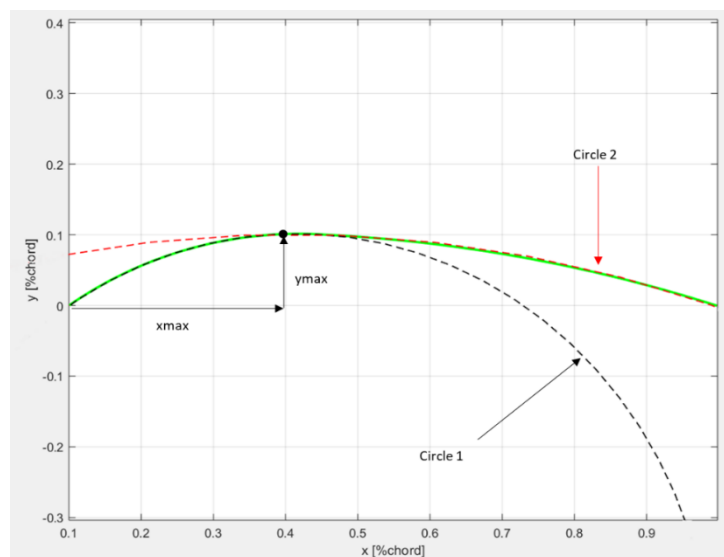


Figure 3.1: Calculation/Modeling/Results of curvature with two circumferences. The green line represents the total blade curvature, sum of the two circumferences (black and red lines respectively)

is inserted through its coordinates expressed in percentage of the blade length. In this way, the first circumference is constrained to pass through the starting curvature point as well as the maximum point, while the second circumference is constrained to pass through the maximum and the ending curvature point. By imposing these conditions, an iterative procedure is set to determine the unknown parameters, namely the radius and the coordinates of the center. Referring to figure 3.1 for the meaning of the symbols, a total curved blade (TE1B) which presents an y_{max} of $0.1R$ located at the 75% of blade length, while the curvature radii are $2.6R$ and $0.28R$ respectively is modeled. Moreover, a single curved blade (SCB) is defined, which presents a starting curvature point at 70% of the blade radius R and is characterized by a dimensionless curvature radius of $0.47R$. These geometric characteristics are kept also for the definition of the models to be investigated with the CFD approach, see section 4.5, and see table 3 for the nomenclature used to address each rotor.

After the blade spatial development determination, an analytical procedure needs to be set to take the curvature in the calculations into account, following the BEMT approach. To do so, a generic blade is divided into $n - 1$ elements, n being the number of vertices, each element has the constant length dr . The element position is located at $\frac{r}{2}$ from the LE. Taking the generic j -th blade element into consideration, it is possible to define its inclination with respect to the axis that links the rotational axis to the tip of the blade (angle ζ) and the inclination of the vector linking the center of the element with the center of rotation, again with respect to the previous axis (angle β).

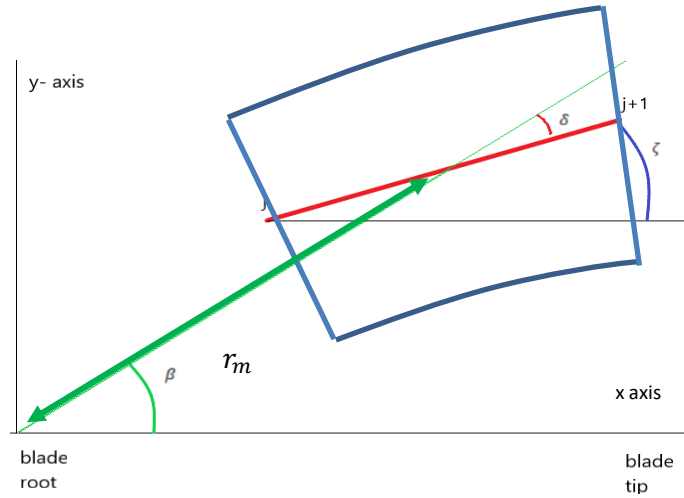


Figure 3.2: Inclination of a generic blade element with respect to the radial direction

Considering the extremes of the blade elements j and $j + 1$, the following angles can be defined:

$$\zeta = \text{atan} \left(\frac{y_{j+1} - y_j}{x_{j+1} - x_j} \right) \quad (3.1)$$

$$\beta = \text{atan} \left(\frac{y_m}{x_m} \right) \quad (3.2)$$

In equation 3.2 x_m and y_m are the coordinates of the blade element center.

Every blade element is moving with a velocity that is orthogonal to the radius linking the center of the element with the center of rotation (r_m). Defining the angle $\delta = \beta - \zeta$ a formulation for the velocity of each element can be found, as to be seen in figure 3.3:

$$v_p = \Omega a = \Omega \left[r_m^2 + \frac{c^2}{4} + r_m c \sin(\delta) \right]^{0.5} \quad (3.3)$$

For the aerodynamics the main interest lies in the velocity perpendicular to the leading edge (v_{inc}), that can be written in its dimensionless form and on the effective aerodynamic angle of attack:

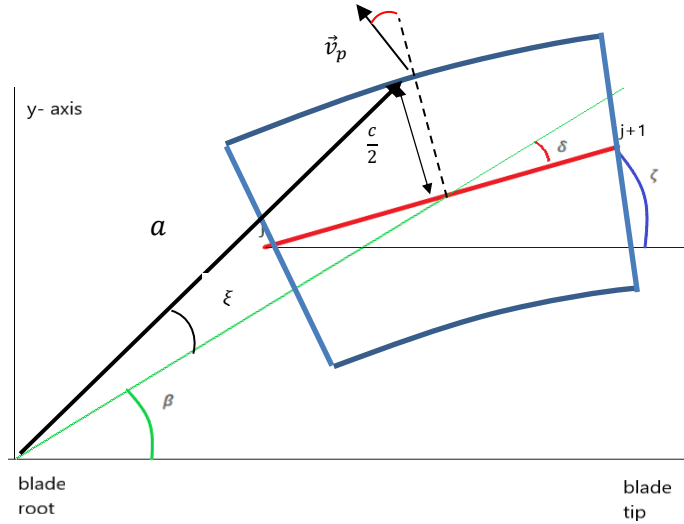


Figure 3.3: Determination of the velocity component perpendicular to the LE for a curved blade

$$v_{inc} = v_p \cos(\xi + \delta) = \Omega \left[r_m^2 + \frac{c^2}{4} + r_m c \sin(\delta) \right]^{0.5} \cos(\xi + \delta) \quad (3.4)$$

$$\lambda_{inc} = \left[r_s + \frac{c^2}{4R^2} + r_s \frac{c}{R} \sin(\delta) \right]^{0.5} \cos(\xi + \delta) \quad (3.5)$$

$$\xi = \beta - \arccos \left(\frac{r_m \cos(\beta) - \frac{c}{2} \sin(\zeta)}{a} \right) \quad (3.6)$$

$$\alpha = \theta - \phi = \theta - \arctan \left(\frac{\lambda}{\left[r_s + \frac{c^2}{4R^2} + r_s \frac{c}{R} \sin(\delta) \right]^{0.5} \cos(\xi + \delta)} \right) \quad (3.7)$$

Where v_{inc} is the velocity perpendicular to the leading edge, λ_{inc} is its dimensionless form, r_s is the dimensionless radial position of the element and ξ is the angle between the vectors a and r_m .

These equations lead to the following values for the elementary contributes dc_T and dc_P :

$$dc_T = \frac{\frac{1}{2} \sigma \lambda_{inc}^2 [c_L \cos(\phi) - c_D \sin(\phi)] dr}{\cos(\zeta)} \quad (3.8)$$

$$dc_P = \frac{\frac{1}{2} \sigma \lambda_{inc}^3}{\cos(\zeta)} [c_L \sin(\phi) + c_D \cos(\phi)] dr \quad (3.9)$$

The length of the j-th blade element is $\frac{dr}{\cos(\zeta)}$.

Furthermore, the formulation for the induced velocity for hovering condition is:

$$\lambda = -\frac{\sigma\lambda_{inc}c_{L\alpha}}{16r_s\cos(\zeta)F} + \sqrt{\left(\frac{\sigma\lambda_{inc}c_{L\alpha}}{16r_s\cos(\zeta)F}\right)^2 + \frac{\sigma\lambda_{inc}^2\theta}{8r_s\cos(\zeta)F}} \quad (3.10)$$

3.2 Calculation of aerodynamic properties

For the implementation of BET and BEMT theories in Matlab, there was the need of determining the values of lift and drag coefficients for different angles of attack, once the shape of the airfoil was chosen. These behaviors depend strongly on the Re number. In order to plot the lift polar and the drag polar while giving the user the option to choose the profile shape, Reynolds regime, and a discrete number of angles of attack, the software XFOIL was chosen for the calculations. This program uses a modified panel method to calculate these quantities and is able to well predict the transition from laminar to turbulent flow regime, as well as to define the formation of separation bubbles. More information about XFOIL can be found in [28], [29]. A Matlab function has been developed which allows to manage XFOIL directly from the Matlab Command Window: after selecting the desired profile, the Re regime and the angles of attack, the function *polyfit* creates the interpolant polynomials. In this way, it is possible to extrapolate the values of c_L and c_D for every angle of attack at which a blade station is subjected. Figure 3.4 shows the great influence that Re has on the aerodynamic properties of airfoils, and how the performances deteriorate as Re decreases. As mentioned in chapter 1, as the Re decreases, a decay in the aerodynamic performances is noticed. In section 3.5.2 this argument will be treated with more details.

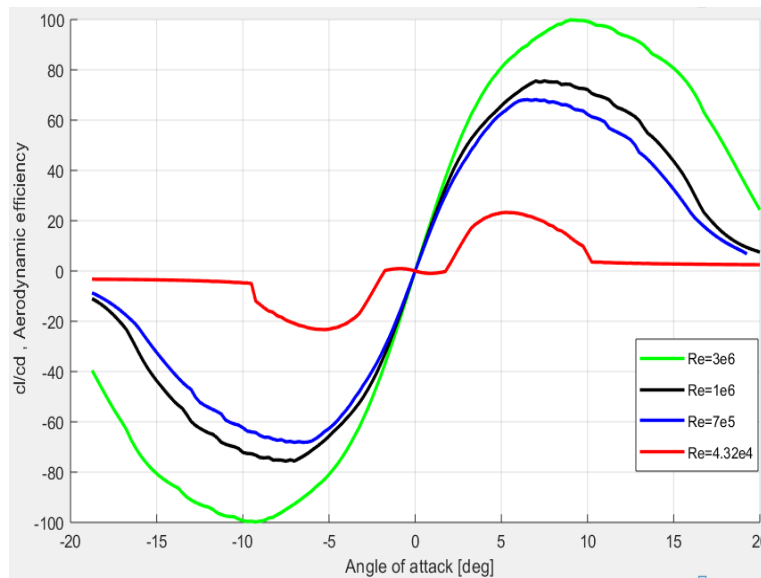


Figure 3.4: Aerodynamic efficiency vs angle of attack at different Reynolds numbers for NACA 0012 airfoil. Data obtained with the program XFOIL

3.3 Method 1

3.3.1 Hovering and axial flight

The first developed program iterates on the geometric parameters of the rotor in order to obtain a desired thrust coefficient. Different parameters can be changed or kept fixed, based on the user intent. As input, it is possible to choose between hovering flight condition or axial flight condition. Further, the desired thrust coefficient must be set as well as some geometric features, like the number of blades, the blade radius and the chord at the root. Then, some specifications for the design are requested: in fact, the amount of tapering and the twisting rate must be specified. Through iteration, the program will find the root pitch angle needed to produce the amount of required thrust. The program manages the rate of tapering by incrementing the value of the tip chord. The program also calculates the power coefficient and Figure of Merit (equations 2.32 and 2.14), as well as the induced velocity distribution.

In the case of a constant chord c the step to be followed are:

- 1) Blade division in N elements, each of length dr
- 2) Hypothesis of θ_0 , and definition of twist distribution
- 3) Determination of the induced velocity at each j -th element

$$\lambda_{i,j}(r_j, \theta_{i,j}, \lambda_c) = -\left(\frac{\sigma c_{L\alpha}}{16F_{i,j}} - \frac{\lambda_c}{2}\right) + \sqrt{\left(\frac{\sigma c_{L\alpha}}{16F_{i,j}} - \frac{\lambda_c}{2}\right)^2 + \frac{\sigma c_{L\alpha} \theta_{i,j} r_j}{8F_{i,j}}} \quad (2.46)$$

$$f_{i+1,j} = \frac{n_b}{2} \arccos\left[\frac{1 - r_j}{\lambda_{i,j}(r_j)}\right] \quad (2.38)$$

$$F_{i+1,j} = \frac{2}{\pi} \arccos(e^{-f_{i+1,j}}) \quad (2.39)$$

- 4) Determination of the thrust and power contributes at every blade station

$$dC_{Ti,j} = \frac{\sigma c_{L\alpha}}{2} (\theta_{i,j} r_j^2 - \lambda(r_j) r_j) dr \quad (2.43) \quad dC_{Pi,j} = dC_{Ti,j} \lambda_{i,j} \quad (2.9)$$

- 5) Determination of global performance parameters

$$C_{Ti} = \sum_{j=1}^N dC_{Ti,j} \quad (3.11) \quad C_{Pi} = \sum_{j=1}^N dC_{Pi,j} + \frac{\sigma c_{D,0}}{8} \quad (3.12)$$

- 6) Check if $abs(C_{Ti} - C_{T,obj}) < tol$. Otherwise, determine the new pitch angle at the root.

A recommended way for determining the $\theta_{0,i+1}$ angle for the successive iteration are iterative steps [24]:

$$\theta_{0,i+1} = \theta_{0,i} + \left[\frac{6(C_{T,obj} - C_{T,i})}{\sigma c_{L\alpha}} + \frac{3\sqrt{2}}{4} \left(\sqrt{C_{T,obj}} - \sqrt{C_{T,i}} \right) \right] \quad (3.13)$$

This routine converges with few iterations, and it gives good results when compared with experimental data for helicopter scale rotors (see figure 3.6). To obtain results more similar to actual rotors, the

insertion of the Prandtl tip loss factor is needed. F is obtainable numerically, since it is strictly linked to the values assumed by λ (see equations 2.38-2.39). This approach is good for comparing different rotors having the aim of producing the same thrust. An example of comparison is now given: a rotor formed by two rectangular untwisted blades, characterized by a solidity $\sigma = 0.1$ and aiming to produce in hovering a thrust defined by the value of the coefficient $C_T = 0.008$ is compared with two rotors having blades

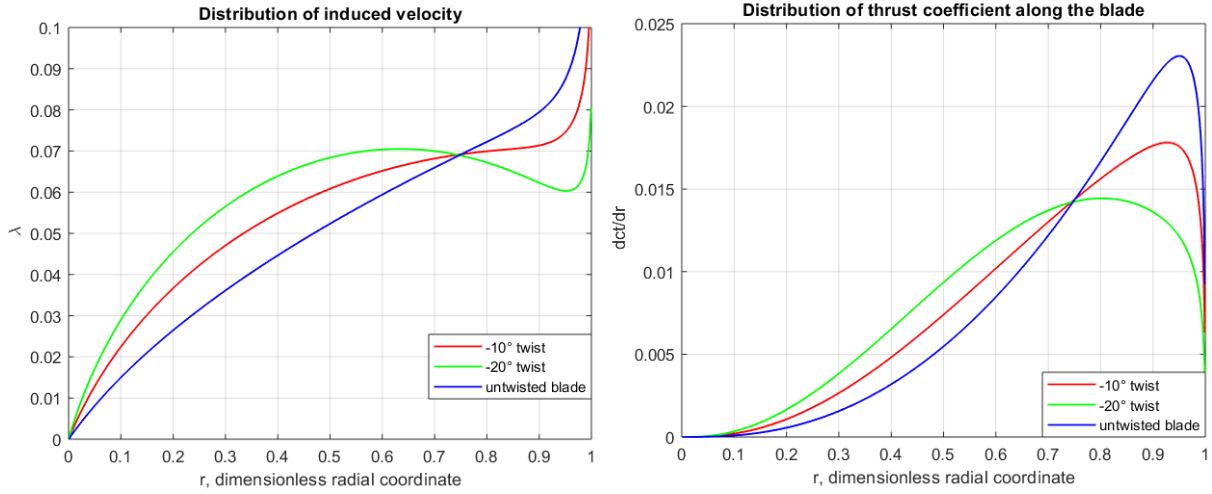


Figure 3.5: Distribution of induced velocity and thrust coefficient for three different types of blade, having different rate of twisting amounts

with a twisting rate of $\theta_{rate,1} = 10^\circ/m$, $\theta_{rate,2} = 20^\circ/m$. The loss of efficiency at the tip of the blades is considered through the Prandtl's tip loss function, whereas the Re is set to $3 \cdot 10^6$, typical for helicopter scale rotors. The three different root pitch angle needed to reach the objective are respectively $\theta_{0,10^\circ twist} = 18^\circ$, $\theta_{0,20^\circ twist} = 25.3^\circ$, $\theta_{0,untwisted} = 10.4^\circ$, for the rotor considered. The Figure of Merit calculated for the three blades is $FM_{untwist} = 0.76$; $FM_{10^\circ twist} = 0.81$; $FM_{20^\circ twist} = 0.83$ which clearly underlines the benefits the insertion of twisting has in the performances of helicopter rotors. As the value of twist rate increases the region of greater lift production moves inwards, and the induced velocity distribution becomes more regular. At the end of the blade, in each case there is a huge decrease in thrust production, caused by the presence of tip vortices, which effects is modeled through the Prandtl tip loss function (see figure 3.5).

3.3.2 Forward flight

In the case of forward flight, the calculations are made for a number of blade azimuthal positions in order to achieve an accurate description of the problem. 300 azimuthal positions are chosen, separated by a constant angle of 1.2° : the implemented procedure is described in the paragraph 2.3.1. In his work, Marco Lonoce [30] found by a sensitivity analysis that the minimum number of azimuthal positions is 100, to well describe the problem of forward flight. It is also clear that increasing the number of positions tested would have brought to a better refinement in the results, so this was done. Each parameter like induced velocity, angle of attack, will be described by a matrix having the number of azimuthal and radial position as rows and columns respectively. For example, taking into account 300 azimuthal position and a blade division in 500 blade elements, the parameters matrices will have the dimension 300×500 .

3.3.3 Method 1 verification

In order to verify the correctness of the results obtained with the code, a comparison with some data available in literature is made. For the hovering condition, the program output is confronted with the

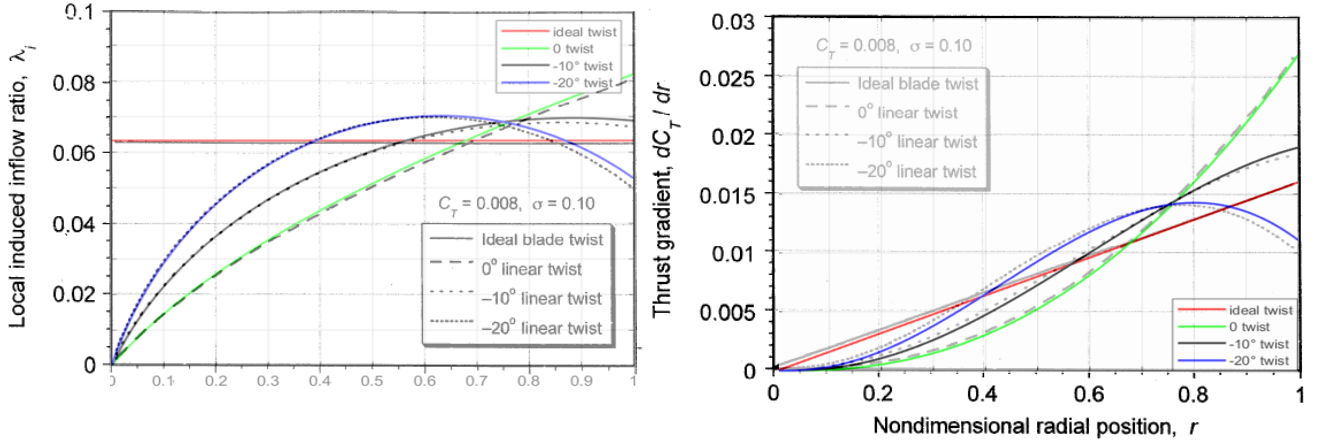


Figure 3.6: Comparison between BEMT results obtained by Leishman and the Matlab code developed. Edited from [24]

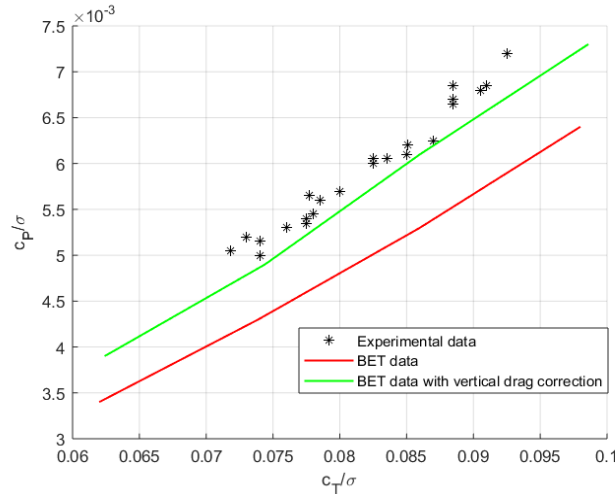


Figure 3.7: Comparison between experimental data and theoretical data for the Wessex helicopter in hover condition

graphs representing the behavior of thrust production and induced velocity in reference [24], [27]. The graphs of figure 3.6, in which the colored lines represent the calculated results, show the good accordance with Leishman results. These graphs are obtained without considering the tip losses, in fact, there is no sudden decrease in the thrust production getting closer to the tip, which happens in reality. As the twisting rate is increased, the induced velocity assumes a more constant value, becoming closer to the ideal case (horizontal line). The second verification is realized by comparing the theoretical results with the experimental data of the Wessex helicopter, measured at RAE Bedford [27]. The Wessex main rotor has four blades, each one having a NACA 0012 profile, a chord length of 0.417 m, a radial dimension of 8.53 m and an 8°/m twisting rate. The angular velocity kept for the tests is 230 RPM. The theoretical results shown in figure 3.7 are well improved by the insertion of vertical drag contribute, which is expressed following the correction presented in [27].

The verification of forward flight results is made by simulating the main rotor of the Sikorsky UH-60A Black Hawk as it is one of the most tested helicopters, thus there exists a high availability of data [26].

In table 1, the characteristics of the main UH-60A rotor are presented. To simplify the analysis, only the SC1095 airfoil is studied, whereas the non-linear twisting rate is replaced by a linear variation equal to $\theta_{rate} = -16^\circ$.

Table 1: UH-60A main rotor characteristics

Radius [m]	8.1788
Chord [m]	0.5273
Number of blades	4
Airfoil used	SC1095, SC1094R8
Rate of twist [°]	Non – linear
Helicopter's weight [kg]	8322.4
f	0.04
A_{eq}	4.65

Five values of advance ratio are tested in the Matlab code, namely $\mu = 0.075; 0.15; 0.25; 0.3; 0.4$. The calculation of aerodynamic properties is made in 300 azimuthal positions to ensure an accurate representation of the problem. The results, shown in figure 3.8, are in good agreement with the experimental data. Conclusively, the program is valid for normal scale rotors, both in hovering and forward flight condition.

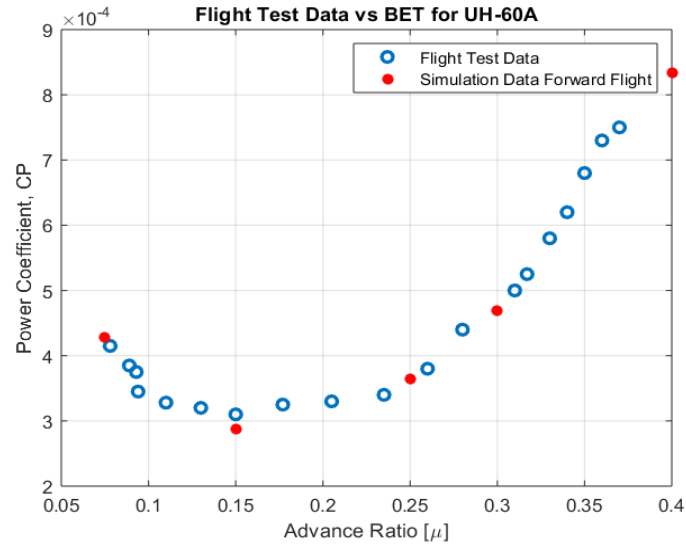


Figure 3.8: Comparison between experimental data and simulation data for UH60A main rotor

3.4 Method 2

For the purpose of the thesis, a different approach is needed that is more suitable for the experimental procedure, in which already designed rotors would be tested. In this case, the program input can be divided in flight conditions input, rotor geometric input and convergence input. The specifications of the flight conditions comprise:

- specification of the air density ρ and air viscosity μ , required for Re determination
- specification of the flight type: *hovering*, *axial flight*, *forward flight*. In case of hovering, the angular velocity is required; for the axial flight, also the climbing velocity is needed, while for the forward flight the advance velocity is required.

The geometric inputs are the data required for the rotor design. The basic ones are the radial dimension of the blade, the chord dimension and the root pitch angle. If it is desired to add a twisting or a tapering of the blade, more information must be provided, like the twist rate or the position at which the taper starts, and its value. Further, the number of blade elements desired for the calculation is required. The convergence inputs are the maximum number of iteration that the program can realize when trying to obtain the induced velocity distribution, and the tolerance value tol . Assuming that the error during the iterative process is $scarto = \max(\lambda_{i+1,j} - \lambda_{i,j})$, the convergence is reached when $abs(scarto) < tol$. The tolerance value is set to $1 \cdot 10^{-6}$. The outputs of the program are the FM as well as the thrust and power coefficient. Moreover, it is possible to plot the behavior of induced velocity, tip loss function, angle of attack and thrust production along the blade, in order to investigate how changes in the rotor geometry influences these parameters. The steps taken in case of hovering condition for a straight blade are:

- 1) Input definition
- 2) Blade division in N stations, each of length dr
- 3) Definition of θ, σ at each blade station, and of the initial vectors (f, F, λ)
- 4) Iterative determination of the induced velocity distribution (to be done at every j -th radial position)

$$\lambda_{i,j}(r_j, \theta_j, \lambda_c) = -\left(\frac{\sigma c_{L\alpha}}{16F_{i-1,j}} - \frac{\lambda_c}{2}\right) + \sqrt{\left(\frac{\sigma c_{L\alpha}}{16F_{i-1,j}} - \frac{\lambda_c}{2}\right)^2 + \frac{\sigma c_{L\alpha} \theta_j r_j}{8F_{i-1,j}}} \quad (2.46)$$

$$f_{i+1,j} = \frac{n_b}{2} \arccos\left[\frac{1 - r_j}{\lambda_{i,j}(r_j)}\right] \quad (2.38)$$

$$F_{i+1,j} = \frac{2}{\pi} \arccos(e^{-f_{i+1,j}}) \quad (2.39)$$

$$scarto = \max(\lambda_{i,j} - \lambda_{i-1,j}) \quad (3.14)$$

- 5) Determination of ϕ and α at each blade station

$$\phi_j = \arctan\left(\frac{\lambda_j}{r_j}\right), \alpha_j = \theta_j - \phi_j \quad (3.15)$$

- 6) Determination of c_L and c_D through the interpolant polynomials calculated from XFOIL data

$$c_{Lj} = \text{polyval}(P_{cL}, \alpha_j) \quad (3.16) \quad c_{Dj} = \text{polyval}(P_{cD}, \alpha_j) \quad (3.17)$$

- 7) Determination of thrust and power contributes of every blade station

$$dC_{Tj} = \frac{1}{2} \sigma r_j^2 (c_{Lj} \cos \phi_j - c_{Dj} \sin \phi_j) dr \quad (3.18) \quad dC_{Pj} = \frac{1}{2} \sigma r_j^3 (c_{Lj} \sin \phi_j + c_{Dj} \cos \phi_j) dr \quad (3.19)$$

8) Determination of global parameters

$$C_T = \sum_{n=1}^N dC_T \quad (3.11) \quad C_P = \sum_{n=1}^N dC_P \quad (3.20) \quad FM = \frac{C_T^{1.5}}{\sqrt{2}C_P} \quad (3.21)$$

In case of forward flight conditions, the formulas used are the one described in the section 2.3.1.

3.5 BET for small scale propellers

The aim is to use the method 2 to investigate the low Re performances of drone rotors, and eventually to insert the presence of a curved LE. At first, the interpolation of XFOIL data is presented; then, two different approaches are used for the determination of propeller performances: firstly, a constant Re approach similar to the one commonly used for normal scale rotors is used, by considering the Re at 75% of the blade length as the operative Re for the entire rotor. Secondly, a different approach is developed, in order to ensure that blade elements work inside a more correct Re interval, because this strongly affects the aerodynamic coefficients.

3.5.1 Interpolation of XFOIL data

For the propeller being studied, characterized by a chord of 20 mm and a radius of 120.44 mm, the Re number varies linearly between 0 and $5.2 \cdot 10^4$. Figure 3.9 presents the variation of lift coefficient inside this specific interval, obtained at discrete angles of attacks through XFOIL. This graph makes obvious that keeping the Re fixed for the entire blade length could cause erroneous results, since the coefficients strongly depend from the Re number. In this sense a method to consider the Re variation along the blade could be preferred.

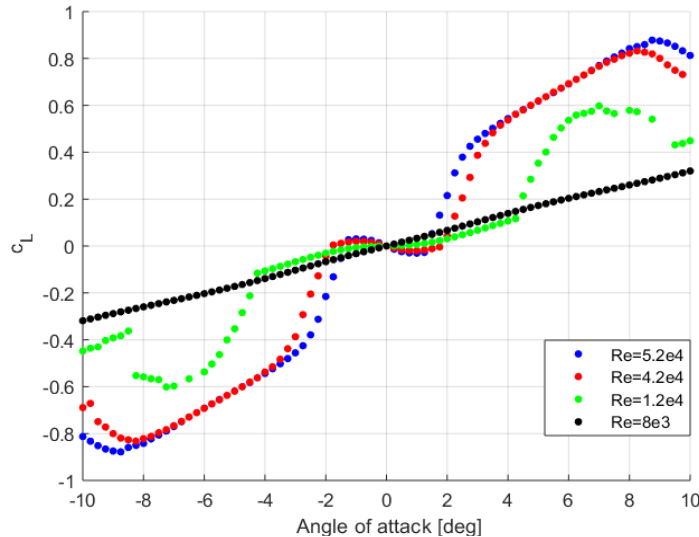


Figure 3.9: Different lift polar for various Re values. The profile is NACA 0012

The nonlinear shape of the curves requires the use of higher degree polynomials for a correct interpolation of data when using the Matlab function *polyfit*. The effect of changing the interpolation is remarkable in the BET, since both lift and drag generated at each blade station are calculated with these

polynomials. In figure 3.10 there are two examples of how various polynomials have different accuracies in the representation of the real behavior. Since the computational time is not influenced by the degree of the polynomials chosen for the interpolation, the degrees for both the lift and the drag case are set high with the aim of reducing this type of error to a minimum. For the lift polar a 14th degree polynomial is used while a 18th degree polynomial is used for the drag's interpolation. Another noticeable aspect is the strong nonlinear behavior for the lift coefficient, which is going to be investigated in the next section.

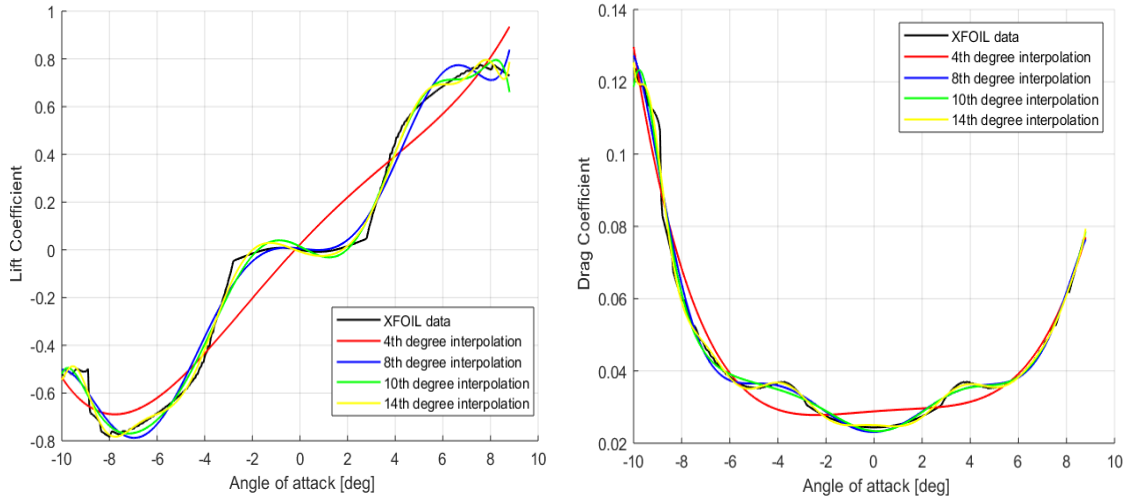


Figure 3.10: Lift and Drag polars interpolation with different polynomials

3.5.2 Non-linearity of lift polar

As mentioned in Chapter 2, the calculation made by BET for the determination of the induced velocity distribution along the blade follows the hypothesis of linear correlation between lift coefficient and angle of attack, which leads to $c_L = c_{L\alpha}(\alpha - \alpha_{L=0})$. It is apparent how different values of $c_{L\alpha}$ lead to different results in the thrust as well as power coefficients and eventually in the rotor FM. The nonlinear behavior depicted in figure 3.10 has been recently studied by scientists both experimentally and numerically, as mentioned in Chapter 1 [16], [17], [18]. In particular, Ohtake and others experimentally tested the

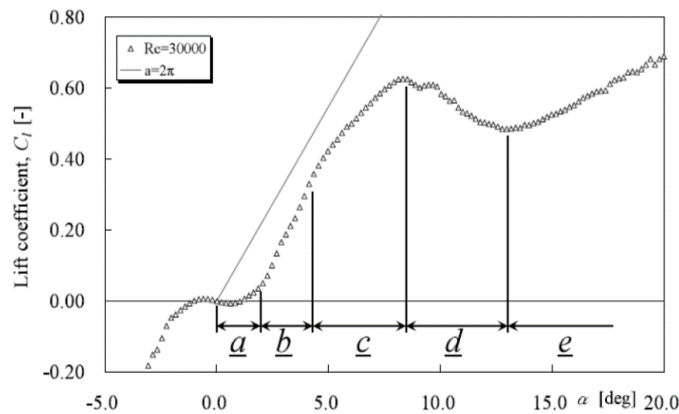


Figure 3.11: Lift polar for NACA 0012 at $Re=30,000$. From [18]

NACA 0012 airfoil in the Re interval $1 \cdot 10^4 < Re < 1 \cdot 10^5$, defining five α intervals which were characterized by different flow features. These intervals are shown in figure 3.11.

- 1st region ($0^\circ < \alpha < 2^\circ$)

When Re is between 25,000 and 70,000 the presence of a negative lift is noticed in this region. In fact, the flow at the upper surface accelerates near the LE, and then it starts decelerating. The same feature can be found in the flow at the lower airfoil surface, but the flow deceleration is less evident, so that a zone of negative lift production can be noticed near the airfoil tail. The reason of this is explained by two aspects. The boundary layer at the upper part of the airfoil separates near the TE, thus reducing the flow velocity, and this elevates the pressure distribution at the upper surface. Moreover, the formation of a reversed flow region behind the TE is noticed, thus violating the Kutta condition. The lower flux tends to move towards the upper surface, thus accelerating and lowering in this way its static pressure. This results in an overall force directed downwards at the TE of the blade and causes the negative lift. In figure 3.12 is possible to see the behavior of the pressure coefficient for $Re=30,000$ (left), as well as the presence of the recirculation region at the airfoil TE (right). Pranesh & others [18] linked the presence of the recirculation region to an equivalent negative-cambered airfoil, which would cause a negative lift.

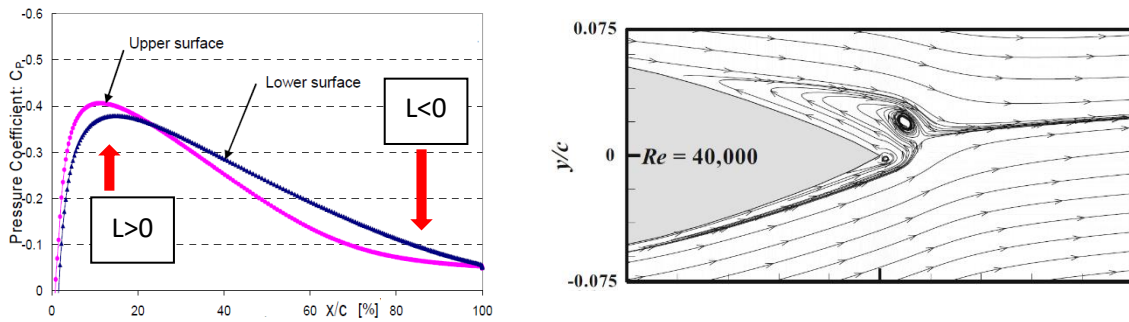


Figure 3.12: To the left, pressure coefficient distribution for the NACA 0012 airfoil at $Re=30,000$ (adapted from [17]). To the right, recirculation region near the TE of the airfoil (from [18]).

As the Re increases, the development of a Karman vortex shedding at the upper part of the TE causes a flux acceleration which is thought to be responsible of the recovering from the negative thrust production. In fact, at $Re=100,000$ there is no negative lift production (see figure 3.13).

- 2nd region ($2^\circ < \alpha < 4.5^\circ$)

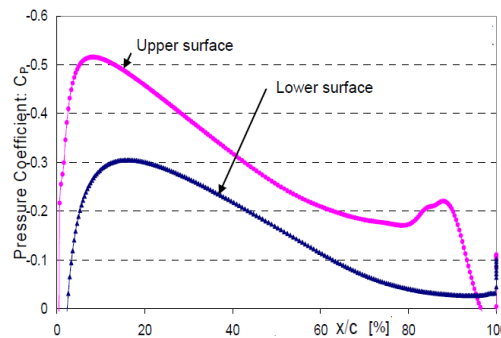


Figure 3.13: Pressure coefficient distribution for NACA 0012 at $Re=100,000$. From [17]

In this region the lift coefficient increases with a slope greater than what would be expected from the thin airfoil theory. This is justified by the formation of vortices near the TE at the upper surface, causing a laminar separation of the flow without reattachment (see figure 3.14).

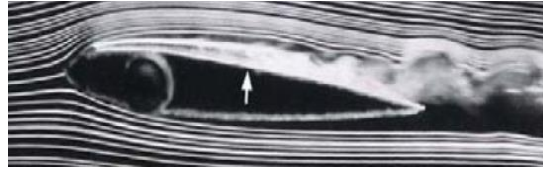


Figure 3.14: Development of vortices at the upper airfoil surface, $Re=23,000$. From [15]

- 3rd region ($4.5^\circ < \alpha < 9^\circ$)

The lift slope decreases, due to the reattachment of the separated flow region at the upper profile surface. After the reattachment there is the genesis of a turbulent boundary layer. The laminar separation bubble being formed moves towards the LE as the α increases [17].

- 4th region ($9^\circ < \alpha < 13^\circ$)

The stall of the profile at low Re is noticed. In fact, to the laminar separation bubble already present at the upper surface, an ulterior fluid separation is present at the TE, causing a decrease in the lift production.

- 5th region ($13^\circ < \alpha < 20^\circ$)

The lift slightly increases, while the flow is completely separated at the upper surface, from the LE. In fact, the laminar separation bubble and the second separation region near the TE melt together. As the α increases, there is a drop in the value of the minimum pressure after the separation point, so that the pressure contribute at the lower surface becomes more important, causing an overall lift increase.

From these studies it is apparent how at low Re the flowfield around the NACA 0012 is greatly affected by slight changes in α , and cannot be approximated with a linear behavior. This fact may cause inaccuracies in the use of BEMT.

3.5.3 Constant Reynolds approach

In the previous sections the Re effects' influence on the aerodynamics of the flow around airfoils at the scale of micro air vehicles (MAVs) has been shown. Recall that the Re assumes values in a range between 0 and $5.2 \cdot 10^4$, for a rotational speed of 3000 RPM. At 75% of the blade, the Re equals $3.88 \cdot 10^4$, therefore this value has been set for all blade stations. The FM variation with the thrust produced is studied by keeping fixed the rotational speed and increasing the root pitch angle. This approach shows a particular result: in fact, for the straight untwisted blade, the thrust coefficient increased with the root pitch angle till a value of $\theta_0 = 16^\circ$, after which it started decreasing. This is due to the nature of the lift curve. In fact, as it is possible to see from figure 3.11 (which is calculated for $Re=30,000$, however a similar shape is obtained for $Re=38,800$) after an angle of attack of 10° there is a decrease in the lift produced, this causing the overall thrust decrease for root angle greater than 16° .

This consideration is confirmed from the study of the angle of attack curve vs radial position of figure 3.15-a: when the root pitch angle is equal to 16° , the part of the blade responsible of the greater thrust production operates at angles above 8° , which correspond to the minimum in the lift curve. A similar behavior is found for the curved blades, and for all the twisted blades, for which the root pitch angle at which the thrust start decreasing is 24.5° .

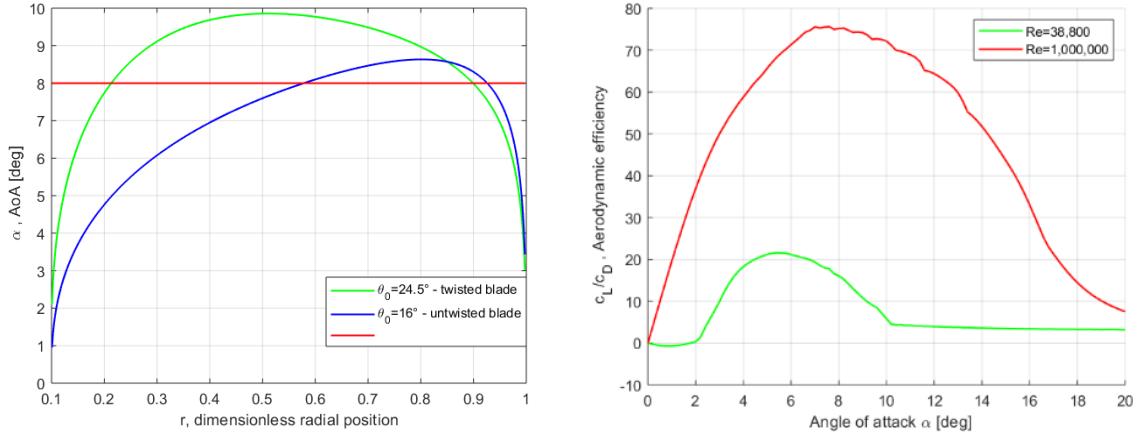


Figure 3.15: (a)-angles of attack for the straight untwisted blade with a root pitch angle of 16° and for the straight twisted blade for a root pitch angle of 24.5° ; (b)-Aerodynamic efficiency at different Re numbers

A decrease in the FM is also noticed starting from the above-mentioned angles. This behavior is confirmed also in the case of the backward curved blades (which geometry has been presented in section 3.1), and it finds its roots in the aerodynamic efficiency curve for Re equal to $3.88 \cdot 10^4$, which is shown in figure 3.15-b, and it is compared with the case of Re equal to $1 \cdot 10^6$. It is clear how at higher root pitch angles the blade element operates in an interval of low aerodynamic efficiency. This fact causes also the absence of an improvement when inserting a twisting in the blade, since the root pitch angle should be increased to produce the same thrust as in the untwisted case, moving towards the poor efficiency region. In figure 3.16 the summary of these considerations is presented. From this analysis it seems that inserting a curvature may bring some benefits in term of FM, however these

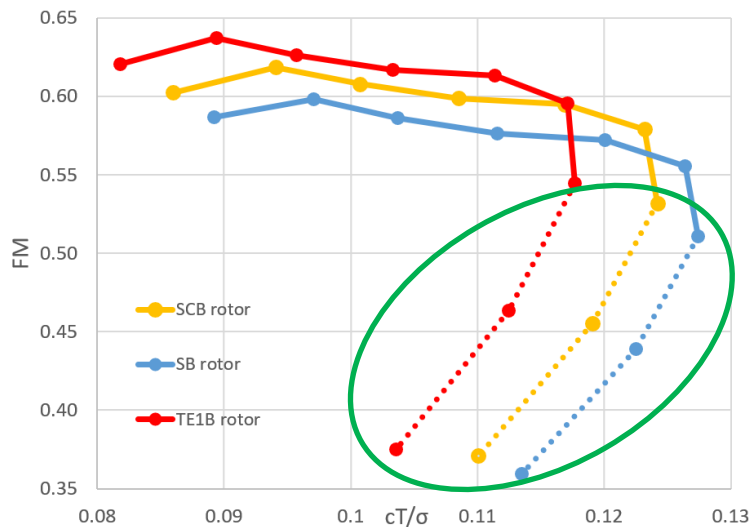


Figure 3.16: FM vs thrust coefficient/solidity calculated with the BEMT

results must be treated with caution, and verified. The values inside the green circle are the one for pitch angles of 16°, 17° and 18°, which present the above-mentioned characteristics.

3.5.4 Blade division in segments

To take the Re variation along the blade into consideration in order to improve the correctness of aerodynamic coefficients, a division of the blade in segments has been operated. For each segment, a mean value for Re is determined and applied to all blade elements englobed in respective part. Initially, the blade is divided in five segments, then in ten segments, with the Re values at each segment presented below:

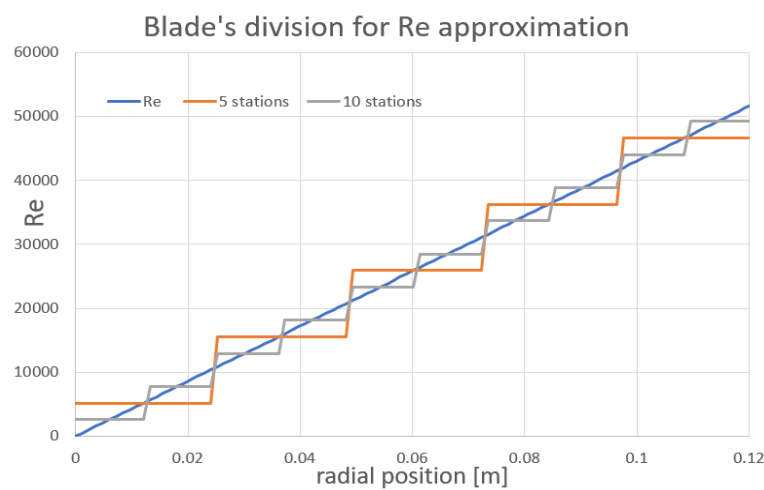


Figure 3.17: Re development along the blade in the case of five or ten divisions

At each blade segment, the usual procedure is applied for the determination of the polynomials characterizing the lift and drag developments in function of the angles of attack. With the five-segment division, five polynomials for the lift and for the drag are obtained, respectively. Then, in the Matlab

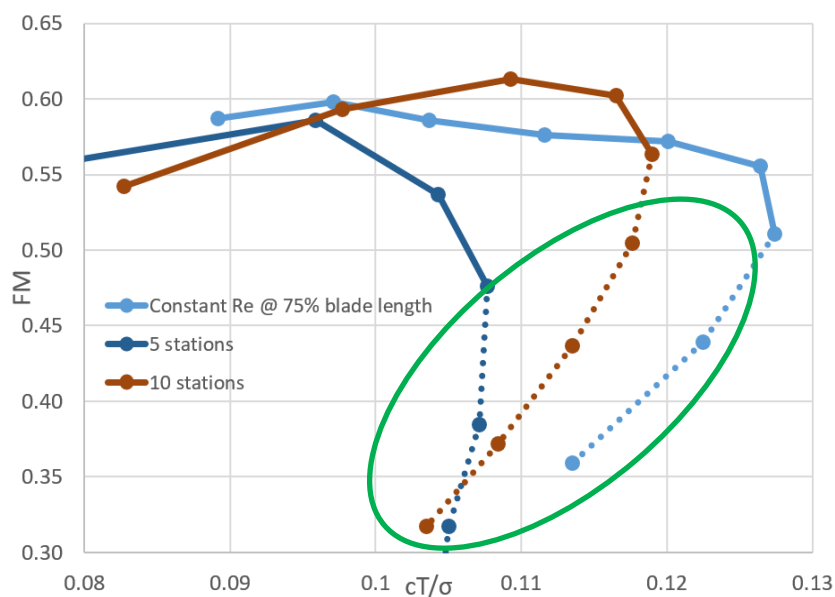


Figure 3.18: FM behavior evaluated with three different approaches for the low RE regime

routine, the proper polynomials are used, based on the position of the blade element. Also with the blade division in segments, the regression in the thrust production as the root pitch angle overpass a certain value is evident, for the same reasons previously mentioned (points inside the green circle). In the case of straight untwisted blade, the behavior is depicted in figure 3.18 for the SB rotor.

The BEMT method here developed is not enough accurate to describe the complex physics around propellers working on a low Re regime, so it cannot be stated that the insertion of curvature leads to an improvement in the FM. The reasons for such inaccuracies are the following: the first is the already said hypothesis in which the induced velocity field is calculated, that is the linear relationship between lift coefficient and angle of attack. This cannot be satisfied in this low Re regime, as previously shown. Trying to linearize the behavior would cause another question in determining the correct value of lift slope: different choices of lift slope would bring different induced velocity distributions, angles of attack, and finally aerodynamic characteristics. Moreover, non-considering the swirling velocity and the radial velocity component at each blade element may be a too strong simplification for the case in exam. Finally, the behavior of thrust reduction after a certain root pitch angle seems not physical, and it seems to be caused by the assumptions done.

At this point, there are two options for further procedure. The first option suggests trying to develop a modified BET without the need of assuming the value of $c_{L\alpha}$, and inserting the swirling velocity as well as the radial component. However, it is questionable how the complex 3D phenomena would be treated, especially in terms of how the nominally laminar boundary layer would be described with the insertion of these velocities. The alternative is the development of CFD analyses which require a significantly higher amount of computational time. On the other hand, their accuracy is higher. Moreover, by finding the fields of pressure acting on the blade, CFD represents a valid instrument to evaluate the best materials for an eventual 3D printing process, by imposing the pressure field acting on the rotor as a load in a structural analysis. Therefore, choosing the second option for further steps, the next chapter is going to cover the development of CFD models.

4 CFD simulations

The results deriving from the BEMT must be treated with caution, since this theory is essentially bidimensional and do not consider the velocity components orthogonal to the airfoil plane. As discussed in Chapter 3, the variability of the aerodynamic coefficients is causing uncertainty in the results for small scale rotors, along with the impossibility of considering the relation between the angle of attack and the lift coefficient as linear. For these reasons, a more accurate method for the analysis shall be used. By solving the Reynolds_Averaged Navier Stokes equations (RANS) in a domain built around the blade geometry, a CFD analysis may lead to more reliable results. Moreover, it gives the option of analyzing the field of pressure acting on the blade surface, thus understanding which structural loads are acting on it. The development of CFD in recent years made it a fundamental tool to be used in the process of designing parts that have interactions with the fluid dynamics. Nowadays, it is a widely used tool in aerospace applications. The CFD development is realized using the ANSYS package: in fact, the geometry is defined in DesignModeler, while the meshing procedure is defined in the ANSYS Mesher. The calculations are made in Fluent: this tool is one of the most used in the analyses of fluid-dynamics and it gives the possibility of checking different parameters during the simulation, permitting also an intuitive post processing [31].

At first, the fundamentals of CFD analysis are going to be introduced, followed by an insight into the modeling of rotational problems. Finally, the prepared model and the results of the CFD analysis are presented and discussed.

4.1 CFD RANS

All fluid phenomena are described by the Navier-Stokes differential equations which are the direct application of mass, momentum and energy conservation to fluids. If the initial conditions and the boundary conditions are known, the development of the system in time is well defined by these equations. However, experiments showed that small changes in the initial condition of a flow can lead to different solution in the development of the system. For example, the pictures of the same water cascade in figure 4.1 have been taken by using various exposure time. It is obvious that the pictures are similar if the exposure time is sufficiently high, while they are very different when reducing the exposure time. This means that instantaneous fields are chaotic and unsteady, they depend on space and time, and they are characterized by the presence of intense gradients. Averaged fields recover the steadiness of boundary conditions and recover symmetry conditions, so that a 2D analysis may be enough in the description of problems characterized by a symmetry. Engineers are often interested in the mean behavior of a flow, thus a statistical description of turbulence flows is going to be used in this work. The averaging of Navier-Stokes equations generates the RANS. To obtain those, the instantaneous velocity

is written as the sum of an averaged term (\bar{u}_i) and a fluctuating term (u_i'). In the following equations, $i = 1,2,3$ and $j = 1,2,3$ are indices used to refer to the three directions of a standard reference frame.

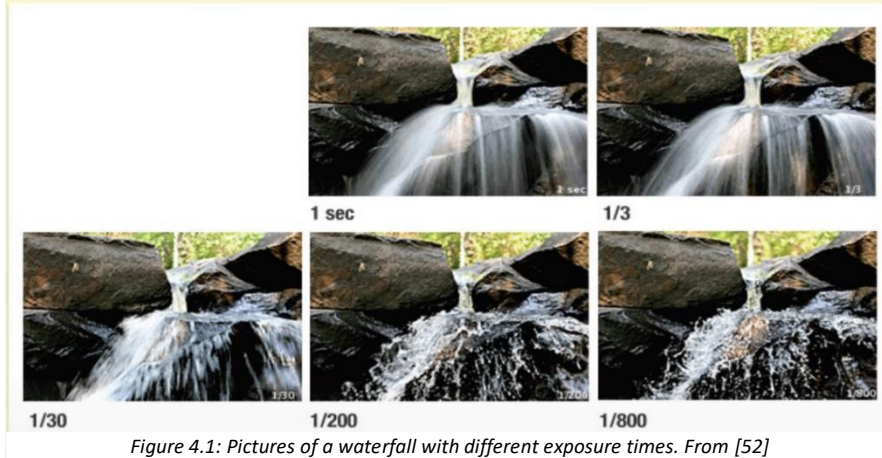


Figure 4.1: Pictures of a waterfall with different exposure times. From [52]

$$u_i = \bar{u}_i + u_i' \quad (4.1)$$

The application of the mean operator to each one of the N-S equations sets:

$$\frac{\partial \bar{u}_i}{\partial x_i} = 0 \quad (4.2)$$

$$\frac{\partial}{\partial t} \bar{u}_i + \bar{u}_j \frac{\partial \bar{u}_i}{\partial x_j} = -\frac{1}{\rho} \frac{\partial \bar{p}}{\partial x_i} + \frac{1}{\rho} \frac{\partial}{\partial x_i} (2\mu \bar{E}_{ij}) + \frac{\partial}{\partial x_i} \tau_{ij} \quad (4.3)$$

$$\tau_{ij} = -\overline{u_i' u_j'} \quad , \quad \bar{E}_{ij} = \frac{1}{2} \left(\frac{\partial}{\partial x_j} \bar{u}_i + \frac{\partial}{\partial x_i} \bar{u}_j \right) \quad (4.4)$$

\bar{p} represents the averaged pressure value, μ the fluid viscosity, and \bar{E}_{ij} represents the strain rate tensor, which represents how the averaged velocity changes at different points of the fluid domain, while τ_{ij} states the unknown Reynolds stress tensor that depends on the fluctuating velocity. This tensor is formally the only difference between an instantaneous and an averaged velocity field, so its determination is of high importance. Since it is a symmetric tensor, the unknown components are only six, which added to the three components of velocity and the pressure gives a total amount of ten unknowns in four equations, namely the continuity and the three momentum equations.

4.2 Turbulence models

Bardina & others [32] presented a description of the most used turbulence models available for various applications underlining strength and weaknesses; among the various possibilities, after the study of the literature available for the CFD study of rotating problems (see Chapter 1), the $k - \omega$ SST model is chosen for this work. Menter [33] developed this turbulence model to merge the positive aspects of

$k - \epsilon$ and $k - \omega$, with the latter used to describe the near walls region, and the first to study the outer part of the boundary layer. By inserting a blending function F_1 with gradually changing values from 0 to 1, it is possible to change the model based on the position of the calculation point with respect to the wall. Moreover, this function influences the value of the model constants to permit their modification. The value of F_1 changes in every cell of the domain, and the use of the hyperbolic tangent in its definition permits a smooth transition. A more detailed description of the model can be found in [34].

4.3 Solving the boundary layer

When using CFD, it is significant to find a way of representation of the behavior of velocity near the walls of objects inserted in the fluid domain. In the boundary layer region, very high velocity gradients are present, to bring the velocity from 0, on the surface, up to the undisturbed value. Basically, two approaches are possible. Their distinction can be understood better by introducing the parameter y^+ :

$$y^+ = \frac{yu_T}{\nu} \quad (4.5)$$

where $u_T = \sqrt{\frac{\tau_W}{\rho}}$ represents the viscous velocity, ratio between the shear stress due to viscous effects τ_W and the density of the fluid ρ ; y is the real distance between the point of measurement and the wall, whereas ν is the cinematic viscosity. y^+ can be thought of as a sort of turbulence Re number as it represents the ratio between the Reynolds and viscous stresses: low values of this parameter characterize the viscous part of the boundary layer where the velocity increases with the law:

$$u^+ = y^+, \text{ where } u^+ = \frac{u}{u_T} \quad (4.6)$$

Here, u^+ represents the dimensionless velocity, ratio between the actual velocity parallel to the wall u and the friction velocity $u_T = \sqrt{\frac{\tau_W}{\rho}}$.

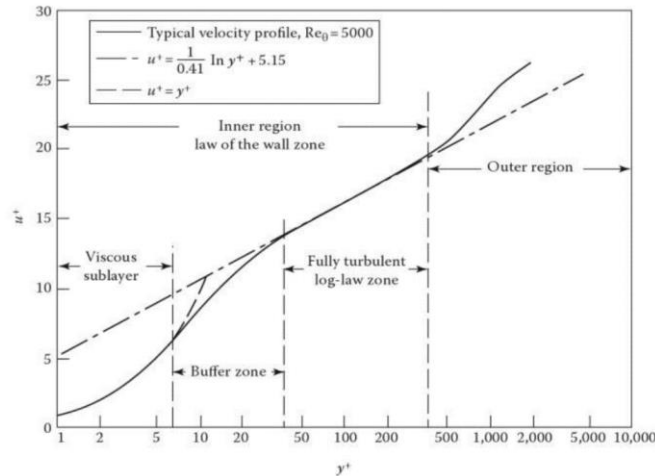


Figure 4.2: Velocity profile inside a turbulent boundary layer. From [51]

On the other hand, when y^+ reaches high values, the viscous effects are low, and the turbulence is mainly responsible for the velocity decreasing: the point is in the fully turbulent region. Therefore, the velocity increases logarithmically in this region, according to the law $u^+ = \frac{\ln(y^+)}{0.41} + 5.15$ (see figure 4.2). The first approach aims to completely resolve the boundary layer, meaning that the value of y^+ for the first cell near the wall should equal approximately 1. A correlation between the value of y^+ and the first cell dimension can be obtained by using a formulation derived from the Blasius theory for the flat plate:

$$y^{1st\ cell} = \frac{y^+ \nu}{\sqrt{\frac{v_\infty^2 0.0576 Re_x^{-0.2}}{2}}} \quad (4.7)$$

Re_x represents the local chord Re number, v_∞ the velocity investing the plate and ν the cinematic viscosity.

This approach is reliable when used with a low Re turbulence model (especially $k - \omega$), and it is suggested when the aim is to determine the forces acting on walls, like aerodynamic drag or blade

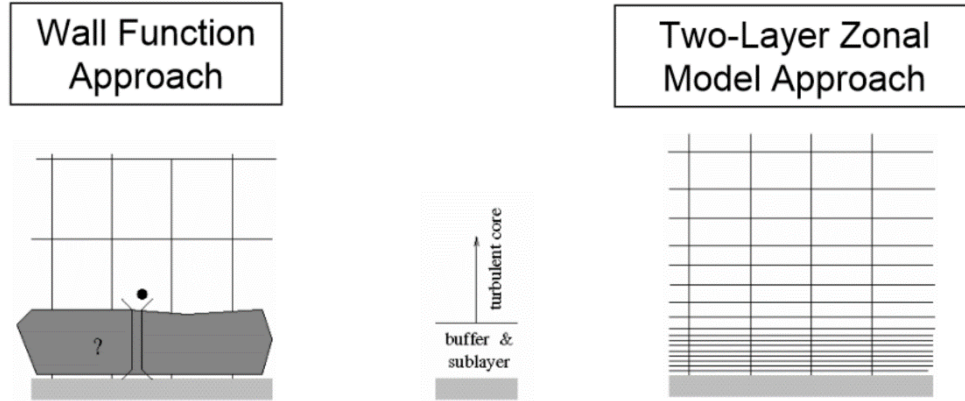


Figure 4.3: Different approaches for boundary layer description. From [51]

general performances. The counterpart is an extremely high computational cost, due to the small element dimensions near the surfaces. The second approach is the use of wall functions. The near-wall region is modeled with empirically derived functions. This strategy relies on the fact that the velocity profile near the wall is similar for almost all turbulent flows. The first cell center needs to be placed in the log-law region which conclusively leads to an interval in which the parameter y^+ can stay: $30 < y^+ < 300$. If its value is lower than 30, the model is invalid while the wall may not be properly resolved if it's higher than 300. With this approach, the usage of high Re turbulence models like $k - \epsilon$ is recommended. The computational demand in this case is lower and results in faster simulations.

If the wall functions are used, phenomena like separation of the fluid or transition laminar to turbulent regime are hard to capture. Moreover, especially for complex geometries, the requirement of keeping y^+ within the recommended interval could be very hard if not impossible to satisfy. It is therefore recommended to use the $k - \omega$ SST turbulence model since it allows to automatically blend the transition between viscous sublayer and logarithmic layer used based on the position of the calculation cell center with respect to the nearest wall [34].

4.4 Flow around rotating objects

There are different ways to model the rotation of a body inside a fluid domain, each with its own peculiarities. One of them is the Moving Reference Frame method (MRF) that introduces a rotation in the frame of reference of a selected domain zone in order to render the problem steady and easier to solve [31]. The alternative is putting the entire mesh in rotation. This approach is being referred to as Moving Mesh method: it gives the option to capture the unsteady characteristics of the flow. In the following paragraphs a description of the two methods is given, along with some useful tips for their implementation.

4.4.1 Moving reference frame

Among the different methods that are available for the description of problems including rotation and generally moving objects inside the flow field, this method has the lowest requirements regarding computational effort due to several simplifying assumptions. However, its theoretical development is precise and based on the concept of expressing the equations with respect to a moving reference frame in some domain regions. In fact, considering the current case, it is possible to divide the fluid domain in two zones: one that encloses the rotor, named *moving zone*, and the rest of the domain, the *fixed zone*. In the moving domain, RANS equations will be solved with respect to a frame that is rotating with the angular velocity of the rotor. That way, the unsteady rotating physics in the near surrounding of the rotor can be treated as steady. In the fixed domain, the equations will be solved in the usual reference frame. The link between the velocities obtained in the two zones is due to a change of coordinates. Since the interaction between domain zones is not taken into account this method can also be referred to as the “Frozen Rotor Method”.

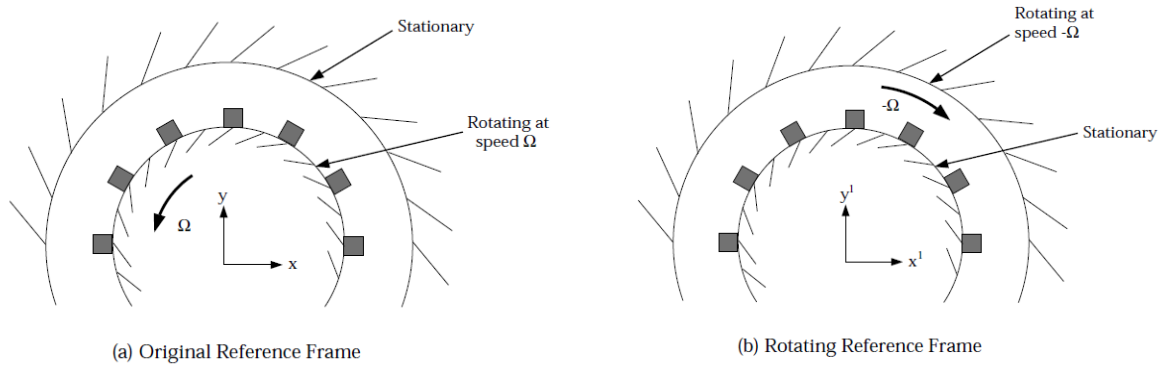


Figure 4.4: Moving Reference Frame method. From [31]

Fluent allows to solve the equation either in the usual reference or rotating frame, for the absolute value of the velocities or for the relative value. A general rule suggested by Fluent developers is to use the absolute formulation if the greater part of the domain is fixed, otherwise applying the relative formulation [34]. However, it must be said that if the coupled solver is activated (see dedicated paragraph) the only available formulation is absolute. It is important to know the presence of some restrictions:

- Any wall inside the rotating domain can appear in any shape.
- The interface between moving and fixed domain must be a surface of revolution.
- The outer wall of the fixed domain must be a surface of revolution.
- The problem is treated as steady even if it is not. Therefore, it is not taken into account the fact that the air encountering a blade is disturbed by the passage of the previous blade(s).

The two zones can have non-conformal meshes at the interface. Fluent will automatically manage the relationships between the near cells in order to determine the fluxes at the interface. In fact, at the boundary between two cell zones the diffusion (and other terms which are present in the equations describing the flow behavior in one subdomain) requires values of the velocity from the other subdomain. The program imposes the continuity of the absolute velocity in order to provide the exchange of information between the two zones. If the relative formulation is used velocities and velocity gradients must be converted to their expression in the absolute inertial frame, using the following equations:

$$\vec{v}_{abs} = \vec{v}_{rel} + (\vec{\Omega} \times \vec{r}_p) + \vec{v}_{trasl} \quad (4.8)$$

$$\nabla \vec{v}_{abs} = \nabla \vec{v}_{rel} + \nabla (\vec{\Omega} \times \vec{r}_p) \quad (4.9)$$

$\vec{\Omega}$ represents the angular velocity of the moving frame, \vec{r}_p the position vector of the calculation point, expressed in the moving frame, \vec{v}_{abs} is the absolute velocity \vec{v}_{rel} is the relative velocity and \vec{v}_{trasl} the translational velocity of the moving frame. If the absolute formulation is used, there is no need for transformations of the coordinates as the velocities are stored in their absolute formulation.

4.4.2 Equation for a rotating reference frame

The Navier-Stokes equations in the moving domain must be re-written to take the additional terms in the acceleration of the fluid into account [34]. As previously stated, Fluent permits the user to choose between the relative and absolute formulation, with the two velocities being related by the following equation:

$$\vec{v}_{rel} = \vec{v}_{abs} - \vec{\Omega} \times \vec{r}_p \quad (4.10)$$

The left-hand side of the equation for conservation of mass can be written (both for relative and absolute formulation) as:

$$\frac{\partial}{\partial t} \rho + \vec{\nabla} \cdot (\rho \vec{v}_{rel}) \quad (4.11)$$

The left-hand side of the momentum equations assumes the following shapes, equation (4.12) for the absolute formulation and equation (4.13) in case of relative formulation:

$$\frac{\partial}{\partial t} \rho \vec{v}_{abs} + \vec{\nabla} \cdot (\rho \vec{v}_{rel} \vec{v}_{abs}) + \rho (\vec{\Omega} \times \vec{r}_p) \quad (4.12)$$

$$\frac{\partial}{\partial t} \rho \vec{v}_{rel} + \vec{\nabla} \cdot (\rho \vec{v}_{rel} \vec{v}_{rel}) + \rho (2\vec{\Omega} \times \vec{v}_{rel} + \vec{\Omega} \times (\vec{\Omega} \times \vec{r}_p)) + \rho \frac{\partial}{\partial t} \vec{\Omega} \times \vec{r}_p \quad (4.13)$$

In equation (4.13), the term $\rho(2\vec{\Omega} \times \vec{v}_{rel} + \vec{\Omega} \times (\vec{\Omega} \times \vec{r}_p))$ represents the Coriolis force. Fluent does not consider the term $\rho \frac{\partial}{\partial t} \vec{\Omega} \times \vec{r}_p$, so this approach therefore is not reliable for cases in which the angular velocities are varying in time. However, in the following analysis the rotational velocity is kept constant, so that this limitation is not hindering the results.

Solving the equations written in this way lead to the determination of the flow characteristics in the computational domain. Most of the boundary conditions are similar to those of a generic CFD analysis. The only particular condition regards walls that have a certain velocity with respect to the rotating domain. In particular, a zero rotational velocity (in the moving frame) must be assigned to the rotor walls to replicate that the rotor is moving with the same angular velocity as the frame.

The coupling between momentum equations is usually high when solving flows characterized by rotations, moreover a large regime of rotation introduces pressure gradients that tend to drive the flow in the axial and radial directions, inserting a distribution of swirl in the field. These facts may lead to instabilities, so some general rules should be followed to enhance the quality of the simulation [34].

- The use of PRESTO (Pressure Based Segregated Solver Only) scheme is highly recommended as it properly describes the pressure gradients which involve rotating flows.
- Reduce the under-relaxation factors for the velocity up to 0.3, 0.5 or lower.
- Begin the simulation with a low rotational speed and increase it gradually until reaching the desired speed.

MRF is not a transient analysis, thus the results should always be compared to a detailed CFD analysis or experimental data. However, its low computational cost makes it one of the best tools for approaching the computational analysis of rotating systems. MRF approach can be also used as starting point for successive transient analysis, which quality is very sensitive to the initial conditions.

4.4.3 Moving mesh method

If an accurate time dependent solution is required, the Moving Mesh method instead of the averaged results coming from an MRF analysis finds its use. It is the most accurate method for simulating flows in which parts of the fluid domain are moving, and it is also the one with higher computational cost. The fluid domain is divided in at least two zones which are separated by an interface: the relative motion between these zones will take place along the interface. With this method, the motion of a part of the domain is not considered imposing a velocity to the frame of reference. Instead, it is the mesh of the moving domain that changes position with respect to the fixed domain: the relative sliding between cell zones is realized in discrete steps, and the non-conformal interfaces will be updated automatically by

Fluent. Thus, the node alignment is not required here. As for the MRF, the mesh interfaces must be based on the same geometry, and they must be created so that there is no motion normal to them.

The setup resembles the one for MRF approach, however, the transient calculation must be enabled. After initializing the solution, the time step size and the number of time steps must be defined: a proper value for the time step and for the number of time steps are to be set in order to simulate a valid amount of mesh positions. With a fixed relative position between cell zones, Fluent will iterate to solve the RANS equations until reaching convergence or the maximum number of iterations. The software will then apply the geometric transformation to obtain the new configuration of the fluid domain and update the interfaces, preparing the domain for the next iterative process.

As said before, a good suggestion for initializing the solution in case of the Moving Mesh method is to start from a previous simple MRF analysis of the same case, which could cause a faster rate of convergence for the simulation. The transient nature of this method gives the opportunity to simulate the actual flow field that a blade is encountering in time, but it must be noted that the computational demand is higher. Another positive aspect of this method is the possibility of viewing the development of the fluid flow in time and thereby checking if the assumptions made for the boundary conditions are correct. The mathematical formulation of this approach is presented in Ansys Fluent Theory Guide [34]. In this study, the MRF method is used because the analysis of many different configurations is required. That makes a transient approach for their study with the provided machine not realizable. The characteristics for the machine are listed in the table below.

Table 2: Computer characteristics

	Dell Inspiron 5579
Processor	Intel Core i7-8550U CPU @1.80 GHz
RAM memory installed	16 GB (15.8 GB available)

A possible future development would therefore be the analysis of the cases with the Moving Mesh method in order to define the amount of error committed when treating the phenomenon of hovering as steady.

4.5 Geometrical model

The rotor was modeled in Solidworks while its import inside a moving and a fixed domain is realized in Ansys DesignModeler. Further, the NACA 0012 is used as the blade profile. It is one of the most studied airfoils and therefore reports a high availability of experimental datasheets of its behavior at low Re regime. All the geometrical dimensions are chosen based on the thesis purpose of using 3D printing technologies to print the rotors, and eventually testing them in a test bench available at the University facility. The nominal chord length is set to $c = 20 \text{ mm}$. The trailing edge (TE) presents a width of 0.3 mm

in order to improve the element quality: meshing a zone in which two faces converge to a single line would for CFD simulations lead to poor quality meshes, affect results and hinder a converged solution. The presence of a finite-width TE improves the element skewness in the surrounding of the TE which was close to one (worst value) before the operation. The blades are then created with an extrusion along a curve which can change shape in order to generate different curvatures. The hub is modeled as a cylinder having an external radius of 15 mm and a height that depends on the pitching angle, varying from 10 mm to 12 mm, while the internal hole diameter results in 5 mm to ensure the coupling between the rotor and the motor shaft. The cylinder and the two blades are linked by a fillet. For a comparison later on, the radial dimension for each model is maintained fixed to 120.44 mm, in order to have rotors with the same disk area.

Four different rotor planforms were studied: the straight blade rotor, the single curved blade rotor, the total curved blade TE1 rotor and the total curved blade TE2 rotor. The geometrical characteristics are the same presented in section 3.1 for the analysis with the BEMT. The single curved blade has the starting curvature point at 70 % of the distance from the axis of rotation, the path being a circumference with a radius equal to 57.15 mm. The only difference between the other two curved blades is the tip shape, since their curvature path is equal.

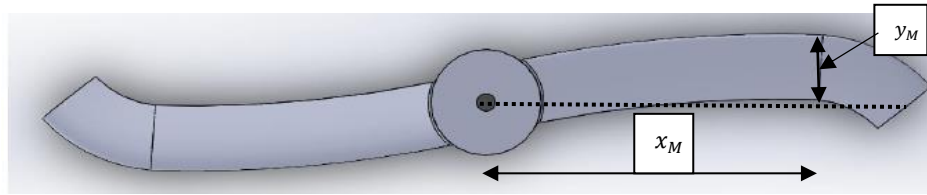
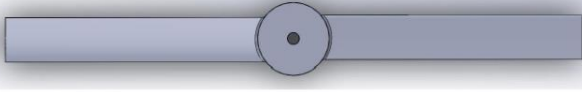
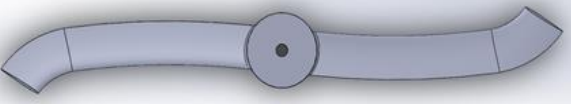
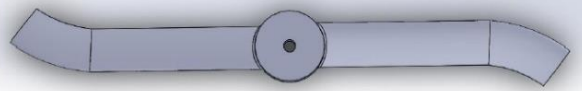
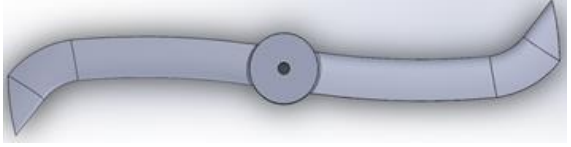
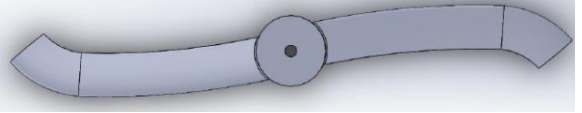
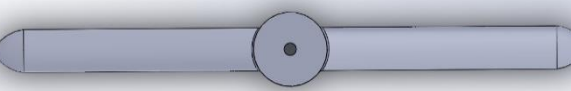
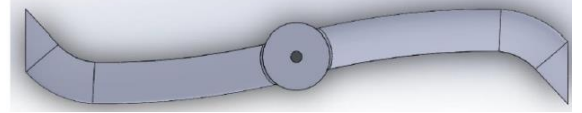
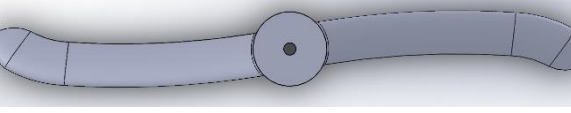
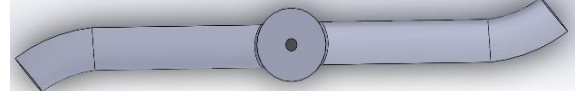
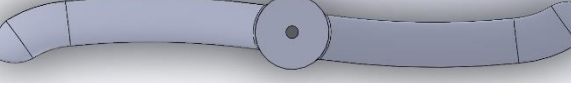


Figure 4.5: Total curved TE1 rotor, with location of the maximum point

This path is the sum of two circumferences, the inner circumference having a radius of 315.8 mm, and the outer one having a radius equal to 33.84 mm. The merging point is located at $x_M = 75\%$ of blade length, and $y_M = 10\%$ of blade length. While TE1 presents a tip which follows the curvature of the blade mean-line staying perpendicular to it, TE2 presents an additive part to ensure that the final blade section is parallel to the airflow. The models are created with different values of blade pitch angle, in order to vary the thrust production, and both with and without twisting rate, keeping it equal to $10^\circ/m$. The tapering is not considered. Even though the insertion of tapering may lead to an improvement in the rotor performances, it is decided not to add another parameter in the analysis in order to keep the focus on the curvature effect. Three reversed curved blades are developed, keeping the same curvature parameters but inverting its direction. That way, it is possible to study whether or not a forward or backward curvature guarantees better performances at low Re regime. Finally, the same tip shape is applied to the straight blade, the single curved blade and the total curved blade in order to limit the tip effects, isolating the effect brought by the curvature. Table 3 resumes the blade modeled, and it gives a name to each rotor.

Table 3: Rotor prototypes and nomenclature

<p>Straight blade SB</p> 	<p>Total curved forward TE1 blade TE1F</p> 
<p>Single curved backward blade SCB</p> 	<p>Total curved forward TE2 blade TE2F</p> 
<p>Total curved backward TE1 blade TE1B</p> 	<p>Straight blade tip modified SB3</p> 
<p>Total curved backward TE2 blade TE2B</p> 	<p>Total curved backward blade TE3B</p> 
<p>Single curved forward blade SCF</p> 	<p>Total curved forward blade TE3F</p> 

In each case, the model prepared in Solidworks is saved with the .igs extension to ensure its readability for Ansys DesignModeler. The command *enclosure* is used to create the moving and fixed domains: for both cases, a cylindrical shape is chosen, imposing the distances above, below, and radial from the

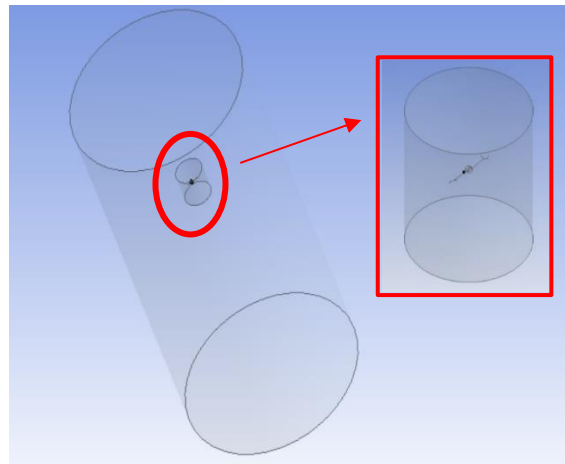


Figure 4.6: Examples of fixed and moving domains

inner object. For the first enclosure, representing the moving domain, the object considered is the rotor, while for the second enclosure, the interior object considered to define the dimensions is the moving domain.

The overall computational domain is a cylinder with 7.06 m height and 3.54 m diameter (see figure 4.6). These dimensions permitted to put the outer boundaries far from the rotor to avoid any kind of interference. A sensitivity analysis is realized to visualize how variations on the moving domain dimensions might affect the simulations. The results will be presented and discussed in paragraph 4.8 of the current chapter. After defining the enclosure, an operation of boolean subtraction is actuated in order to separate the two domains, thus creating the interface zone between them. This step is of great importance when defining a problem to be solved by using the MRF method. Another very important operation is the setting up of a new coordinate system which has its center in the center of the rotor (see figure 4.7). That way, it is easier to impose the rotation of the body, and therefore to calculate the forces and the torques in the post processing phase.

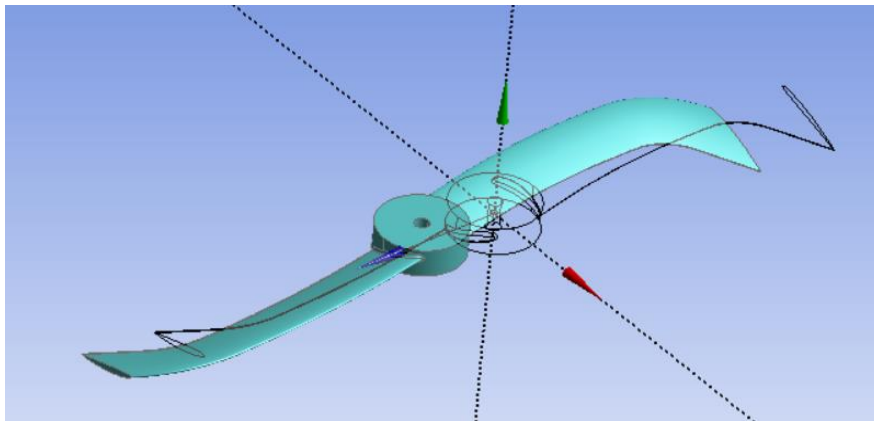


Figure 4.7: Translation of the body at the origin of the new frame of reference. The "old" position is in green, while the transparent rotor represents the new position

4.6 Mesh

Before starting the meshing procedure, the contact zone between the two domains is checked, ensuring that the contact is between the three internal faces of the fixed domain and the three external faces of the moving domain. The meshing procedure is one of the most important steps in the CFD analysis. The domain must be divided in a discrete number of elements, at which location the equations will be solved. An accurate and efficient meshing can increase the rate of convergence and can well-capture phenomena of high gradients for certain quantities. A standard procedure for the fluid domain meshing do not exist: having a certain physic domain, there are regions in which a fine mesh is required, and other in which it is not useful to have a great number of elements, since the behavior of the fluid is almost stable.

4.6.1 Mesh topology

For the mesh topology two options are available: a structured mesh or an unstructured mesh. In a structured mesh, the fluid domain is divided in blocks, which are singularly meshed with hexahedral elements. This approach produces the highest quality meshes, thus optimizing the computational time and the memory needed by the calculator. The drawback of this topology is the high time demand in the mesh production: generating a structured mesh could be very time consuming, and it could become prohibitive in the case of complex geometry. Examples of structured meshes used to study the flow around small-scale rotors are present in the work of Subhas [21]. The progress made in the definition of unstructured meshes in the last few years made them a very appreciated tool in the industry field. In fact, the procedure of meshing is semi-automatic, and bodies of whatever shape can be meshed in a relatively short period. Most of unstructured meshes are realized with tetrahedral (or polyhedral) elements. The tetrahedral elements are not good for the boundary layers meshing, since they cannot be stretched too much: this would in fact, lower their quality; for this reason, very often some prism layers are used in the surrounding of walls, to create the inflation sheets. Generally, a higher number of tetrahedral elements is required to mesh these regions with respect to hexahedral elements. The need of testing many different rotor configurations, the study of previous works done in small-scale rotors meshing (see references [19], [22]) and the fact that the tetrahedral unstructured meshing is the most used procedure in the Ansys ambient, led to choose the unstructured topology for the current work.

4.6.2 Mesh quality

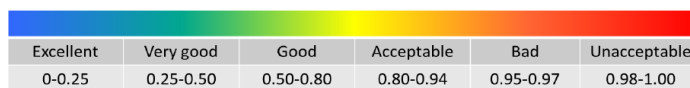
Another very important aspect is the mesh quality, since the accuracy of results can deteriorate as the elements shape gets distorted from the ideal one. In this sense, many parameters can be checked to ensure a good mesh quality, two of them are the skewness and the aspect ratio AR. Two methods are available for the skewness definition. In the case of triangles or tetrahedrons the skewness may be expressed as the equilateral volume deviation (equation 4.14), while the definition through the normalized angle deviation can be used for whatever element (equation 4.15):

$$SKEW_{tetra} = \frac{V_{optimal\ cell} - V_{cell}}{V_{optimal\ cell}} \quad (4.14)$$

$$SKEW_{hexa,tetra} = \max\left\{\frac{\theta_{max} - \theta_e}{\theta_e}; \frac{\theta_{min} - \theta_e}{\theta_e}\right\}, \quad (4.15)$$

where $\theta_e = 60^\circ$ for tetra, $\theta_e = 90^\circ$ for hexa

Ideally, the best value of skewness is 0, while the worst elements have a skewness equal to 1.



Excellent	Very good	Good	Acceptable	Bad	Unacceptable
0-0.25	0.25-0.50	0.50-0.80	0.80-0.94	0.95-0.97	0.98-1.00

Figure 4.8: skewness scale

The AR has two different definitions, depending on the element dimension (see equations 4.16 and 4.17).

$$AR_{2D} = \frac{length}{height} \quad (4.16)$$

$$AR_{3D} = \text{area ratio} , \text{ or } \frac{radius \text{ circumscribed circle}}{radius \text{ inscribed circle}} \quad (4.17)$$

The AR best values are near one, while the element quality decreases as this value increases. The only elements for which a high AR is tolerated are the ones located in regions in which there is no strong transverse gradient, such as the boundary layers. It is possible to define some limit values to be respected in order to satisfy the quality requirements of a mesh: the maximum skewness value should be always lower than 0.90, while for the AR the limit is 40 (or 50 in the case of boundary layer) [31].

In the Ansys Mesher it is possible to check the mesh quality distribution and the mesh metrics. In fact, a parameter (Skewness, AR, element quality) can be selected and a diagram bar will be displayed, showing the statistical distribution of the mesh elements with respect to that parameter.

This tool is very useful to locate the position of poor-quality elements, thus helping the user to understand the regions in which a mesh improvement is needed. In figure 4.9 the distribution of AR for a mesh of the TE1B rotor is presented. The tetrahedral elements are colored in red, while the prism elements are colored in green. It can be noted that the higher AR value is around 10.80, well below the limit value of 40: this indicates that the mesh is enough accurate to be used for a simulation. In general, in all the mesh prepared, the AR is always kept below the value of 15, and the maximum skewness value is always below 0.85.

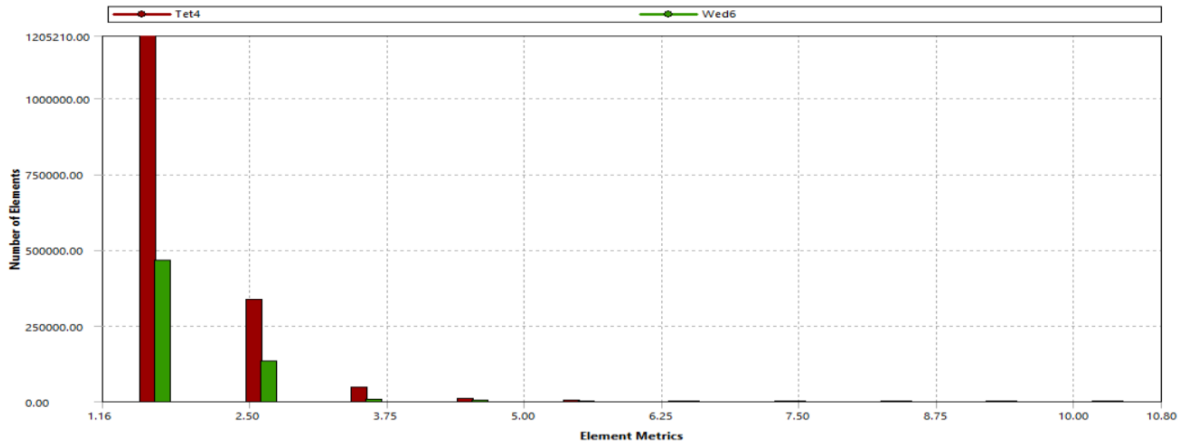


Figure 4.9: Mesh metrics of the AR parameter, for the total curved blade TE1

4.6.3 Mesh method, sizing and inflation

Since the geometry of the model is quite simple the patch conforming method is preferred to the patch independent method. The first is suggested when there is the need of high accuracy at the surfaces, because it has a bottom-up approach: in fact, the first entities to be meshed are the edges, followed by the faces and then by the volumes. Instead, in the patch independent method, the volumes are meshed first, followed by faces and edges: 2D and 1D entities are not necessarily respected during the mesh procedure. If small details are present in the model's geometry, then the patch conforming method has to be chosen [31].

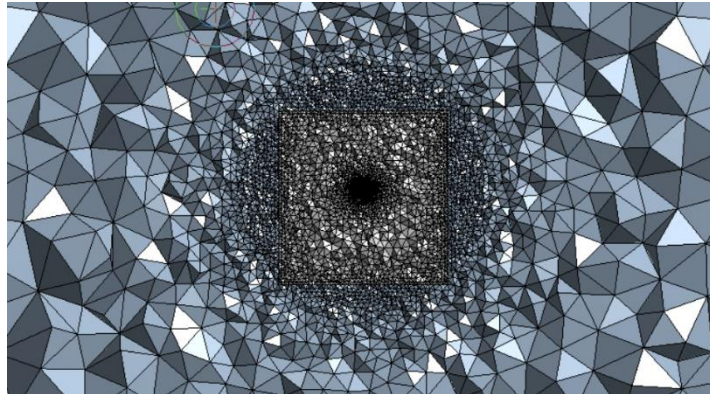


Figure 4.10: Sphere of influence method, for the meshing of fixed domain. The moving domain is depicted in grey

The sizing of the two domains is realized in different ways. The fixed domain is sized with a sphere of influence approach: the sphere center, radius as well as the minimum element size desired must be defined. In this way, it is possible to refine the mesh quality near the interface between the fixed and the moving domain, without increasing too much the number of elements, since their dimension is increased when getting farther from the interface.

For the meshing of the moving domain, it is decided to focus on the faces: the faces of the moving interface are meshed defining the element size and imposing the respect of curvature, with a normal curvature angle of 12° . This angle represents the maximum allowable angle that an element's edge could span: in this way, a finer mesh in the lateral surface of the cylinder is created, with a transition of the cell size regulated by the value of growth rate (the default is 1.2). The rotor surfaces are meshed defining the element size and imposing the respect of proximity and curvature: this permits a high-quality mesh in the surrounding of the blades, as well as a good description of the leading edge, which is characterized by a small radius of curvature.

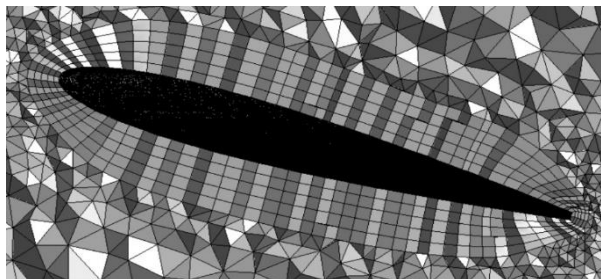


Figure 4.11: Inflation near the rotor. Notice how the element dimensions changed with the surfaces curvature

The insertion of inflation in the moving domain is needed, to capture the behavior near the rotor. Different ways are available to define its characteristics:

- *smooth transition*, by which the program determines the local initial height checking the tetrahedra local dimensions, in order to achieve a smooth transition. In particular, the first layer height is calculated with:

$$1st\ layer\ height = \frac{H}{g^{n_{layers}-1}} \quad (4.18)$$

where H is the height of the last prism (equal to $H = average\ edge\ length * transition\ ratio$), g is the growth rate, and n_{layers} is the number of inflation's layers.

- *total thickness*, the program creates a constant layer height inflation, using the values of number of layers and growth rate (specified by the user) to obtain a total thickness
- *first layer thickness*, a constant inflation layers sheet is created, using the values of 1st layer height, maximum number of layers, and growth rate to determine the total height of the sheet.

This last option is chosen in this work. Moreover, the pre- inflation algorithm is selected: at first the surfaces of the mesh are inflated, and then the volume is meshed. The first layer thickness is determined knowing the Re number at the 75% of the blade radius and aiming to use a wall function approach for the description of the boundary layer (see section 4.3). The first layer thickness is found to be equal to 0.4 mm, for having a y^+ of about 50. This approach has been used for each mesh prepared. The mesh refinement needed for the sensitivity analysis, is realized by changing the minimum elements dimensions in the sizing.

4.7 Setup

In this section, the choices made in the setting up of the simulations are shown and explained, from the solution parameters, to the boundary conditions, going through the selection of the proper initialization method. ANSYS Fluent 18.1 is the program chosen to operate the CFD simulations. Due to the computational requirement in term of time and memory, the MRF is the approach preferred.

4.7.1 Solver and solution controls

Two kinds of solver are available in Fluent: the pressure-based solver and the density-based solver [34]. A control-volume approach characterizes both cases, but different ways of expressing and solving the system of equations are used in each method. If the pressure-based solver is chosen, two possibilities are then available: the segregated solution, in which the momentum equations are solved along the three axis, the continuity equation is calculated, and then the velocity is updated; and the coupled solver,

in which mass & momentum equations are rewritten in a coupled manner, and are simultaneously solved. After these different steps, the energy equation (if needed) is solved, and then the turbulence equations are solved. In most of the studies found in literature, the pressure-based solver was used [20], [35], [23]. In the case of density-based solvers, continuity, momentum and energy (if needed) equations are coupled and solved together, and after the programs solve the turbulence equations.

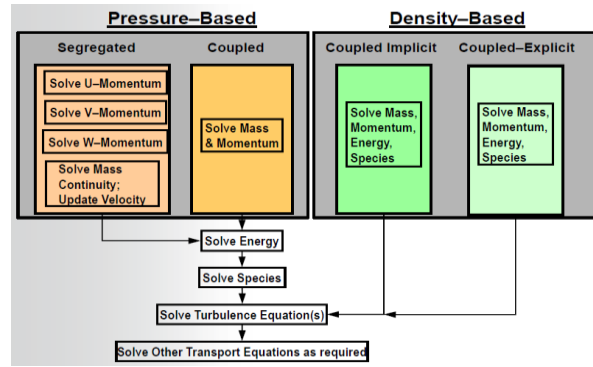


Figure 4.12: Types of solver available in Ansys. From [50]

The ANSYS Fluent Theory Guide [34] suggests the use of the pressure-based solver, since it is applicable for a wide range of flow regimes, from low speed incompressible flows to high speed compressible. Moreover, it suggests the use of the coupled solver, if there are difficulties in the convergence with the segregated: this choice can speed up the rate of convergence up to 5 times, while requiring a small amount more of memory during the calculation (1.5-2 times the memory of the segregated solver). At the same time, the reduction of the under-relaxation factors from 0.75 to 0.4-0.5 is suggested, when using the coupled solver, because this fact could avoid the phenomenon of oscillatory convergence. The under-relaxation factors are used to stabilize the convergence, and their value will not influence the final converged solution. Only the experience could lead to the setting of the proper under-relaxation factors for the case of study. Consider the generic variation after iteration of a quantity ζ' :

$$\zeta'_{i+1} = \zeta'_i + \eta \Delta \zeta' \quad (4.19)$$

η is the under-relaxation factor and ζ' represents a generic quantity to be determined by iteration.

Cases	Courant number-based coupled (iterations)	Pseudo-transient coupled (iterations)
Backward facing step (turbulent: SST)	750	75
Film cooling benchmark (turbulent: SA)	2,300	1,350
Flat plate, SST transition model	1,200	100
Rotor/stator with mixing plane model	500	250
Centrifugal pump	220	50
Axial compressor stage	400	110

Figure 4.13: rate of convergence achievements when using pseudo-transient approach. Image from [36]

In the Fluent *Solution Control* section, two different options to improve the convergence can be selected. The first is the Courant number (default value of 200): for more complex physics, a reduction of this value is recommended (up to 10-50). The alternative is to activate the pseudo-transient formulation [36]. In the case of stationary simulations, it is possible to insert an under-relaxation factor which value depends on a pseudo-time step size. If the automatic procedure is activated (recommended), Fluent

calculates automatically the value of the time step inside the domain and uses this value to obtain the stabilizing factors. Enabling the pseudo-transient option could improve the rate of convergence especially in the case of meshes with high AR. This approach is particularly suggested in the case of MRF, as shown in the picture 4.13.

4.7.2 Spatial discretization

Another very important aspect for the quality of the solution obtainable is the definition of the spatial discretization. In fact, the field variables are stored at the center of a generic cell, but they must be interpolated to the faces of the control volume, for spreading the solution in the entire fluid domain. Defining a generic property ζ' , the influence of the interpolating term can be seen looking at the following equation:

$$V_{cell} \frac{\partial \rho \zeta'}{\partial t} + \sum_{n^o \text{ faces}} \rho v \zeta' A_i = S V_{cell} + \sum_{n^o \text{ faces}} \Gamma \nabla(\zeta'_i) A_i \quad (4.20)$$

In which V_{cell} is the cell volume, Γ is the diffusion coefficient and S is the source of ζ' per unit volume. This value of ζ' is obtainable by interpolation. Different interpolation's schemes are available:

- First order upwind, it is the easiest to reach convergence, and it has a 1st order accuracy
- Power law, it has a greater accuracy than the first order, especially for flows at low Re
- Second order upwind, its use is essential with a tetrahedral mesh or when the flux is not aligned with the grid. The rate of convergence is usually lower, but it guarantees a 2nd degree accuracy.
- Monotone upstream centered schemes for conservation laws (MUSCL), it is a 3rd degree discretization order, available for unstructured meshes. It is good for the prediction of vortices
- Quadratic upwind interpolation (QUICK), it is a 3rd order scheme for hexahedral meshes. Its use is suggested for rotational flows.

To understand the way in which these different interpolation schemes work, consider the figure 4.14. If the first order upwind scheme is chosen, $\beta'' = 0$. This means that the value of the generic property in the face is the same as in the center of the cell. This method is robust, but not accurate. It is used for initial runs. The use of the second order upwind method leads to $\beta'' = 1$. This means that there is a linear variation of the generic property inside the element. It is necessary to add limitations to the value of ζ'_{face} to ensure a bound solution ($\zeta'_{c0} < \zeta'_f < \zeta'_{c1}$). The use of QUICK maximizes the value of β'' inside the domain, maintaining confined the value of ζ'_{face} reached. For the diffusive term of the previous

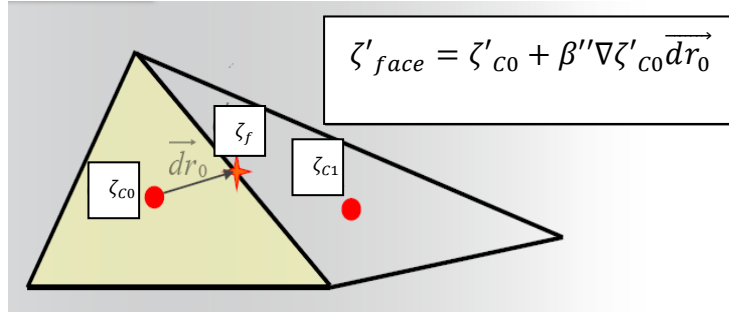


Figure 4.14: discretization schemes. Image from [50]

equation $(\sum_{n^{\circ} faces} \Gamma \nabla(\phi \zeta'_i) A_i)$, there is always a 2nd degree- precision interpolation. Fluent developers suggest starting a simulation with the first order method, and then switch to the second order. For further details on this argument, see Ansys Fluent Theory Guide [34].

4.7.3 Initialization

The initialization of the problem is a fundamental phase of the CFD simulations. Each variable, in fact, must be initialized before starting the iterative process. A realistic initialization improves the solution stability and accelerates the convergence. Two basic initializations are available in Fluent: the standard initialization and the hybrid initialization. With the standard initialization the user chooses an inlet boundary and specifies the velocities and the turbulence parameters of that particular boundary. These values will be taken as starting points in each point of the domain. With the hybrid initialization, the potential equations are solved in the fluid domain to find the velocity and pressure field. Other quantities such as temperature, turbulent kinetic energy and turbulent dissipation rate are found with an averaging operated in the entire domain. The hybrid initialization is the default option.

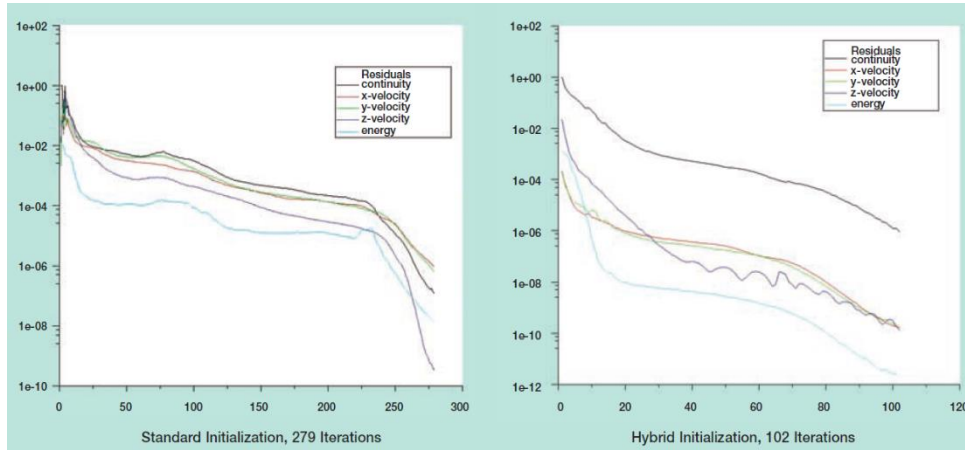


Figure 4.15: utility of using the hybrid initialization against the standard initialization [36].

In 2006 a new type of initialization was introduced, the Full multigrid initialization (Fmg). With Fmg, which is available only for single-phase flows, the Euler equations are solved in the entire domain. This method should provide the best starting point for a simulation, especially in the case of turbomachinery, or external flows problems. The initialization time is longer than in the standard initialization, but this time is recovered thanks to the faster convergence. Further details are available in the Ansys Fluent user's

guide [31]. A previous calculated solution can be used as initial condition when changes are made to the case setup. For example, this procedure is useful when it is desired to simulate a rotor running at different rotational speeds, or again when results from a fine mesh are available, and a simulation with a coarser mesh has to be run. In order to do so, the previous solution must be saved [*file>interpolate>write data*], and to initialize the next run the solution interpolation command shall be used [31].

4.7.4 Boundary conditions

The choice of the boundary conditions depends on the physics of the phenomenon to be modeled. In this case, a hovering condition is studied, and this influences the inlet condition. In fact, a pressure inlet is inserted with a value of total pressure of 101325 Pa, to simulate the fact that there is no air motion at the inlet location (2.25 m above the rotor). This condition is good to simulate an unconfined flow, when the value of the pressure is known. The turbulence characteristics are left to the default value. For what concerns the outer wall, a stationary wall condition is chosen. The outlet condition is a pressure outlet with a static pressure value of 101325 Pa. Moreover, the determination of eventual backflow is imposed to be calculated from the pressure values of the neighboring cells. The boundary condition at the rotor is a moving wall with no relative velocity with respect to the adjacent moving zone: in this way, it is simulated the fact that the rotor is moving with the rotational speed of the moving frame of reference.

Due to the considerations expressed above, for the simulations of the present work the coupled solver is chosen, together with a 2nd order discretization scheme for momentum, pressure, turbulent kinetic energy and turbulent dissipation rate. The $k - \omega$ SST turbulence model is chosen because of its ability of working with low Re number flows, and its ability of switching the formulation to better behave in different situations. The Fmg-initialization is always used, except for the case in which it is possible to have a previous calculation as starting point. The overall choices are resumed in the table below:

Table 4: Setup of the CFD simulations

Solver	Coupled solver
Approach	MRF method
Discretization scheme	Second order upwind (for all quantities)
Turbulence model	SST $k - \omega$
Initialization type	Fmg- initialization
Inlet BC	Pressure inlet
Outlet BC	Pressure outlet
Outerwall BC	Stationary wall
Rotor BC	No-slip condition

4.8 Analysis of moving domain dimensions

As it was explained in the paragraph dedicated to the study of the state of art, the problem of finding the best moving domain dimensions to describe the physics of a rotating system challenged many researchers in the last few years [22], [23]. There is no prior solution to this question, since there are too many variables that could affect this behavior, such as tip vortices dimensions, rotating element geometry, speed of rotation and so on. This leads to the need of making a sensitivity study of rotor performances for different moving domain dimensions, once fixed all the other parameters. The meshing parameters are kept constant for each surface, in order to keep the moving domain dimensions as the only varying parameter. In this way the total number of elements increases together with the moving domain size.

4.8.1 Geometry

For the realization of this study, the untwisted straight blade is chosen, with a constant pitching angle equal to $\theta_0 = 15^\circ$. The overall domain is a cylinder having a basis diameter equal to 3.54 m and a height of 7.06 m. The rotor is located at 2.25 m from the inlet surface, with its rotational axis coincident with the cylinder's one. As explained in the section dedicated to the geometrical model, both the moving and fixed domain are built using the command *enclosure*, which needs the specification of {radial distance from inner object; distance above the inner object; distance below the inner object}: in this way, both the fixed and moving domain dimensions are changed in order to obtain the above-mentioned overall footprint.

The moving domains chosen for the analysis are the following:

- Domain 1: {25 mm; 50 mm; 50 mm}
- Domain 2: {50 mm; 100 mm; 100 mm}
- Domain 3: {100 mm; 200 mm; 250 mm}
- Domain 4: {150 mm; 250 mm; 300 mm}
- Domain 5: {200 mm; 300 mm; 400 mm}

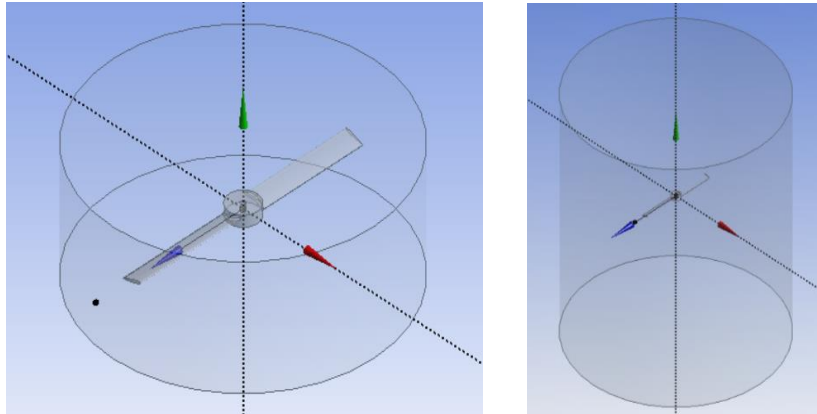


Figure 4.16: Examples of moving domains tested. The domain 1 is represented in the left, while the domain 5 is in the right.

4.8.2 Mesh

The parameters chosen for the mesh definition are listed in the following table.

Table 5: Meshing parameters for the moving domain analysis

Moving domain	Moving interface	Rotor	Fixed domain	
Type	Element size	Element size	Type	Sphere of influence
Element size	15 mm	0.5 mm	Sphere radius	350 mm
Defeature size	0.1 mm	0.1 mm	Element size	20 mm
Size function	curvature	Proximity & curvature		
Curvature normal angle	12°	12°		

The number of elements change with the domain dimensions, from the minimum value of $2.34 \cdot 10^6$ in the case of the moving domain 1, to the maximum value of $2.38 \cdot 10^6$ obtained in the case of the moving domain 3. It is expected that the cases 4 and 5 have an even higher number of elements but this is not obtained. In fact, they present $2.37 \cdot 10^6$ and $2.34 \cdot 10^6$ elements respectively. Each mesh tested presents good quality parameters: considering the AR, the mean value oscillates between 1.92 (moving domain 2) and 1.93 (moving domain 5), while the maximum standard deviation is equal to 0.503 (moving domain 1). This leads to meshes in which the 99.5% of the elements have an AR lower than 3.44, following the statistical normal distribution, and considering a cover factor equal to 3 (see table 6). In the table, μ_v represents the mean value of a data set, while σ_v represents the standard deviation. The same procedure has been done with the skewness, finding that the 99.5% of elements have a value lower than 0.696.

Table 6: AR and Skewness statistic distribution

	Domain 1	Domain 2	Domain 3	Domain 4	Domain 5
AR $\mu_v + 3\sigma_v$	3.436	3.429	3.432	3.430	3.435
Skewness $\mu_v + 3\sigma_v$	0.696	0.693	0.692	0.693	0.696

4.8.3 Results

The convergence of the simulation is set as all the residuals reach a value below $1 \cdot 10^5$. An ulterior parameter that is checked to evaluate the accuracy of the simulation is the difference between the mass flux entering in the domain through the inlet, and the mass flux exiting the domain through the outlet. In these analyses, such value is always lower than $1 \cdot 10^{-7}$. Changing the moving domain dimensions cause variations in the thrust, power, and consequently in FM. In all cases, there is no evidence of linear correlation between the domain size and the thrust or power values. This non-linear behavior is clearly visible from the figure 4.17.

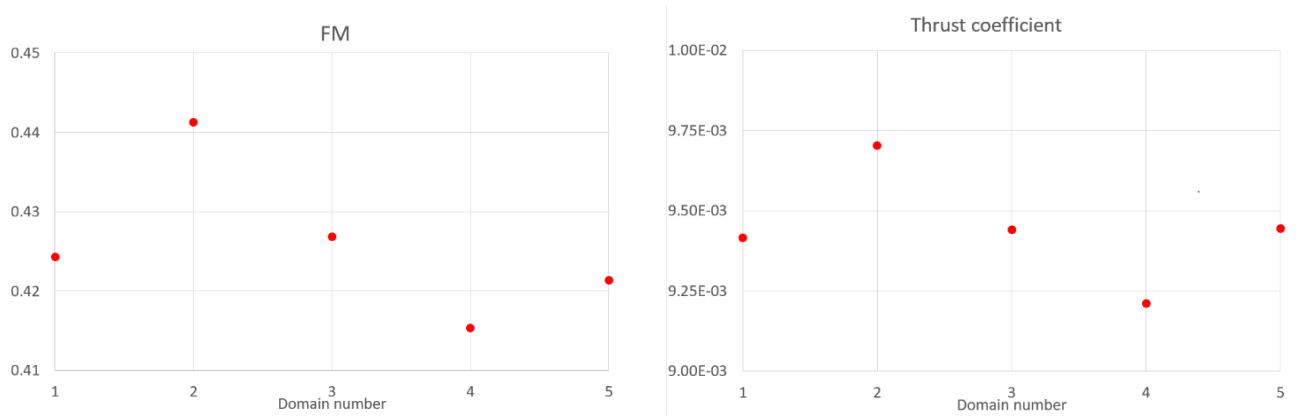


Figure 4.17: FM and thrust coefficient for the five domains tested

However, these differences are small when confronted in a relative way. The minimum values for each one of the three quantities are obtained with the domain 4, which is set as a reference. The percentual differences relative to it are always less than 5.4% in term of thrust, 2.35% in term of power, and 6.2% in term of FM (see figure 4.18 - right).

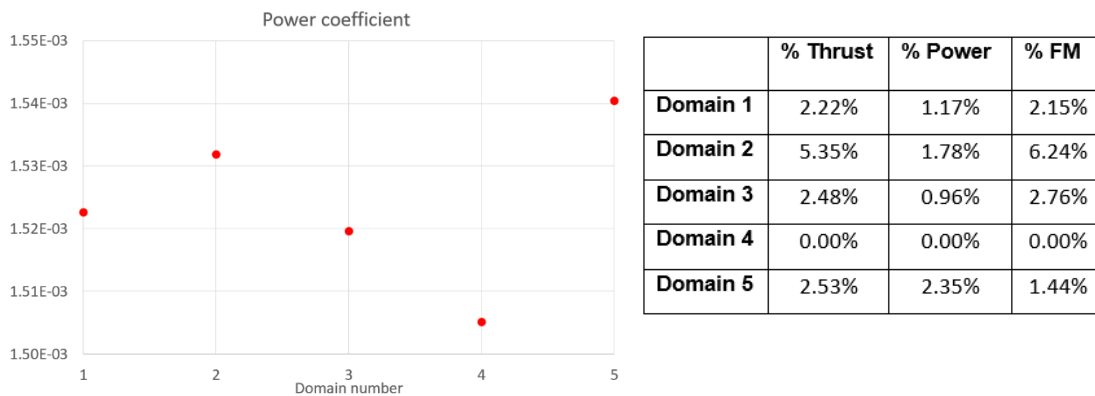


Figure 4.18: Power coefficient for the five domains tested (left). On the right, table showing the percentage discrepancies between the domain 4 and the others

From the absolute velocity contours plotted in the YZ plane, some interesting features could be noticed, see figure 4.19. In fact, the first domain appears to be inadequate since the interface location near the rotor, hinders the flow development, causing a noticeable discontinuity, both above and below the rotor. The presence of such discontinuities has been verified also when plotting the velocity contours in differently oriented planes. As the domain dimensions increase, a reduction of these errors is noticed. In fact, it can be said that, although there is still an unperfect passage between moving and fixed domain, starting from the moving domain 3, the flow below the rotor seems to reach an adequate shape.

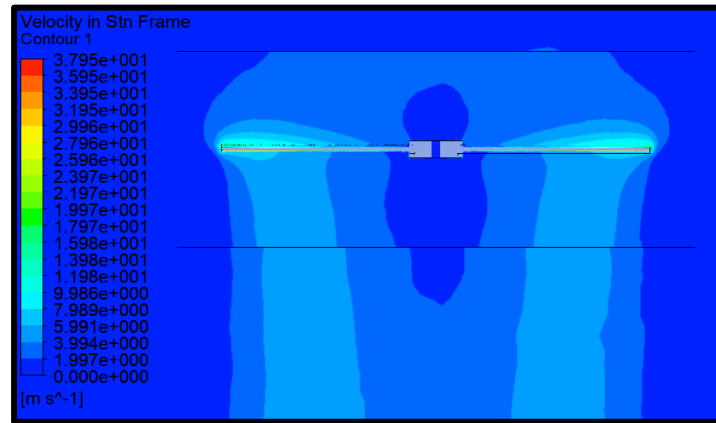


Figure 4.19: Velocity contour for domain 1, plotted on the YZ plane

The induced velocity distribution has been checked by determining the y-velocity values along a horizontal line collocated 15 mm below the rotor (see figure 4.20). The trend is similar for all cases, in fact the percentage difference is below 5% for most of the blade length. The greater offsets are present in the tip region: as the domain dimension increases, a rise of the induced velocity is noticeable. As found by Stajuda, Karczewski and other in [22], it is fundamental to confront simulation results with experimental data in order to select the proper domain dimension for the most correct analyses. In absence of that, the domain 4 is selected as the basis domain for all the simulations in this work: the motivations rely on a good representation of the wake region, and on the fact that it gives the lower values in term of FM. As experimental results will be available, a proper selection of the moving domain dimension should be made.

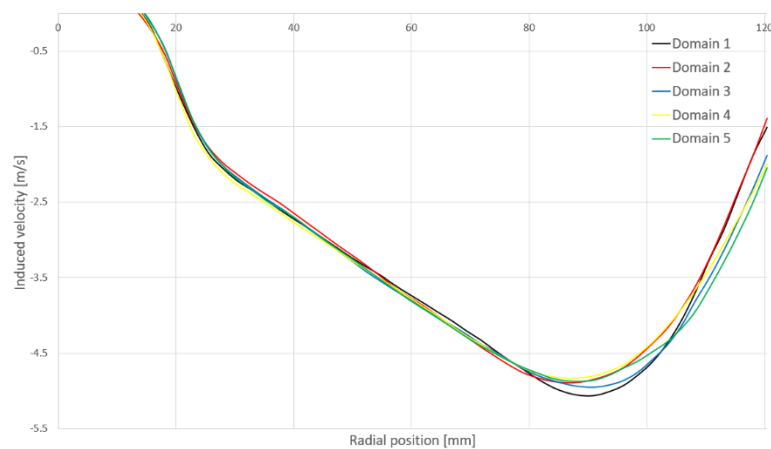


Figure 4.20: Induced velocity distribution 15 mm below the rotor, parametrized for different domain dimensions

4.9 Analysis of mesh sensitivity

After the domain definition, the influence of number of elements on the results is required in order to choose the mesh to be used for the following analyses. In order to do so, four different meshes are prepared, with increasing number of elements from a minimum of $1.29 \cdot 10^6$ to a maximum of $2.53 \cdot 10^6$. As it was explained in the Mesh section, these variations are obtained changing the element size in the sizing procedure, but keeping the meshing strategy common. The quality parameter of the various meshes are presented in table 8.

Table 8: Statistic parameters for the mesh sensitivity analysis

	Mean AR	Standard deviation (AR)	Max AR	Mean Skewness	Standard deviation (SK)	Max Skewness	N° elements	N° nodes
Coarse	1.942	0.503	13.46	0.263	0.149	0.852	1'290'524	391'305
Medium	1.937	0.459	12.17	0.269	0.129	0.845	1'959'424	514'256
Medium-fine	1.932	0.443	12.1	0.264	0.131	0.837	2'276'853	639'644
Fine	1.912	0.437	12.1	0.260	0.129	0.837	2'530'856	685'922

As the number of elements increases, an increasing in the thrust production is noticed, together with an oscillation in term of power consumption. This causes the FM to increase, reaching an almost flat behavior between the medium-fine and fine mesh (see figure 4.21).

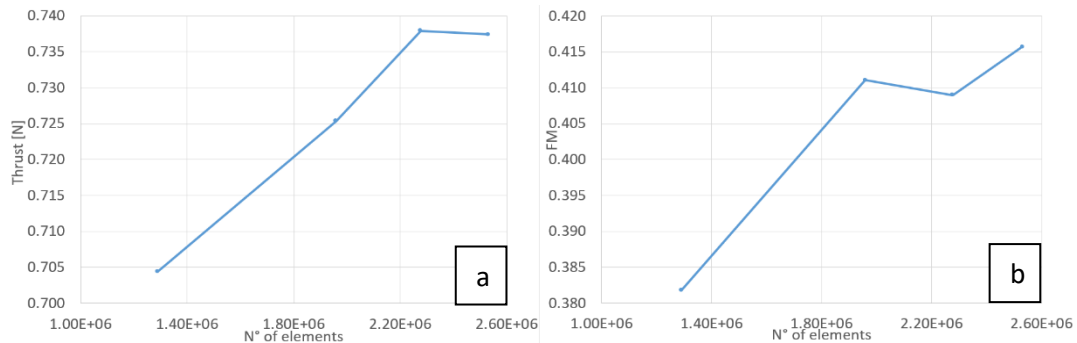


Figure 4.21: Thrust (a) and FM (b) trend varying the number of elements

Setting the finer mesh results as a reference, the percentual differences from them are evaluated to understand the error committed utilizing coarser meshes (see table 9). It must be noticed that a more correct approach would require experimental results, to be set as reference point. This consideration, in union with the only computational resource available (which characteristics have been shown in section 4.4) lead to choose the medium-fine mesh as the standard mesh for the work.

Table 9: Discrepancies between results with different meshes

	Δ Thrust	Δ Power	Δ FM
Coarse	4.48%	1.66%	8.16%
Medium	1.64%	1.35%	1.12%
Medium-fine	0.07%	1.75%	1.62%
Fine	-	-	-

5 Results

In this chapter, the results of various CFD simulations are presented. At first, the effect of varying the rotational velocity is studied. Afterwards, the focus moves on how FM varies at different $\frac{c_T}{\sigma}$ ratios, for the rotors studied in hovering condition. Both the cases with and without twisting are investigated, as well as the effect of having a forward or backward curvature. The results are confronted with the BEMT results and with experimental tests made with the SB, SCB, TE1B and TE2B untwisted rotor. A successive analysis is made with ascending flight. Finally, the results with the insertion of a rounded tip are presented.

5.1 Rotational velocity variation

The first study concerns the effect of different rotational velocities on rotor performances. For such purpose, the SB rotor is used, with a constant pitch angle of 15° . The interval of rotational speed tested is between 2800 and 6500 RPM. Eleven simulations are realized following an increasing speed order, so that the starting point of a generic simulation can be derived from the previous one, because this guarantees a faster convergence. As the rotational speed is increased, the thrust increased with the square of the velocity, while the power with the cube. This is shown in the figure 5.1, where the red lines represent the theoretical results:

$$T = \rho A (\Omega R)^2 C_T \quad (5.1)$$

$$P = \rho A (\Omega R)^3 C_P \quad (5.2)$$

In which for C_T and C_P the mean between all the simulations has been considered.

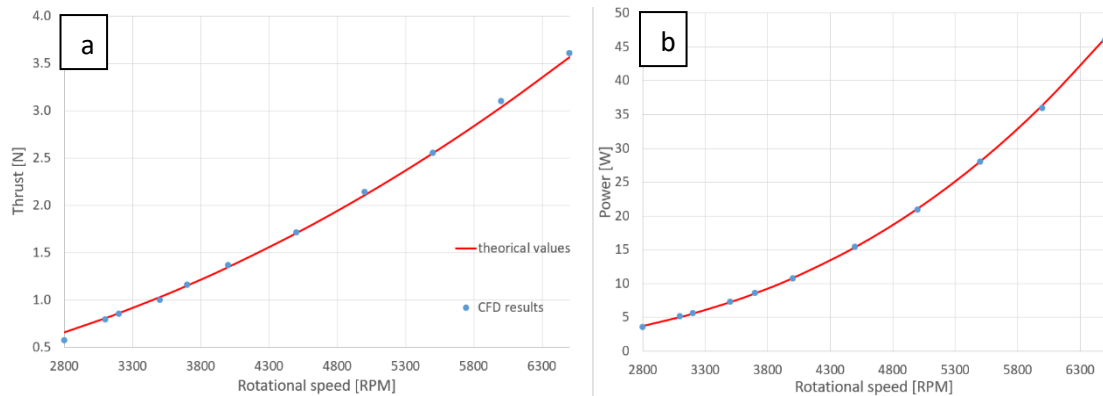


Figure 5.1: Thrust (a) and Power (b) for the straight blade at different rotational velocities

The thrust and power coefficient, instead, don't follow the behavior of their parent quantities (see figure 5.2 a-b). In fact, their variation is very reduced: the relative difference between maximum and minimum thrust and power coefficient value in the rotational speed range between 3000 RPM and 6500 RPM is around 5%. The FM (see figure 5.2 c) presents an improvement moving towards higher rotational velocities, varying between 0.42 and 0.45, for a global improvement of 9.2% between 3100 and 6000 RPM. At 2800 RPM the FM is quite lower, equal to 0.366. From these considerations it seems that moving faster the rotor could improve the hovering performances and this is thought to be caused by the increase of the Re number with consequent improvement in aerodynamic efficiency. The upper angular velocity limit depends on the rotor structural capability to withstand the aerodynamic and rotational load acting on it.

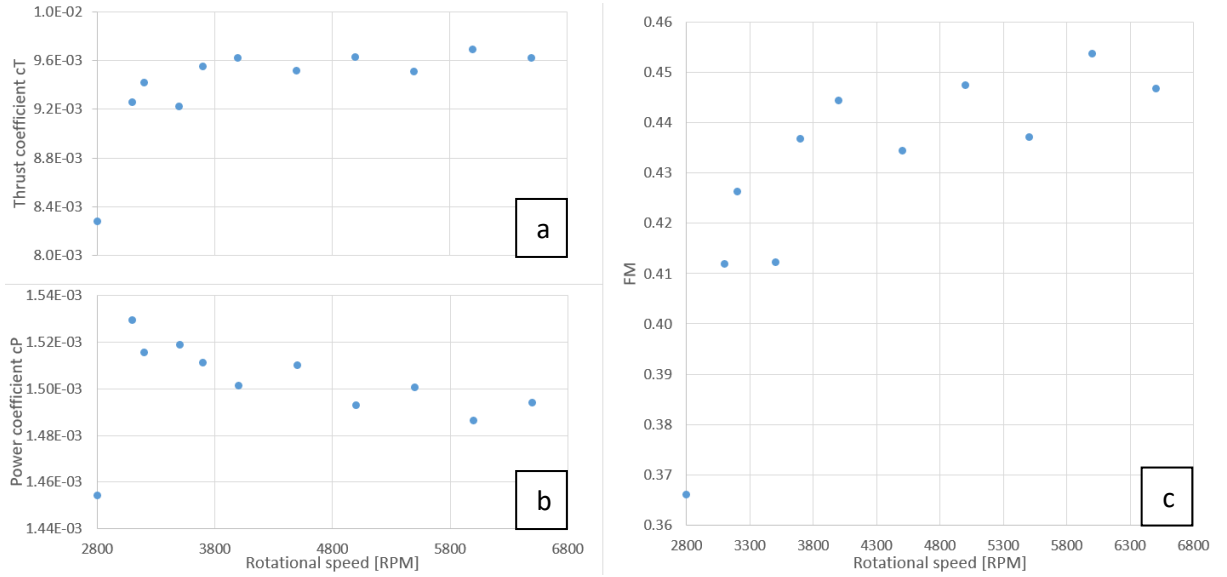


Figure 5.2: Thrust coefficient, Power coefficient and FM for the straight blade at various rotational velocities

5.2 Untwisted blades-backward curvature

In order to evaluate how FM behaves at different $\frac{c_T}{\sigma}$ ratios for the four backward-curved blades studied in this work, the approach of keeping fixed the rotational speed, varying the root pitch angle is chosen. In the case of untwisted blades, five different pitch angles are considered, namely $15^\circ, 17^\circ, 19^\circ, 21^\circ, 25^\circ$ while the rotational speed is kept to 3000 RPM. Although drone rotors angular speeds could reach values up to 10,000 RPM and more, the choice of a relatively low value relies on the aim of the work. In fact, another thesis purpose is to verify how different 3D printing procedures can be used for producing small scale rotors (see Appendix A1). The structural properties of the pieces depend on the material, as well as the technique used, so it is decided to operate in safety, not increasing too much the rotational forces that would act on a rotor when tested. The comparison between the FM obtained with the four different rotors brings interesting results (see figure 5.3). The straight blade appears to be the best configuration for a great interval of normalized thrust coefficient, ending at $\frac{c_T}{\sigma} \approx 0.14$. Every rotor has its

optimum working point around $\frac{c_T}{\sigma} = 0.11$, and next to the maximum value the performances are almost constant (see the presence of a plateau in all cases, more pronounced in the case of the straight blade). In order to understand the effect of curvature at the outer part of the blade, a comparison between the SB rotor and the SCB is done, since the only difference between the two is the curvature present in the last 30% of the radial dimension (section 4.5). It is noticeable that having this curvature brings to lower thrust values, and to a decrease in the overall performance: in fact, a decrement of thrust production between 4% and 8% is present, with the maximum difference for the blade having 21° pitch angle, equal to 8.26%. Considering the FM, the highest discrepancy is in the case of 17° pitch angle, for which the FM of the SB rotor is 6% higher than the SCB case. The two total curved blades TE1B and TE2B differ only for the tip shape: the TE2B presents a tip aligned with the air flow direction, without increasing the radial dimension of the rotor and presenting a wider blade area. This is at the basis of the greater thrust generation that characterizes this blade: for all the cases tested, the thrust produced by TE2B is between 5% and 20% higher than the one produced by TE1B. The power requirement increases as well, but not sufficiently to hinder the FM improvement seen in the TE2B case.

Table 10: Thrust comparison between the backward untwisted rotors. The percentages are calculated with respect to the straight blade

Root Pitch angle	STRAIGHT Thrust [N]	SCB Thrust [N]	TE1B Thrust [N]	TE2B Thrust [N]
15°	0.74	0.70 (-5.63%)	0.74 (-0.06%)	0.78 (5.76%)
17°	0.87	0.82 (-6.33%)	0.80 (-7.93%)	0.93 (6.94%)
19°	0.97	0.92 (-5.89%)	0.92 (-5.77%)	1.06 (9.27%)
21°	1.09	1.01 (-7.63%)	1.02 (-6.40%)	1.23 (12.72%)

From these results it is apparent the very important role that tip shape has in the drone rotors performances, since it is the region where the highest velocities are found, and the highest thrust is produced. For high root pitch angle values (and consequently high values of $\frac{c_T}{\sigma}$), the decay in the performance for the TE2B rotor is not as evident as that of the straight blade: this reflects on a higher FM. In this sense, the TE2B rotor seems to better operate at higher root pitch angles (figure 5.3).

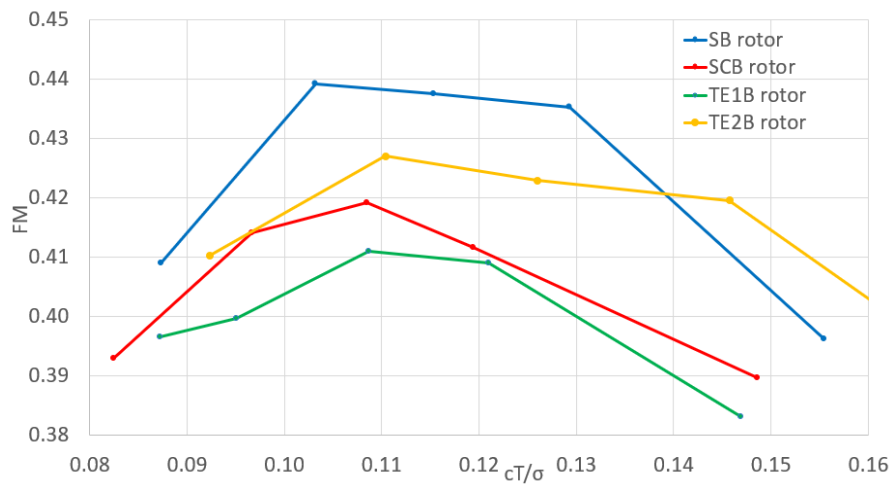


Figure 5.3: FM behavior for untwisted blades, in case of backward curvature

5.3 Twisted blades – backward curvature

The insertion of a pitch variation along the blade is then considered. In this way it is possible to quantify the twisting effect on rotor performance at low Re , as well as check if there is a noticeable coupling between the curvature and the twist variation. A $10^\circ/m$ twisting variation is inserted, imposing that the angle at 75% of the blade length is equal to the pitch angle in the untwisted case. In this way, according to the BET, the thrust production should be the same in the two cases (see section 2.2). This is almost true in the case of normal scale rotors [24], and it is found to be reasonably true for subscale rotors, even though the differences in thrust are more evident. For all the four rotors the differences between the thrust produced by the untwisted and the twisted type is below 5%.

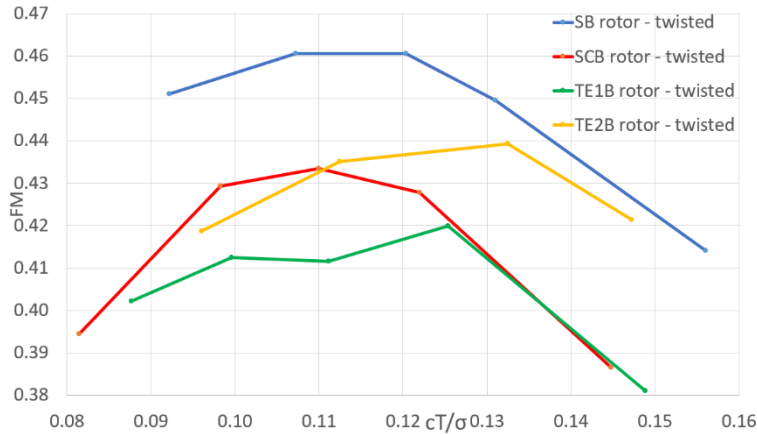


Figure 5.4: FM behavior for twisted blades, in the case of backward curvature

Considering the SB rotor, the twisting insertion is shown to improve both the thrust production, and the FM. In particular, the improvement in FM is between 5% and 10% in the range of cases studied (see figure 5.5). The region of best performance is again between $\frac{cT}{\sigma} = 0.105$ and $\frac{cT}{\sigma} = 0.125$ for the twisted blade. Considering the curved blade rotors, the improvement is found to be always around 3%, so that a small decrease on the beneficial effect of twisting is noticed. This fact leads to the better behavior of the SB rotor with respect to the TE2B rotor at higher thrust production, in odds with what was found previously in the untwisted case (see figure 5.4).

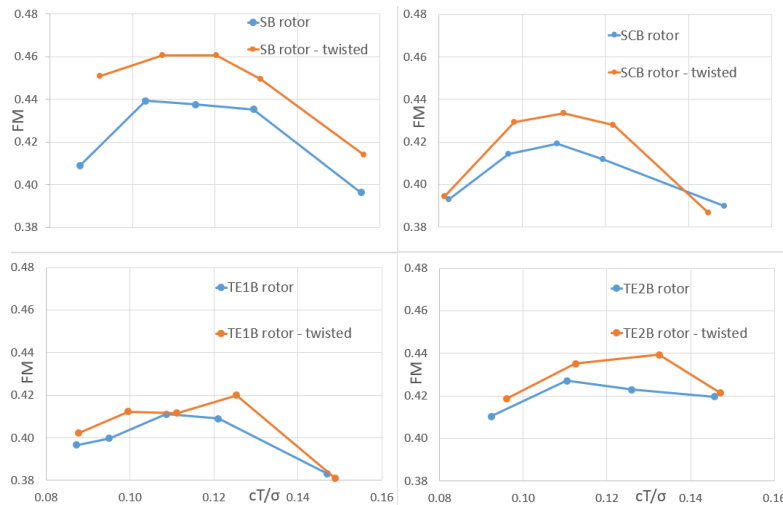


Figure 5.5: Effect of inserting the twisting variation for the straight blade rotor and the backward curved rotors

5.4 Untwisted blades – forward curvature

As explained in section 4.5, also the presence of a forward curvature is investigated. The curvature parameters are the same as for the backward curved blades, but they are mirrored towards the advancing side of the blade. In this way, it is possible to verify which curvature direction is preferred for small scale rotors. The blade section is swept keeping its shape and following the path defined for the curvature insertion, and this has some influence in the results. At first, let's consider the SB rotor in comparison with the SCF rotor. At the tip a thicker part facing the air flow direction is present: this part is responsible of a great drag increasing without bringing any benefit on the thrust production. Moreover, it seems to facilitate the separation of the flow, thus increasing the blade tip vortices dimensions. This is qualitatively shown in the figure 5.6 a-b, where the vortex region with a swirling strength of 0.01 are compared for the two blades with the same pitching angle of 19° .

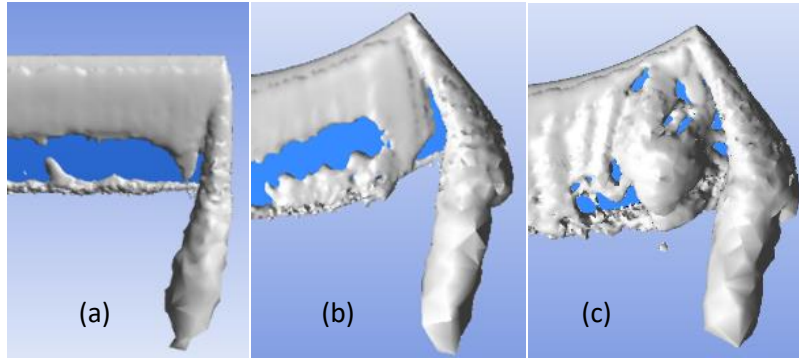


Figure 5.6: Comparison between the contour of the region at constant swirling strength for the straight blade (a) and the single forward-curved blade at 19° (b) and 25° (c) of root pitch angle

As the root pitch angle is increased the flow separation is more evident (see figure 5.6 c), and this is reflected on a performance decay for the SCF rotor at high $\frac{c_T}{\sigma}$ values. In conclusion, the SCF rotor presents an almost constant FM value in a $\frac{c_T}{\sigma}$ interval that end around 0.125, after which the performance decay is greater. In figure 5.7 a comparison is made between SCB and SCF rotor. Even though the thrust production is similar (see Appendix A3), with differences below the 2% in most of the cases studied, the SCB presents a 10% less power consumption, this leading to higher FM values.

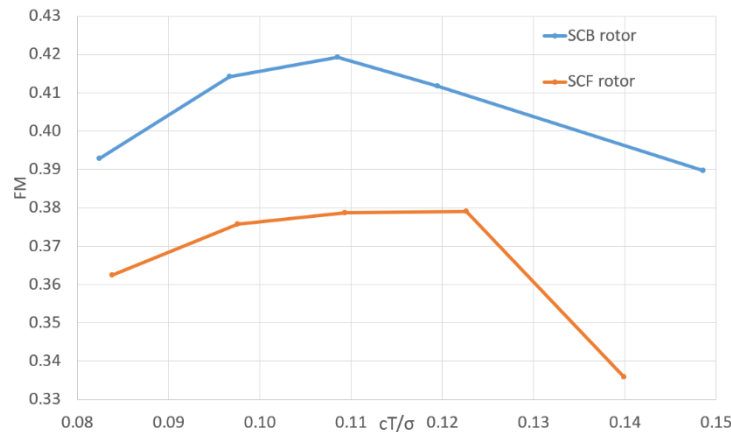


Figure 5.7: Comparison between the single curved blade performance with backward and forward curvature direction

The total curved TE1F rotor presents similar characteristics when studying the forward curvature. In fact, the area facing the air flow at the tip is even greater than the single curved case (see section 4.2), and this is reflected on a higher drag production and vortex generation. Again, the look of the vortex core region qualitatively justifies this behavior, when comparing the tip vortices at the same root pitch angle of 19° . (see figure 5.8 a-b). The SCF rotor produces higher thrust than the TE1F at the same root pitch angle, the differences being always between 5% and 9%. The greater vortices produced by the TE1F rotor cause a greater power requirement, so that the FM of the SCF is always higher, with a discrepancy between the 6% for the root pitch angle equal to 25° to values near 15% in the other cases.

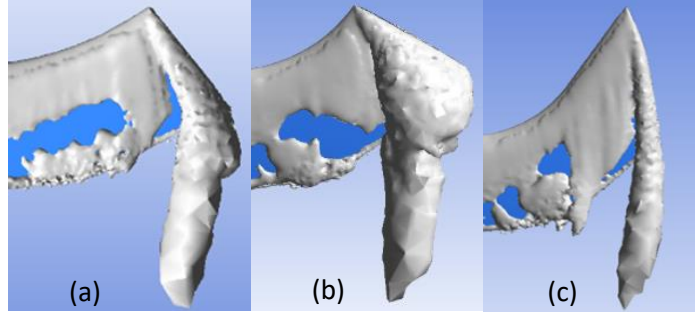


Figure 5.8: Region at constant swirling strength equal to 0.01 in the case of single curved blade SCF (a), TE1F (b) and TE2F (c) for a 19° root pitch angle

A clear improvement to the total curved performances is given by the adoption of the TE2F rotor. In fact, the last blade section is now parallel to the airflow, thus not facing it with a thick area. Moreover, it is clear as the TE2F presents a wider blade area, that causes a greater thrust production with respect to the TE1F. In term of percentages, TE2F produces around 15% more thrust than TE1F and around 6% more thrust than the SCF (see Appendix A3). The vortex region at the tip of the blade is smaller, as shown in figure 5.8 c, so it could be said that the tip effects are less evident than in the other cases, thus reducing the induced losses. This has some benefits in the FM, that is the highest between the forward curved blades till a value of $\frac{c_T}{\sigma} = 0.12$. At higher thrust coefficients, the SCF rotor seems to behave slightly better (see figure 5.10). Comparing TE2B and TE2F, it is found that incrementing the pitch angle, there is an increase in the gap between the two cases. This can be clearly seen in figure 5.9.

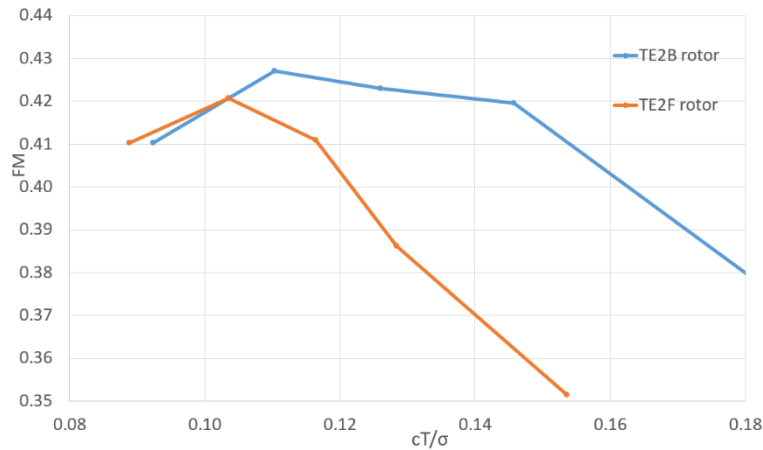


Figure 5.9: Comparison between the forward and backward curvature for the total curved blade TE2

In figure 5.10 the results regarding the forward untwisted case are presented. The reduction in term of FM with respect to the backward curvature is evident especially for the SCF rotor and the TE1F rotor. It can be said that having a forward curvature leads to an easier flow separation with consequent loss of performance. The next step is studying the insertion of twisting in the case of forward curvature.

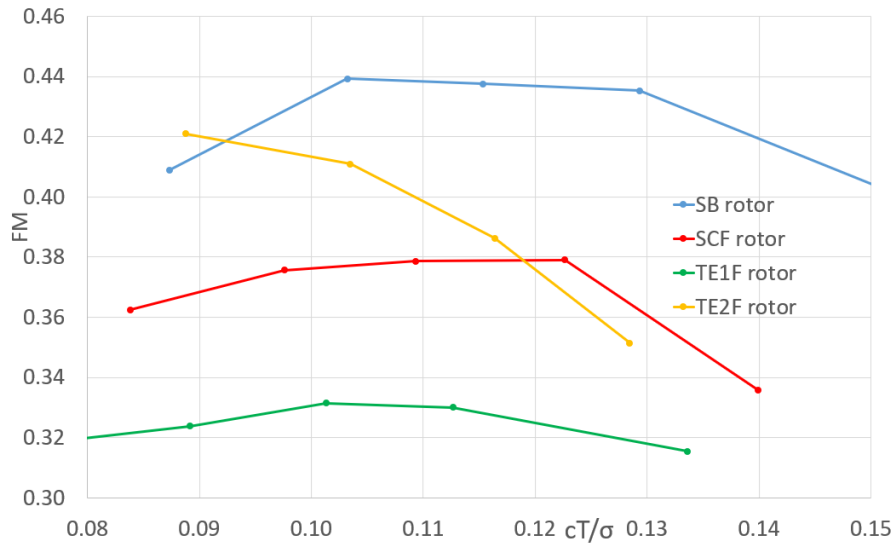


Figure 5.10: FM behavior for untwisted blades, in case of forward curvature

5.5 Twisted blades – forward curvature

Due to the twisting the SCF rotor presents an FM improvement between 3% and 11%, while the thrust production is almost similar with the maximum discrepancy equal to 3%. In fact, the lower pitch angle at the tip could cause a reduction in term of tip vortex dimension between rotors producing the same thrust amount. The benefits of inserting the twisting can be seen also in the induced velocity distribution. The

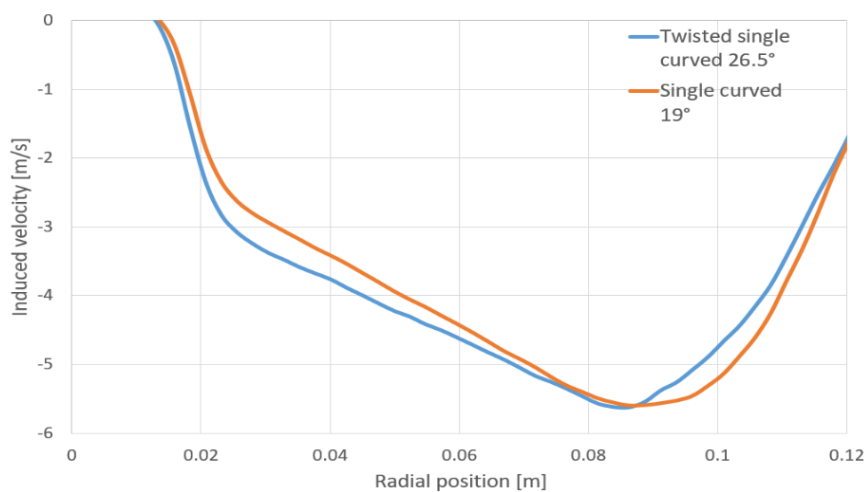


Figure 5.11: Comparison of induced velocities between the 19° untwisted blade and the 26.5° twisted blade, having a twist variation of 10°

values of y-velocity are plotted along a line located 15 mm below the rotor horizontal plane, for the case of 19° untwisted single curved blade and 26.5° twisted single curved blade. The two rotors produce a thrust of around 0.92 N, with a difference below 1%. From figure 5.11 it is noticeable how the induced velocity appears more regular with the insertion of twisting, getting closer to the ideal constant value that would generate the best rotor efficiency. In the case of the TE1F rotor, inserting a twisting leads to some

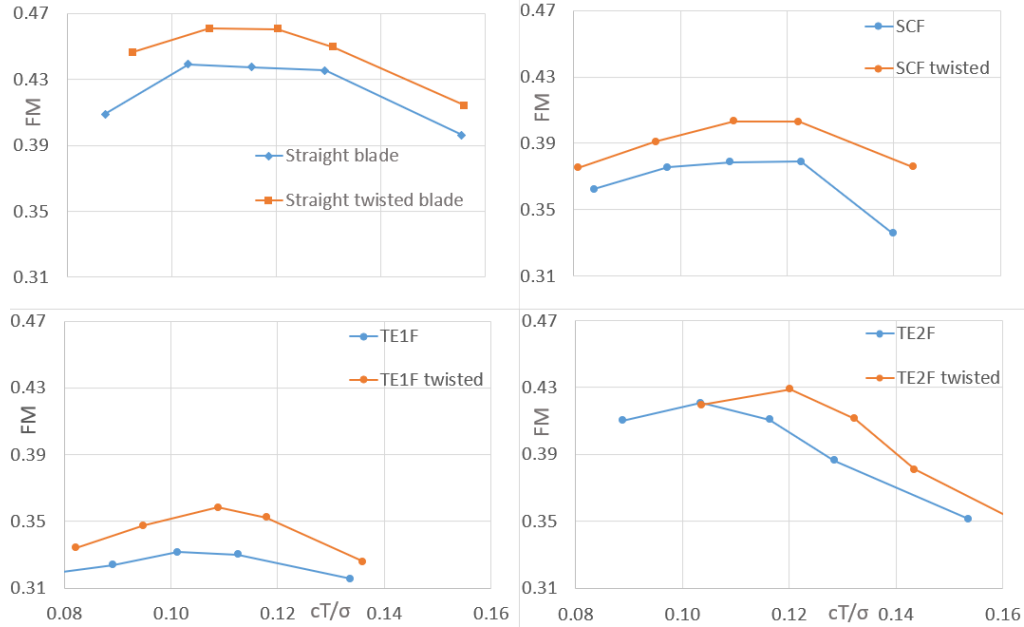


Figure 5.12: Effect of inserting the twisting variation for the straight blade rotor and the forward curved rotors

benefits in the FM, in a higher percentage than in the case of backward curvature. In fact, the improvement is between 3% and 8%. In the case of the other tip shape, TE2F, the improvement is always present, but reduced to a value of 2%. A resume of the twisting insertion effect is given in figure 5.12. From figure 5.13 is apparent how the TE2F rotor is the best configuration in the case of forward curvature, however the performances are far from the one obtained with the backward curvature, especially for the SCF and TE1F rotors.

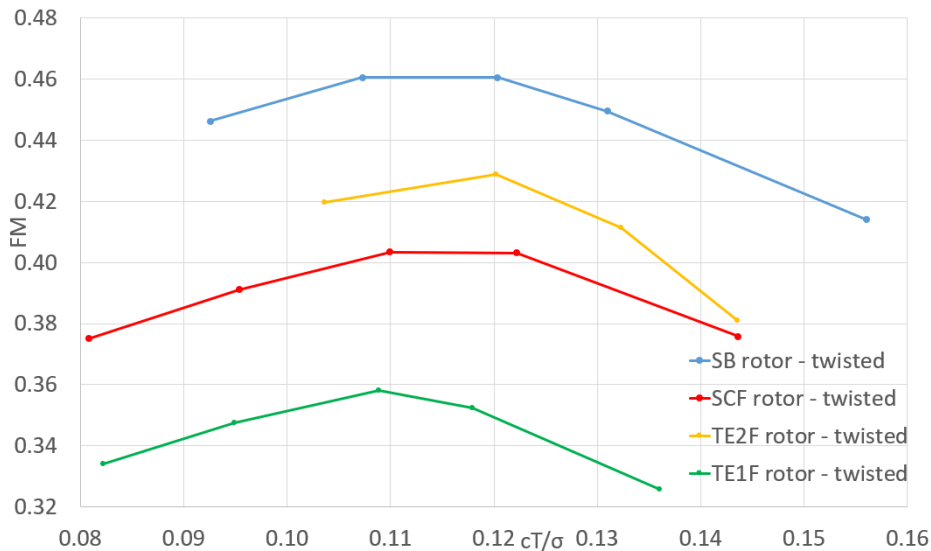


Figure 5.13: FM behavior for twisted blades, in the case of forward curvature

5.6 Comparison between BET and CFD results

In Chapter 3 the difficulty in applying the BEMT for the study of small-scale propellers operating in low Re regime has been presented. The results are compared with the CFD simulations to understand and quantify the differences. It is evident the higher prediction in term of FM made by the BEMT, around 30% in the case of the SB rotor, and even greater for the curved blades. Moreover, it is recalled here how with the BEMT after a root pitch angle of about 16° for the untwisted case and 24° for the twisted case, the thrust production started to decrease, because the majority of the blade elements began to operate in an interval of angles of attack characterized by low aerodynamic efficiency. The BEMT formulation developed in this work defines the curvature of the blade as a positive mean to increase the rotor efficiency, while this is not confirmed with the CFD. There are intervals of thrust coefficient in which the TE2B rotor appeared to be more performant than the SB, but the other curved configurations in hovering conditions are characterized by a lower FM.

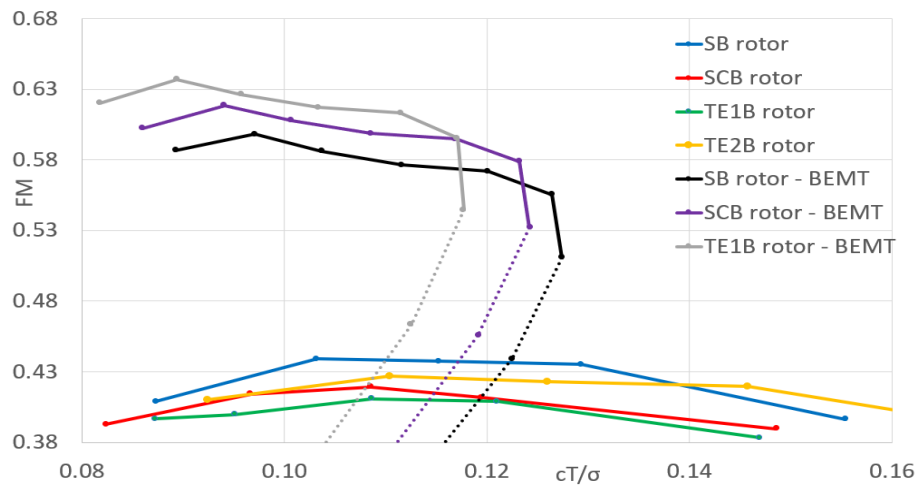


Figure 5.14: Comparison between BEMT and CFD data for the rotor studied

5.7 Comparison between CFD and experimental results

In the Appendix a detailed analysis of the 3D printing procedure used to design the rotors object of this study is presented, together with the results coming from the experimental test campaign realized using the test bench available at the University, which has been developed by Ines Amado [37] for a previous project. The rotors tested are printed with the SLA technology and this on one side gave the possibility of obtaining very smooth surfaces and an almost perfect description of the smaller details, like the blade tip or the infill between the blade and the hub. On the other side, the poor mechanical stiffness which characterizes the resin, turns out to complicate the procedure of aligning the rotor with the motor rotational axis, as well as the alignment of the two blades forming a generic rotor.

In most of the cases, except for the TE1B untwisted rotor, the CFD simulations underpredict the thrust production, while in term of FM there is no clear underprediction or overestimation, since the results

vary case by case. The discrepancies between CFD and experimental results are acceptable, below 8% in most cases, and are addressed to be caused by two distinguished factors. The first comes from the impossibility of knowing the real pitching angle which characterizes the resin-printed rotors, together with the inaccuracies in the alignment of the blades with the rotational axis. The second motivation derives from the CFD simulations, since the moving domain dimension turned out to be very influent in the determination of the forces generated by a rotating blade and should be calibrated with experimental data that were not available at the moment of the simulation definition (confront section 4.8).

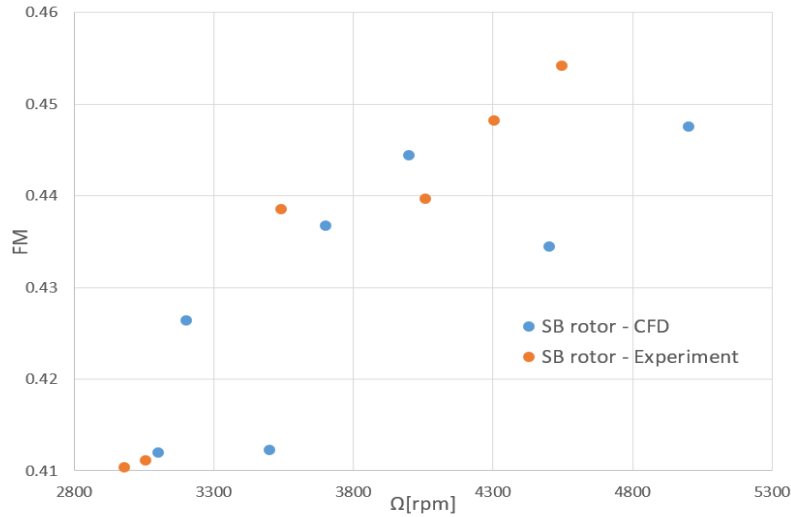


Figure 5.15: FM vs rotational speed; comparison between CFD and experimental data

The experimental data regarding the 15° root pitch angle SB rotor, which is put in rotation at different angular speeds between 1090 RPM and 5043 RPM, confirm the tendency of the FM to increase when the rotor is operating at higher rotational velocities, as depicted in figure 5.15. The thrust and power behaviors inside this interval are in good accordance with the CFD prediction (see Appendix A.2.1).

One of the most interesting results that derives from the experimental test of the printed rotors is the performance of TE2B rotor, which appears to behave better than the SB not only at high thrust coefficient, as found with the CFD analysis. According to the experimental data, at 3000 RPM the twisted TE2B rotor with a root pitch angle of 22.5° presents a $FM = 0.455$, 8% higher than what predicted computationally.

5.8 Axial flight results

Five twisted configurations with a root pitch angle of 26.5° are studied also in the case of ascending flight condition, namely the SB, SCB, TE2B, SCF, TE2F rotors. The flight condition is obtained by imposing a velocity inlet equal to the ascending velocity and keeping the moving domain in rotation with the desired angular speed. Two analyses are realized, the first keeping a constant rotational speed of 3000 RPM, and increasing the climbing velocity, and the second keeping constant the thrust to the hovering value as the climbing velocity is increased, by adapting the rotor rotational speed. The results of the first analysis are compared to the behavior shown in [24], plotting the thrust and power coefficients versus the climbing ratio $\frac{v_c}{v_h}$. As depicted in figures 5.16 a, as the climbing velocity is increased, a decrease in the thrust coefficient is noticeable for every blade: in fact, the angle of attack α is reduced as v_c reaches higher values, thus causing a reduction for the rotor thrust. The power coefficient depicted in figure 5.16 b is calculated with the following equation:

$$C_P = C_{P,CFD} + \frac{C_T v_{climb}}{\Omega R} \quad (5.3)$$

In which $C_{P,CFD}$ is the coefficient representing the power needed to put the rotor in rotation, while the other term is the power needed for the ascending motion.

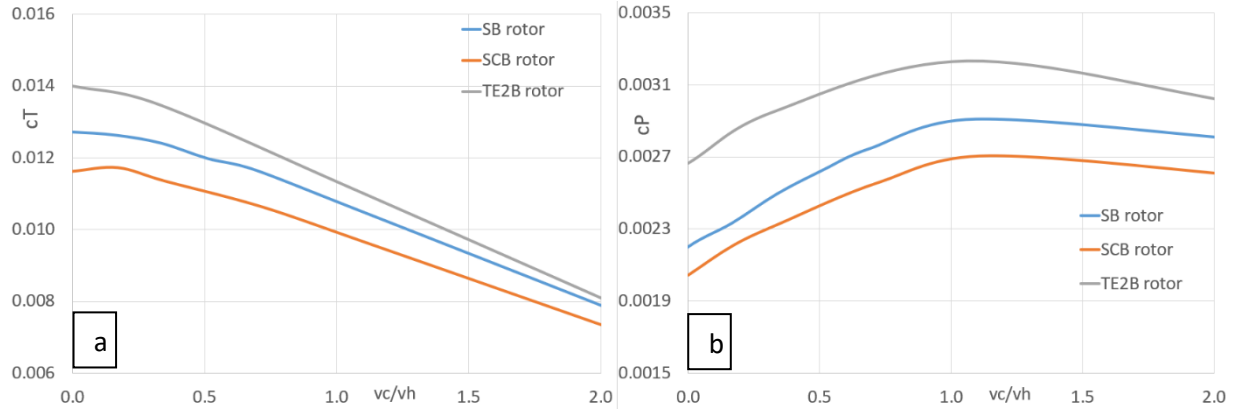


Figure 5.16: Thrust and power coefficients versus climbing ratio

The great decrease in thrust production for high climbing velocities causes also the power coefficient to a decrease after reaching the peak around $\frac{v_c}{v_h} = 1$.

In the second analysis the development of a steady climbing motion is done by increasing the rotational speed of the rotor. In the CFD simulations, the angular velocities are changed with the climbing velocity in order to have a maximum difference of 2.5% between the thrust produced in hovering and in the axial case, to satisfy the requirement of producing a constant thrust. The expression 5.4 is plotted in figure 5.17 a, in order to understand how the power requirements change as the ascending velocity is increased:

$$\frac{P_{climb}}{P_h} = \frac{P_{CFD,c} + T v_c}{P_{CFD,h}} \quad (5.4)$$

The term $P_{CFD,c}$ comprises the viscous drag, and the induced drag at the rotor disk, while the term $T v_c$ represents the climbing power. $P_{CFD,h}$ is the power required to hover.

Every rotor typology shows an increase in the power requirement as the climbing velocity gets higher, besides the induced and viscous contributes should decrease due to the decrease in the angle of attack [24]: it can be said that at higher climbing ratios the climbing power becomes the dominant term in the overall power request. The SB rotor presents the highest increase with respect to the hovering case at high $\frac{v_c}{v_h}$ values, followed by the backward curved configurations SCB and TE2B. The SCF and TE2F rotors present a smaller increase in the power with the climbing ratio, however the overall performance is scaled by the power required to hover, which is high for these two configurations.

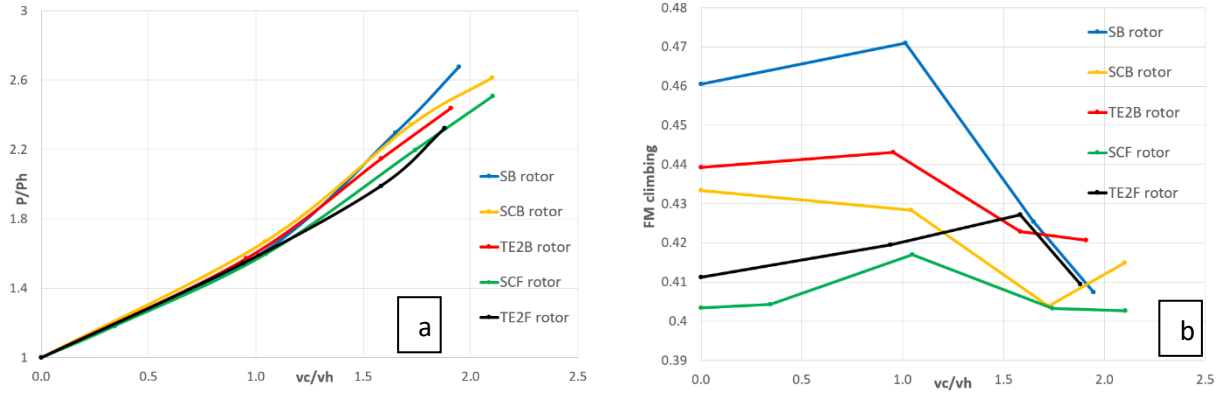


Figure 5.17: Climbing power ratio and climbing FM plotted versus the climbing ratio

Also the parameter FM_{climb} introduced in section 2.5 is plotted, for each rotor. All the rotors tested show a peak in the value of this parameter when the climbing ratio is closer to unity, with exception for the TE2F rotor, for which the peak is around $v_c/v_h \approx 1.6$. After this peak, a decrease is noticed: this means that at high climbing velocities the actual power required for the motion gets higher with respect to the ideal value. In this region, the best configuration seems to be TE2B rotor, which suffer a smaller decrease in the performance with respect to the SB rotor.

5.9 Tip modification results

From the results of the simulations previously done, it is apparent how the tip shape has a strong influence on the overall performances of a rotor. the three rotors SB3, TE3B and TE3F are designed in order to minimize the influence of a different tip shape, to permit the analysis of how the curvature affects the performances. These rotors are studied in hovering flight conditions, in the case of untwisted blades and with a root pitch angle which varies from 15° to 25° . At first the SB3 rotor is compared with the SB rotor (figure 5.18 a): the insertion of the new tip causes a decrement in the thrust produced between 5%

and 8.8%, while the FM presents an almost stable behavior, varying from 0.53% to 1.57%. Up to value $c_T/\sigma \approx 0.115$ the SB3 rotor appear to behave better than the SB rotor, requiring less power to hover for the production of the same thrust amount. A thrust reduction between 7% and 15% is noticed also in the case of the backward curved rotors TE2B and TE3B; also in this case, the FM presents instead similar values. Up to $\frac{c_T}{\sigma} \approx 0.135$ the TE3B rotor has a better FM with respect to the TE2B, while experiencing a strong performance decay at higher thrust values (which correspond to higher root pitch angles). The TE1B rotor presents lower performances for all the cases tested, as to be seen in figure 5.18 b.

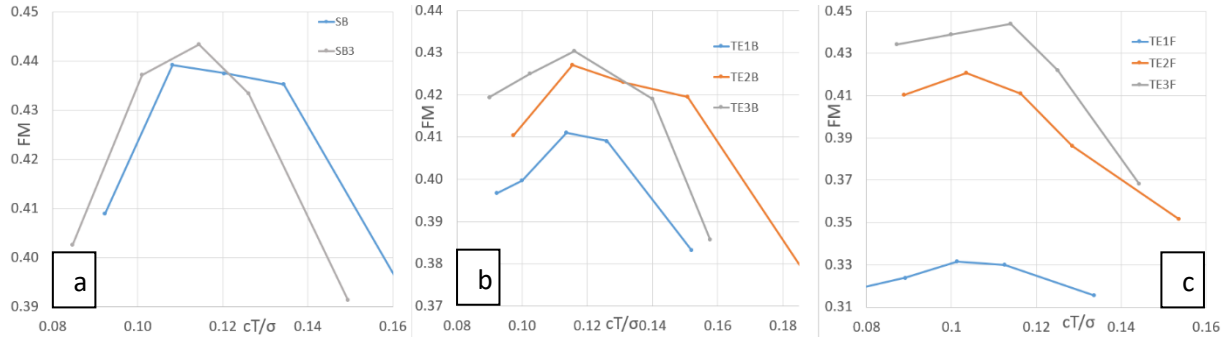


Figure 5.18: Comparison between the tip modified rotors and the standard tip rotors

Considering the rotors characterized by a forward curvature, the obtained results are particularly interesting (see figure 5.18 c). In this case, the thrust reduction is less evident, and it can be estimated to a value of 2% with respect to the TE2F rotor, while the FM experiences a high improvement, increasing between a value of 4.3% and 9.3%. In this way, the TE3F results the best configuration for a great interval of thrust coefficients. Comparing the tip modified rotors SB3, TE3B and TE3F a better insight in the effect of inserting a curvature can be made, since the tip presents the same shape. Considering rotors with the same root pitch angle, it is seen how inserting a curvature increase the thrust produced in all the case tested between 1% and 9% (see figure 5.19). At low thrust values (low root pitch angles), the SB3 and TE3F rotors present similar performances, while the TE3B rotor seems to be less efficient, but the opposite happens at higher thrust coefficients, for which the TE3B gets the higher thrust production and the higher FM. In this sense, it seems that when a rotor should operate at low thrust production the forward curvature is preferable, while the opposite happens at higher thrust requirements.

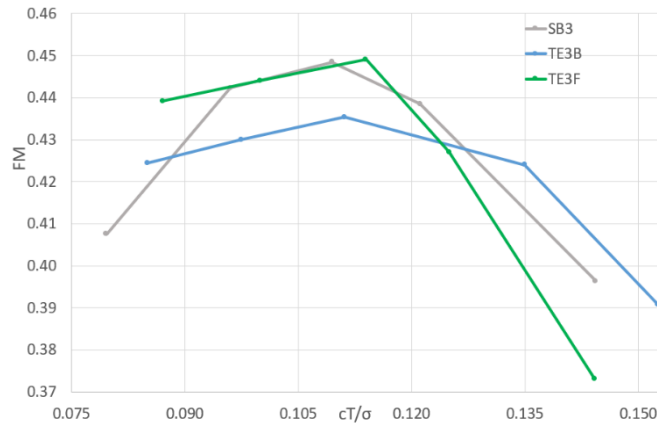


Figure 5.19: Comparison between SB3, TE3B and TE3F rotors

6 Conclusion and future developments

6.1 Conclusions

The BEMT appeared to be not adequate for the analysis of low Re propellers, in the formulation derived from [24]. The possibility of inserting the swirling velocity, as well as the influence of radial velocity should be studied to verify the possibility of predicting drones' performances with this theory. The code developed was however good in predicting the performances of full-scale helicopters. The CFD simulations showed how the SB rotor appears to be the best configuration in most of the cases, except for high pitch angles, for which the total curved TE2B rotor operates better. The insertion of curvature does not prevent the benefits coming from the insertion of twisting, nor in the case of backward curvature, nor in the case of forward curvature, in fact an improvement in the FM has been found when considering twisted blades. For all the analyses realized, the tip region appears to be of outstanding importance for rotor performances: this explains the great difference in the performance between TE1B and TE2B rotors, as well as TE1F and TE2F rotors. The tip vortices appear to be strongly linked with the change in rotor performances, as it is noticeable from the analysis of the swirling strength contours. The comparison of rotors with a standardized tip reveals how, according to CFD, the presence of a forward curvature may improve the hovering performances at low root pitch angles, while the backward curvature is desirable for high root pitch angles. In axial flight condition it seems that the curved rotors present a less evident increase in the power requirement when the climbing velocity increases. This fact should be further investigated by means of experimental tests.

Considering the 3D printing aspects, both the FDM and SLA technologies appear to be adapted in the development of propellers, each one with his pros and cons. The SLA methods is faster, giving the possibility of printing several objects in one session, and it creates objects with a very high surface quality, reducing to a minimum the need of user action in the post processing phase. On the other side, the flexibility of the material and the non-perfect flatness of the rotor hubs severely complicated the procedure of blade alignment to form the rotor as well as the alignment with the rotational axis (see Appendix). Moreover, further study is required to understand whether this flexible material may change the effective root pitch angle of the blade during the rotation, thus modifying the aerodynamic properties. The FDM methodology creates stiffer objects, which can be readily postprocessed to enhance the surface quality. The production time is higher, but no surface warping has been found in the object printed.

The experimental results show how the SLA printed blades can withstand the loads acting on them when rotating at moderately high angular velocities and appear to be in good agreement with the CFD prevision for most of the rotors. In fact, the benefit of introducing a twisting has been confirmed, as well as the importance of the tip region: the TE2B rotor has been proven to operate better than the TE1B

rotor in hovering condition. In this sense, the tip shape appears to influence the performance more than the simple insertion of a curvature.

6.2 Future developments

This work offers many possibilities of a future development. At first, the experimental campaign should be extended by testing rotors with different pitch angles and also the forward curved rotors. Also the axial flight condition should be experimentally tested. Moreover, the production of a rotor which could mix the surface smoothness of resin-printed parts with the stiffness of a basis structure should be addressed. Another aspect that could be further analyzed is the difference in noise production between the rotors studied in this work.

From a computational point of view, the moving domain dimensions should be calibrated with the experimental data, in order to maximize the accuracy of the MRF method; the implementation of the Moving Mesh method could be interesting in order to pass from a steady simulation to a transient.

Bibliography

- [1] A. Konak, «Medium» [Online]. Available: <https://medium.com/@ahmetkonak55/the-importance-and-future-of-drone-in-cargo-transportation-3ad20ff022d7>. [Last visit 04 05 2020].
- [2] R. D'Andrea, «Guest editorial can drones deliver?» *IEEE transactions on automatic science and engineering*, vol. 11, n. 3, pp. 647-648, 2014.
- [3] A. Goodchild and J. Toy, «Deliver by drone: an evaluation of unmanned aerial vehicle technology in reducing CO2 emissions in the delivery service industry» *Transport. Res. Part D Transport and Environment*, 2017.
- [4] «Volocopter GmbH» [Online]. Available: <https://www.volocopter.com/en/product/>. [Last visit 04 05 2020].
- [5] «Airbus» Airbus S.A.S., [Online]. Available: <https://www.airbus.com/innovation/urban-air-mobility/vehicle-demonstrators/vahana.html>. [Last visit 04 05 2020].
- [6] «Electric VTOL news TM» The vertical flight society, [Online]. Available: <https://evtol.news/aircraft/pop-up-next/>. [Last visit 04 05 2020].
- [7] M. A. McVeigh and F. J. McHugh, «Recent Advances in Rotor Technology at Boeing Vertol» *38th Annual Forum of the American Helicopter Society*, 1982.
- [8] J. Brandt and M. Selig, «Propeller performance data at low Reynolds numbers» *49th AIAA Aerospace Sciences Meeting including the New Horizons Forum and Aerospace Exposition*, p.1255, 2011.
- [9] M. Benedict, J. Winslow, Z. Hasnain and I. Chopra, «Experimental investigation of micro air vehicle scale helicopter rotor in hover» *International Journal of Micro Air Vehicles*, vol. 7, no. 3, pp. 231-255, 2015.
- [10] M. Ramasamy, «Flowfield of a rotating-wing micro air vehicle» *Journal of Aircraft*, vol. 44, n. 4, pp. 1236-1244, July 2007.
- [11] M. Ramasamy, «Understanding the aerodynamic efficiency of a hovering micro rotor» *Journal of the American Helicopter Society*, vol. 53, pp. 412-428, October 2008.
- [12] F. W. Schmitz, «Aerodynamik des flugmodells», Berlin-Charlottenburg: C. Lange, 1942.
- [13] J. H. McMaster and M. L. Henderson, «Low-speed single-element airfoil synthesis» *NASA conference publication*, vol. 2085, pp. 1-31, 1979.
- [14] E. V. Laitone, «Wind tunnel testing of wings at Reynolds number below 70000» *Experiments in fluids*, n. 23, pp. 405-409, 1997.
- [15] D.-H. Kim and J.-H. Yang, «Boundary layer and near-wake measurements of NACA 0012 airfoil at low Reynolds numbers» *47th AIAA Aerospace Sciences Meeting including The New Horizons Forum and Aerospace Exposition*, p. 1472, 2009.
- [16] Ohtake, Tomohisa, Nakae, Yusuke, Motohasi and Tatsuo, «Nonlinearity of the aerodynamic characteristics of NACA0012 aerofoil at low Reynolds numbers» *Journal of the Japan society for aeronautical and space sciences*, vol. 55, n. 644, pp. 439-445, 2007.
- [17] K. Yonemoto, K. Takato, H. Ochi and S. Fujie, «Kutta condition violation in two-dimensional NACA0012 airfoil at low Reynolds number» *26th AIAA Applied Aerodynamics Conference*, p. 6399, 2008.
- [18] C. Pranesh, M. Sivapragasam, M. D. Deshpande and H. K. Narahari, «Negative lift characteristics of NACA 0012 aerofoil at low Reynolds numbers,» *Sadhana*, vol. 44, n. 1, 2019.

- [19] H. A. Kutty and P. Rajendran, «3D CFD simulation and experimental validation of small APC slow flyer propeller blade» *Aerospace*, vol. 4, no. 1, 25 February 2017.
- [20] M. Atmaca, B. Cetin and E. Yilmaz, «CFD analysis of unmanned aerial vehicles(UAV) moving in flocks» *Acta Physica Polonica A*, vol. 135, no. 4, pp. 694-696, 2019.
- [21] S. Subhas, «CFD analysis of a propeller flow and cavitation» *International Journal of Computer applications*, vol. 55, pp. 26-33, 2012.
- [22] M. Stajuda, M. Karczewski, D. Obidowski and K. Jozwik, «Development of a CFD model for propeller simulation» *Mechanics and Mechanical engineering*, vol. 20, no. 4, pp. 579-593, 2016.
- [23] R. Franzke, S. Sebben, T. Bark, E. Willeson. and A. Broniewicz, «Evaluation of the multiple reference frame approach for the modeling of an axial cooling fan» *Energies MDPI*, vol. 12, no. 15, pp. 2934-2948, 2019.
- [24] J. G. Leishman, «Principles of helicopter aerodynamics», II edition, Cambridge Press, 2006.
- [25] L. Prandtl, «Applications of modern hydrodynamics to aeronautics» *Technical report no. 116 National Advisory Committee for Aeronautics (NACA)*, 1921.
- [26] R. Marpu, R. Sankar, T. Norman, T. Egolf and S. Makinen, «Analysis of the UH-60A Rotor Loads Using Wind Tunnel Data» *51st AIAA Aerospace Sciences Meeting including the New Horizons Forum and Aerospace Exposition*, n. 0635, p. 635, 2013.
- [27] C. Young, «The prediction of helicopter rotor hover performance using a prescribed wake analysis», Her Majesty's Stationery Office, London, 1976.
- [28] M. Drela and M. B. Giles, «Viscous-inviscid analysis of transonic and low reynolds number airfoils» *Journal of American Institute of Aeronautics and Astronautics (AIAA)*, vol. 25, n. 10, pp. 1347-1355, 1987.
- [29] M. Drela, «XFOIL: an analysis and design system for low Reynolds numbers airfoils» *Low Reynolds number aerodynamics*, pp. 1-12, 1989.
- [30] M. Lonoce, «Helicopter blade twist optimization in forward flight», Master thesis, IST Lisboa, 2016.
- [31] Ansys Inc., «Ansys Fluent user's guide», version 18.1, 2017.
- [32] J. Bardina, P. Huang and T. Coakley, «Turbulence modeling validation, testing and development» in *28th Fluid dynamics conference*, 1997.
- [33] F. R. Menter, «Turbulence modeling for engineering flows», Ansys, Inc. , 2011.
- [34] Ansys Inc., «Ansys Fluent theory guide», version 18.1, 2017.
- [35] P. R. H. A. Kutty, «3D CFD simulation and experimental validation of small APC slow flyer propeller blade» *Aerospace*, 25 February 2017.
- [36] M. Keating, «Accelerating CFD solutions, Ansys advantage» *advantage 1*, vol. 48, 2011.
- [37] I. S. Amado, «Experimental comparison of planar and coaxial rotor configurations in multi-rotors», Master thesis, IST Lisboa, 2017.
- [38] P. Chennakesava and Y. S. Navrayan, «Fused deposition modeling- insights» *Journal of International Conference on Advances in Design and Manufacturing (ICAD&M'14)*, vol. 14, pp. 1345-1350, 2014.
- [39] D. Garlotta, «Literature review of polylactic acyd» *Journal of polymers and the environment*, vol. 9, n. 2, pp. 63-84, 2001.

- [40] T. Prater, Q. Bean, R. Beshears, T. Rolin, N. Werkheiser, E. Ordonez, R. Ryan and F. L. III, «Summary report on phase I results from the 3D printing in zero-G technology demonstration mission, Volume I» National Aeronautics and Space Administration (NASA), Huntsville, Alabama, 2016.
- [41] Engineers Edge, [Online]. Available: https://www.engineersedge.com/3D_Printing/abs_plastic_filament_engineering_information_14211.html. [Last visit 20 04 2020].
- [42] L. Zengguang, W. Yanqing, W. Beicheng, C. Chunzhi, G. Yu and Y. Cheng, «A critical review of fused deposition modeling 3D printing technology in manufacturing polylactic acid parts» *The International Journal of Advanced Manufacturing Technology*, n. 102, pp. 2877-2889, 2019.
- [43] J. Yang, Z. Zhao and S. Park, «Evaluation of directional mechanical properties of 3D printed polymer parts» *International conference on Control IEEE*, pp. 1952-1954, 2015.
- [44] M. Afrose, S. Masood, P. Iovenitti, M. Nikzad and I. Sbarski, «Effects of part build orientations on fatigue behavior of FDM-processed PLA material» *Prog Addit Manuf*, vol. 1, n. 1-2, pp. 21-28, 2015.
- [45] U. BV, «Ultimaker» [Online]. Available: <https://ultimaker.com/it/3d-printers/>. [Last visit 28 04 2020].
- [46] J. Prusa, «3D printing handbook user manual for 3D printers: original Prusa SL1», Prusa Research s.r.o., 2019.
- [47] Z. Zguris, «How Mechanical Properties of Stereolithography 3D Prints Are Affected by UV Curing», Somerville, MA: Formlabs Inc., 2016.
- [48] Y. Lee, S. Lee, X. G. Zhao, D. Lee, T. Kim, H. Jung and N. Kim, «Impact of UV curing process on mechanical properties and dimensional accuracies of digital light processing 3D printed objects» *Formlabs white paper*, vol. 22, n. 2, pp. 161-166, 2018.
- [49] «Scapa industrial» [Online]. Available: <https://www.scapaindustrial.com/products/product-details/GenerateTDS/4403/EN/>. [Last visit 28 05 2020].
- [50] D. Sofialidis, «Express introductory training in Ansys Fluent, Lecture 2, Boundary conditions & solver settings. Prace autumn school» 2013.
- [51] «Ansys Student Community» [Online]. Available: <https://studentcommunity.ansys.com/thread/neat-wall-treatment/>. [Last visit 21 04 2020].
- [52] «Masconomet» [Online]. Available: <https://www.masconometdigitalphotography.com/elements-of-exposure-poster.html>. [Last visit 12 04 2020].
- [53] S. Korukonda, T. Sanduga and S. Benedict, «Numerical study of laminar separation flow over a low Reynolds number airfoil», 3rd International Conference ICRAMAV, pp. 181-184, 2014

A Annex

A.1 3D printing

This chapter will deal with the 3D printing procedure that was tested for the present work. At first, a description of the main 3D printing methodologies is made, with particular emphasis on the parameters influencing the quality of the print. Then, the machines present in the laboratory are described, and finally the results of different print tests are presented.

The rapid prototyping (RP) can be defined as the group of different procedures which scope is the fabrication of a scale model starting from CAD data [38]. The importance of fast and accurate production methods, in order to maximize profits and staying competitive in the market, led to the development, around the 1980s, of a particular technology that can go under the name of additive manufacturing (AD). It is based on a different and innovative concept with respect to the traditional fabrication procedures: unlike the technique of removing material from raw pieces, the procedure of creating a new part with AD is based on “adding material”. There are different ways of “adding material”, and in the Product Development laboratory of IST there are machines which are based on two very different but equally interesting concepts, the Fused Deposition Modeling (FDM), and the Stereolithography (SLA). In this way, it is possible to compare the same rotors printed with these two techniques, evaluating their differences, and choosing which one is the best for the aim of testing sub-scale propellers at relatively high rotational speeds.

A.1.1 Fused Deposition Modeling

The Fused Deposition Modeling technique was invented in the end of the 1980s by S. Scott Crump, and it was made available in commerce in 1990 by Stratasys [39]. Among all the additive manufacturing techniques, it is interesting because of its low cost in use and maintenance: in fact, it does not require laser, and the extruded materials are low-melting point polymers such as polylactic acid (PLA), acrylonitrile butadiene styrene (ABS), polycarbonate (PC) and polyamide (PA). The possibility of feeding the header with different materials, being extruded by different nozzles, permits the printing of multi-material pieces. This is particularly interesting especially in the case in which the support material can be printed in a soluble substance, so that the procedure of its separation from the designed part is easier.

Since the beginning of its life, FDM found success in different engineering fields such as mechanics, microelectronics, computer technology and aerospace. For example, it is worth noting that in 2014

NASA sent an FDM printer to the International Space Station, for the creation of pieces needed for maintenance and repair [40]. All the materials mentioned above are thermoplastics: when heated, they become malleable, so that they could be extruded in a nozzle. The generic process followed by an FDM

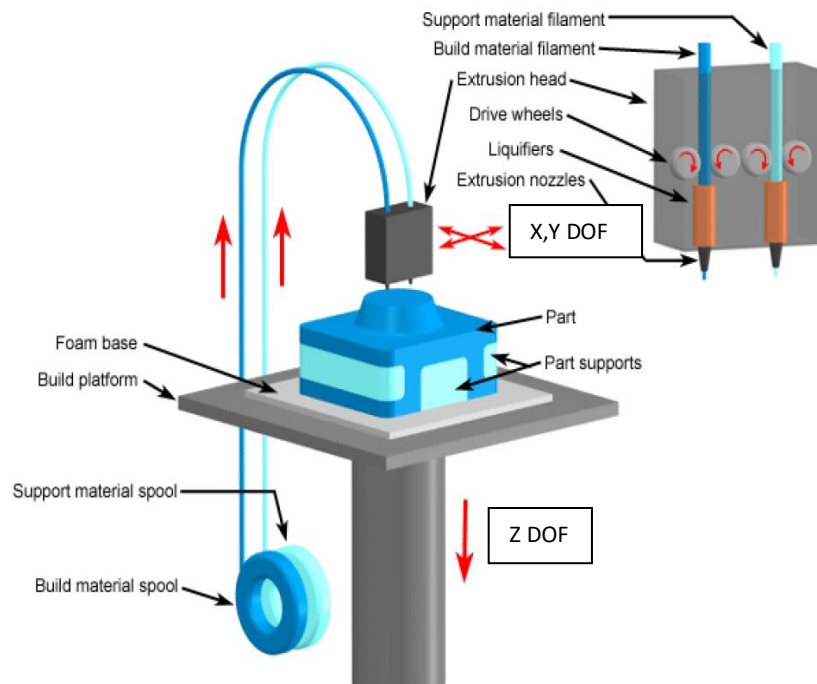


Figure A.1: FDM printing procedure, adapted from [38]

machine is as follows. A filament of thermoplastic material is led to the extruder. When arrived at the extruder, which uses a torque and a pinch system in order to feed and retract the filament of precise amounts, the filament is heated up to a certain characteristic temperature at which it melts. The temperature depends on the material chosen for the print. The heated material is forced to pass through a nozzle of small diameter, and then it is led down on the plate where needed. Usually the extruder can move freely, with X, Y degrees of freedom, while the Z degree of freedom is controlled by the height of the building plate (see figure A.1). The building plate is heated to permit the adhesion of material on it. However, it is possible to develop printers with a different system of degrees of freedom, like with control of radial and azimuthal coordinates.

A.1.2 Materials

Different materials are available for the FDM technique. Two of the most widely used materials are ABS and PLA.

ABS is a low-cost thermoplastic, used in many different engineering fields for being a good tradeoff between price and qualities. It is ideal in applications in which impact resistance, strength and stiffness are required [41]. Usually, more than 50% of ABS is made by Styrene, which provides rigidity and easy processability. Different amounts of Acrylonitrile (which guaranties chemical resistance and heat stability) and Butadiene (to improve toughness and impact strength, as well as ductility) are possible, in order to enhance the required qualities. Weaknesses of ABS are the high flammability values and poor resistance to UV outdoor light.

Two different procedures are possible for the realization of ABS: the first is the mechanical blending of individual components; the second is the polymerization of a mixture of Styrene with Acrylonitrile in the presence of the rubber component. It is possible to choose between three kind of polymerization: emulsion, suspension, and bulk, with the first that is the most used. As previously said, the overall toughness is the first good characteristic of this material. Moreover, with respect to other polymers, ABS is less sensitive to notch; these characteristics are valid in a huge interval of temperatures, making ABS good also for low-temperature applications. Also, its ductility is maintained for different temperatures.

For the FDM applications, the diameter of ABS filament can be of 1.75 mm or 2.85 mm and the nozzle can have a temperature between 220° and 245°, with this one recommended. The suggested temperature of the building plate is around 95° [41].

PLA belongs to the family of aliphatic polyesters, which are biodegradable and compostable compounds [39]. It is a relatively old material, because the lactic acid, from which it derives, was isolated in 1780 by the Swedish chemist Scheele and it was commercialized around 1881. It can be produced from annually renewable resources, and this aspect contributed to its spread in the 3D printing world, being used in many medical applications, as well as support material in tissue engineering. Its degradation to form H₂O and CO₂ happens through hydrolisis, without the need of any catalyzer for the process. With respect to ABS, PLA has lower mechanical strength, because its molecular chain structure is simply linear, and the molecular diffusion which causes the bonding between different layers during the 3D printing process

Property	ABS (Acrylonitrile Butadiene Styrene)	PLA (Polylactic Acid)
Density ρ (Mg/m ³)	1.00 - 1.22	1.24
Young's Modulus E (GPa)	1.12 - 2.87	3.53
Elongation at break (%)	3 - 75	6.05
Melting (softening) Temperature (°C)	88 - 128	159
Glass Transition Temperature (°C)	100	60
Yield Stress σ_y (MPa)	18.5 - 51	-
Tensile Strength σ_{ts} (MPa)	25 - 50	36 - 55
Ultimate Tensile Strength (MPa)	33 - 110	35
Fracture Toughness (Plane strain) (MPa√m)	1.19 - 4.3	-
Thermal expansion (μm/mK)	83 - 95	-
Strength to weight ratio (kNm/ kg)	31 - 80	40
Shear modulus (GPa)	3180-	24

Figure A.2: Resume of ABS and PLA characteristics. From [41]

is limited. It is worth noting that its molecular shape contains many holes that could be filled with particular materials, in order to increase the mechanical properties: metals like Copper are preferred as reinforce materials instead of Iron and steel, because of their spherical morphology, thanks to which they can diffuse in good part of the PLA material matrix.

A.1.3 Parameters influencing printing

A piece produced with FDM techniques must ensure a certain strength, and a surface quality which can be controlled by selecting the proper value for different parameters.

The nozzle and build platform temperatures depends on the material chosen (for example, the PLA optimal nozzle temperature is 150°, while for ABS is between 220° and 245°), and affects the mechanical characteristics of the final product. Many studies were made in order to understand what the best temperature is to guarantee a good bonding. Various approaches are described in [42]. Their values are strongly linked with the bonding quality between successive layers, as well as with the development of internal loads. The molten thermoplastic is extruded and pressed against the previous layers: due to the high temperature and pressure, the previous layer re-melts, enabling bonding between the two layers. This bonding is due to the molecular diffusion, a process that happens at the melting point temperature: in the printing process the temperature drops due to the impact of external environment, and the limited volume of material which is melting. These facts can stop the molecular diffusion, thus forbidding the complete formation of bonds. For this reason, the mechanical properties of a 3D-printed piece change when considering different directions: in particular, they are discontinuous between fuses in the Y direction, and in the gradually accumulating Z direction, supposing X as the printing direction, and this fact is more evident for PLA than ABS, due to the different molecular structure.

The external environment temperature variation changes the rate of cooling in different regions of the printed part, contributing to the storing of stresses in the structure, with consequent formation of warping, undesired deformation, and lowering of mechanical properties. Too slow cooling causes disorder of fused PLA filaments, bad surface quality, and possibility of deformation during the printing; instead too fast cooling implies a poor molecular diffusion, and so poor mechanical properties. ABS is usually more sensible to warping than PLA.

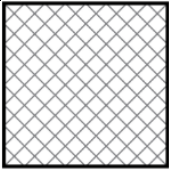
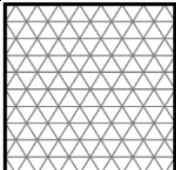

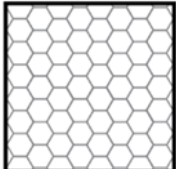
A direct consequence of these themes is that the strength of parts is affected by printing directions. The fuse direction should be aligned with the maximum structural load direction [43]. Afrose and others [44] studied x-oriented, y-oriented, and 45°-oriented parts, finding out that the last had the best fatigue property. There is not a perfect rule in defining the best printing direction: it must be chosen case by case. If possible, it is good to try the different options, and test them experimentally.

A.1.4 Shell and infills

Often FDM parts are not printed solid for reason that start from the printing time and end in the need of saving material. In these cases, the outer perimeter is traced with several passes, creating the shell, while the interior is filled with an internal low-density structure (infill). Shells and infills influence the strength of a part. The shell is the first thing to be printed; an increasing in its thickness leads to a growth in the strength of the material, and it is necessary if the part will be subjected to post-processing methods

that would reduce the thickness of the model; on the counterside, increasing its width causes a longer production time. It is a good practice to design shells being a multiple of the nozzle diameter, to prevent void formation.

Table 11: Different infill tipologies

<p>RECTANGULAR</p> <p>Strength in all directions</p> <p>Fast to print</p>		<p>TRIANGULAR/DIAGONAL</p> <p>Strength in wall directions</p> <p>Longer to print than rectangular</p>	
<p>WIGGLE</p> <p>Not stiff for twisting/compressive loads</p>		<p>HONEYCOMB</p> <p>Strength in all directions</p>	

Different infill typologies are available, the choice depending on the type of loads the printed part will have to withstand. In the case of this study, it was chosen to fill the entire blade section, not considering the effect of different infill geometries, because of its small dimension.

A.1.5 Support material

The presence of a support material is mandatory for many applications: it creates the best basis on which the real part can be printed, and it is fundamental especially for models which have overhanging parts. It is possible to have supports made of the same material as the piece to be printed, and in the case of multi-nozzle machines it is possible to print in a different material, to ease the process of removing the support and having the part of interest. If this last option is chosen, careful attention of the support material must be made, making sure that it does not react with the other material. A well-known support material that can be used with PLA is polyvinyl alcohol (PVA), which is soluble in water: this makes the post-printing curing easier.

A.1.6 Printing procedure

The machines used for testing the FDM printing where the Ultimaker S3, the Ultimaker S5, and the Ideamaker. The S3 printer presents a 230 x 190 x 200 mm printing volume, with a minimum layer height of 20 μ m, and a nozzle size of 0.4 mm. It can work with many materials such as PLA, BS, nylon. The S5 presents a greater printing volume of 330 x 240 x 300 mm, and the same characteristics for the

minimum layer height and nozzle size. Detailed characteristics about these printers can be found in [45]. The software suggested for the implementation of the model to be printed is the open source Ultimaker Cura. The Ideamaker printer has a 305 x 305 x 300 mm printing volume and a minimum layer height of 10 μm , and it can work with a variety of filaments up to 300°C. The slicer software to be used is developed by the same brand, Ideamaker.

The CAD model prepared for the CFD simulations is saved in the .stl format, and it is sent to the slicer software, where it is possible to set up the printing characteristics. In fact, the positioning of the parts on the printing plate is made, as well as the definition of the material to be used. In this way, the software automatically defines the temperatures needed for the nozzle and the building plate. Moreover, the characteristics of the support material, and the advanced printing features can be specified. The user can in fact modify the printing quality by choosing the layer height, the line width for both the outer wall and the infill and so on. It is also possible to select the number of lines composing the shell, as well as selecting the infill pattern and its characteristics in term of infill density. It is possible to choose if to insert the support material everywhere or only in the points in which the model touches the building plate, as well as choosing the overhang angle which needs the presence of support.

Like the main part, also the support presents an infill which geometry has to be properly chosen. In fact, a too dense support may cause difficult in its separation from the printed part; on the opposite, a too weak support may fail during the process, thus damaging the printing. Finally, it is suggested to create a build plate adhesion with the main material, and not the support material, to ease the removing of the piece once the procedure is done. There is no an overall correct setup, but the parameters for the best print should be calibrated case by case after several tests. Once the settings are completed, it is possible to create the slicing, and to preview the paths followed by the header to complete the print. At this point it is often useful to check how support and infills are realized and change their characteristics if needed. The file is then saved in the format .3mf and is ready to be sent to the printer.

A.1.7 Printing tests

A first test is realized with the S3 printer, to check how the body orientation on the building plate affects results, particularly in term of surface quality. In fact, it is important to have smooth surfaces to not

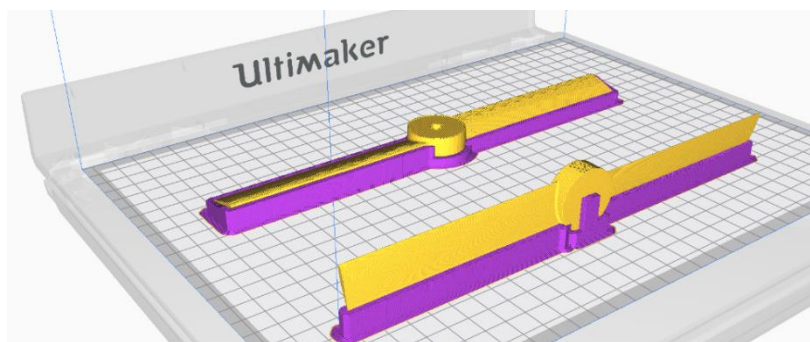


Figure A.3: Positioning the SB rotor for the FDM printing

enhance the skin friction drag of the rotor. The PLA is chosen for both the support and the object, and the best quality available is assessed by imposing an extra fine thickness for the extruded material, equal to 0.06 mm. For the rotor orientation in which the rotor plane is parallel to the building plate (method 1), a rectangular infill support material is chosen, with a density equal to 60%. For the other rotor (method 2), the support is made by a very thin wall, supporting the LE of a blade, and the TE of the other (see figure A.3).

The obtained results are particularly interesting. In fact, for the case 1, the procedure of support removal is difficult, and the interface between the rotor and the support presented some defects which need a post-processing curing (see figure A.4). The upper rotor part presents a surface quality that should be sand papered to increase its smoothness. The sandpapering of this rotor is difficult, since it could modify the airfoil shape.



Figure A.4: Particular of the surface quality after the support removal for the case 1

The overall surface quality of case 2 is higher, however a small defect is found, due to the vibration of the building plate. In fact, looking at the blade which has the TE in contact with the support material, it is possible to see the vibration effect on the airfoil shape, which turns out to be non-symmetric (see figure A.5). The other blade, with the LE in contact with the support does not show this problem, keeping an elevated surface quality. The problems deriving from the vibrations, already present in the straight blade, would have been increased with the presence of curvature, since the tip of the blade would be at a greater distance from the building blade, thus requiring a higher support structure.



Figure A.5: Airfoil shape for case 2. It is noticeable the effect of vibrations in the airfoil shape.

These considerations led to the definition of an alternative printing method (method 3). It is chosen to print the support in the soluble material PVA, and to divide the blade in two part, in order to ensure that the LE is always facing the support, to reduce the vibrational problems. This printing series is realized with the S5 printer. The path followed for the support is concentric lines, while the infill density is kept to 60%. Since two materials are used during this process, both nozzles are fed with the proper material, and for every layer the machine must change the nozzle activated. The tests are made with the single curved blade, in order to check how the curved tip is treated.



Figure A.6: Single curved blade printed with method 2. On the right, particular of the tip profile

The results shown in figure A.6 are good in term of accuracy in the LE and TE representation, as well as in the surface smoothness on both blade sides. This last characteristic is enhanced by means of two post-processing passages: at first, the sandpapering with an extra fine paper (1000 grit) is realized; then, plastic wax is applied, to fill the microscopical void between lines of PLA, and to recover some thickness that is inevitably lost during the sandpapering. Some defects are found in the definition of the curved LE, due to the difficulty of sandpapering that part, and in the TE near the tip region, in which some vibrational effects are noticed.

An ulterior test is realized with the Ideamaker printer, printing the blade vertically (method 4). This orientation would improve the surface quality, but questions arise on the vibrational effects, since the outer part of the blade is located far from the building plate (around 120 mm). The blade typology chosen for this test is the total curved TE2B. The printed piece shows a very good LE representation and a good surface quality, better than the previous before any post-processing operation. However, the TE is thinner than the other models and a small irregular step is present on both sides (see figure A.7). Conclusively, the method 3 seems to be the best for the 3D printing of these blade models using the FDM technique, comparing the surface quality, and the possibility of limiting the effects of vibrational loads. In term of production time, a rotor composed by two blades could be printed in about 13 hours.



Figure A.7: Blade printed with Ideamaker (left), and particular of the blade tip (right). The presence of a small step near the TE all along the blade is noticeable

A.1.8 SLA

In 1986 Chuck Hull developed the technology for printing objects through the SLA method, with the first apparatus realized in 1992. This technique is different in the concept from the FDM. In fact, it is based on the property that a specific liquid resin can solidify when put in contact with an ultraviolet (UV) laser source. Most of the common SLA 3D printers are composed of the following parts:

- resin tank, which contains the photosensitive resin
- movable build platform, on which the first solid layers can attach. The platform can move up and down during the printing process

- UV laser source
- Laser addressing system, which has the function of selecting the regions in which the laser goes in contact with the resin for the solidification. Different possibilities are available, like a mirroring system, or an LCD screen, which display a mask with the shape of the layer being processed. In this way, the UV source will shine through the mask solidifying only the desired regions.

The printer used in this study is the Prusa SL1, which characteristics are available in [46]: it works with an upside-down technology, so that the laser is directed upwards to the resin tank which presents a transparent basement. The main difference between materials available for the FDM printing and the SLA printing is the variability. In fact, when printing with FDM technology, it is possible to choose the material between different possibilities like PLA, PVA, ABS, nylon, and so on. Instead, when printing with SLA, the only material available is the resin. The three main resin components are the core, the photo initiators, which is responsible of the starting of the solidifying process, and some additives which aim to change the resin mechanical properties, as well as the color. The Prusa SL1 machine works with liquid resins sensible to 405 nm UV light source.

A.1.9 Printing process

The printing process starts from the CAD file that must be saved in the .stl format. The successive step is opening the file with a slicer software. Prusa developed its own slicer Prusaslicer, which properly interacts with the machine, so this is used for the work. In the slicer software, it is possible to set up the main characteristics of the printing, starting from the quality. The SL1 printer offers four different quality levels, based on the width of each layer. The fastest but less precise condition is imposing a layer height

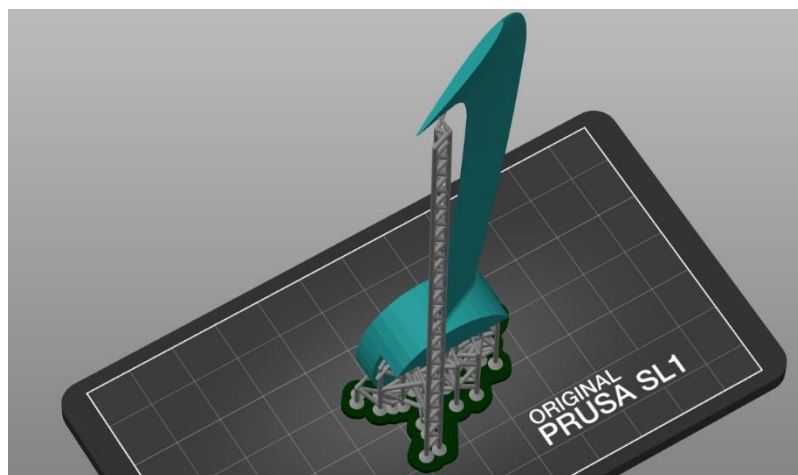


Figure A.8: Example of Prusa slicer display. In this case the blade is the total curved TE2 with presence of twisting. The program automatically builds a support for the tip of the blade.

of 0.1 mm, the finer is 0.025 mm. The other two possibilities are 0.035 mm and 0.05 mm. It is also possible to select the resin to be used, among a list of Prusa resins. Based on the selection, the program defines the exposure time needed for the solidification of the resin. Another setup to be made is the definition of the support material: it is possible to choose if the support should be present only on the building plate, or everywhere, as well as to define its density. Improving the support density could

prevent the object deformation during the printing process, helping to obtain the desired result (see figures A.9 for an example of support material at the blade hub). The printing session could be damaged by the breaking of the supports, so care must be addressed in their design. The user can choose the position of the contact points between the support and the printed part by activating the support manual editing.

When the project is defined, it must be saved in the format .3mf, to be then sent to the printer. As the printing process starts, the laser operates solidifying the first resin layer where needed. After the solidification time, which is a function of the material selected, the building plate moves upwards, so that new liquid resin enters in contact with the laser source and solidifies. This process continues till the entire part is completed; at this point, the platform is elevated above the tank so that the excess resin is drained.



Figure A.9: Example of support material at the blade root

When working with the SLA technology, the post-printing phase becomes crucial to enhance the printed objects properties [47]. The first step is washing the part in isopropyl alcohol (IPA), for several minutes. Keeping the object in contact with IPA for an extended period of time may lead to failure of the part. The second step is the drying, to ensure that all the IPA is removed from the surface. Finally, there is the curing of the object, putting it in contact with a UV light source. This source could be the Sun (in which case the object should be kept for an extended period of time (24-48 hours)). This time drastically reduces when using a proper machine. In the laboratory, the Prusa Curing and Washing Machine CW1 is used for completing the three post-processing phases in 10 minutes. The washing of the part is guaranteed by a magnetic propeller who has the function of diffusing the IPA to every part of the model. After the drying, the curing is realized with four UV light sources operating at a wavelength of 405 nm. The utility of post-processing curing is confirmed in [47] and [48] where the improvements on mechanical properties such as the ultimate tensile strength and the Young modulus is experimentally confirmed.

The printing of the SCB rotor blades as a sample model brings to brilliant results in term of surface smoothness. Without any kind of refinement, its quality is at the level of the sandpapered FDM-printed blades. Moreover, small details like the TE or the tip shape are represented better than with FDM. However, for the nature of the printing process itself, the blade surfaces in contact with the support material are not flat, but present an irregular shape. The same feature is noticeable also in the other hub surfaces, thus the sandpapering with a 1000- grit paper is realized to smooth them. Another concern regards the mechanical characteristics, since the blades appeared to be very flexible. From an aerodynamic point of view this fact could develop a modification in the pitch angle, and so in the aerodynamic angle of attack, thus influencing the overall rotor performances. In absence of data

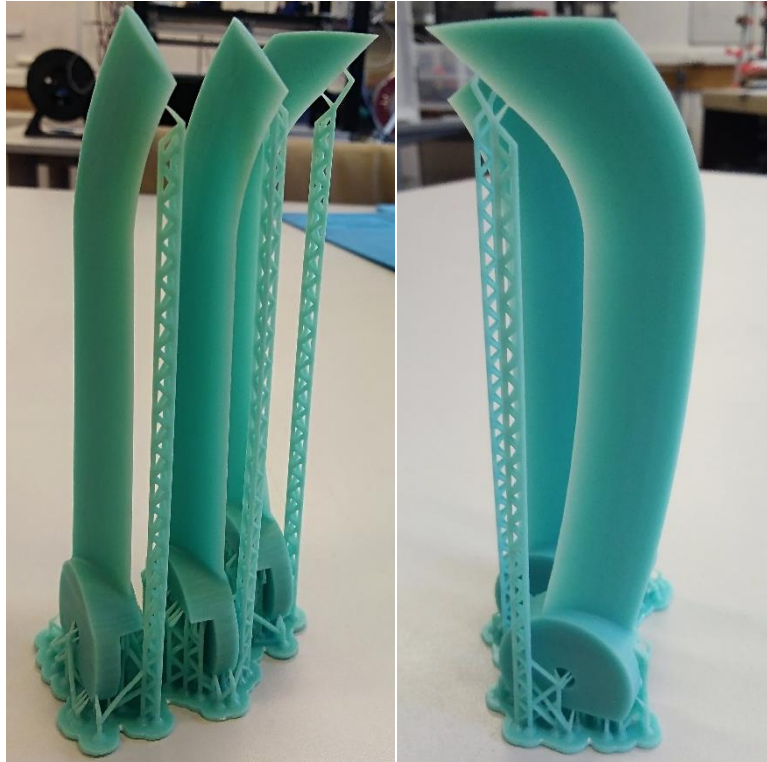


Figure A.10: Total curved blades TE1, TE2 printed with the SLA technology. The presence of the support material contributed to obtain the desired geometry.

available about the mechanical strength of the part, a first test is made by putting the SCB rotor in rotation at 3000 RPM. Since there is no evidence of a blade damaging under these loads, it is assumed that the blade is enough stiff to withstand the loads acting on it for the time required in a test.

Another positive aspect of SLA printing is the possibility of printing many objects during the same session without increasing the printing time. In the current case, up to 6 blades could be printed at the same time, and this is a great advantage with respect to the FDM technique. In fact, assuming a good quality for the FDM printing, that is with a layer thickness of 0.06 mm, a single blade is printed in about 6 hours. With the SLA technology, six blades can be printed in about 10 hours, thus greatly reducing the overall printing time. In table 12, the rotors printed with the SLA technology are presented.

Table 12: Rotors printed with the SLA technology

Rotor	Root pitch angle	Rotor	Root pitch angle
SB	15°	TE1B	15°
SB twisted	22.5°	TE1B twisted	22.5°
SCB	15°	TE2B	15°
SCB twisted	22.5°	TE2B twisted	22.5°

A.1.10 Union of the printed blades

The printed blades must be attached together in order to ensure a good alineament, that is fundamental for comparing the experimental results with the CFD simulations. The SLA-printed blades present some defects which can hinder the procedure of alineament, as explained in section A.1.9. After the sandpapering of the irregular surfaces, the blades are attached together by a 0.24 mm thickness SCAPA 4403 tape, with an operative temperature range between -30° and 70°, and suitable for rough surfaces [49]. Its reduced thickness do not influence eccessively the hub height; moreover, with respect to cyanacrylate glues, the longer bonding time permits to adjust the relative position between the two blades after the contact.

Even though the gluing procedure has been realized with care, is is noticed how the blades are not perfectly aligned. This is caused by the printing process, which generates a distortion in the blade shape. This distortion is more evident in the case of blade characterized by curvature, namely the SCB, TE1B and TE2B rotors blades. This not perfect alignment is predicted to alterate in some way the experimental results, and to introduce vibrations in the system.

A.2 Experimental tests

The test bench developed by Ines is used for testing the printed rotors [37]. It is based on an Aluminium arm in which 3 Wheatstone bridges made by straining gauges are present in order to detect the forces directed along x and y directions F_x, F_y as well as the torque around the x axis M_x . Moreover it is dotated of a RPM sensor to measure the rotational velocity, and of a temperature sensor to measure the motor temperature. The strain gauges calibration is realized following the Ines approach by applying three times 154 loads conditions with the help of known weights and pulleys. Both the positive and negative x and y directions are calibrated. A Matlab code has been then developed in order to obtain the coefficients which links the bridge readings with the actual measures of F_x, F_y and M_x , according to the relation expressed in equations A.1, A.2, A.3.

$$F_x = c_{1,1}R_1 + c_{2,1}R_2 + c_{3,1}R_3 \quad (\text{A.1})$$

$$F_y = c_{1,2}R_1 + c_{2,2}R_2 + c_{3,2}R_3 \quad (\text{A.2})$$

$$M_x = c_{1,3}R_1 + c_{2,3}R_2 + c_{3,3}R_3 \quad (\text{A.3})$$

It is noticed how in this case F_x is the thrust generated by the rotor in hovering condition, while M_x represents the torque required to put the rotor in rotation. Multiplying the value of M_x for the angular speed it is possible to find the power required to hover, and finally the rotor FM, through equation 2.14.

A.2.1 Experimental results

The first experimental test made is done with the SB rotor having a 15° pitch angle. The SLA-printed rotor is put in rotation at different rotational speeds to detect how thrust and power vary with it. In particular, the rotational speeds tested cover a range between 1990 RPM and 5043 RPM.

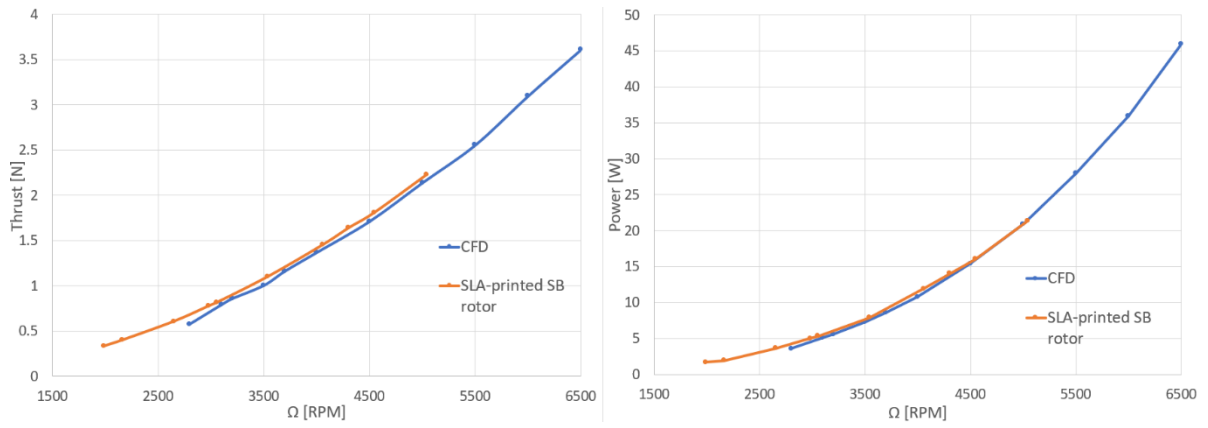


Figure A.12: Thrust and Power behavior versus rotational speed. Comparison between experimental data and CFD simulations for the SB rotor with 15° root pitch angle

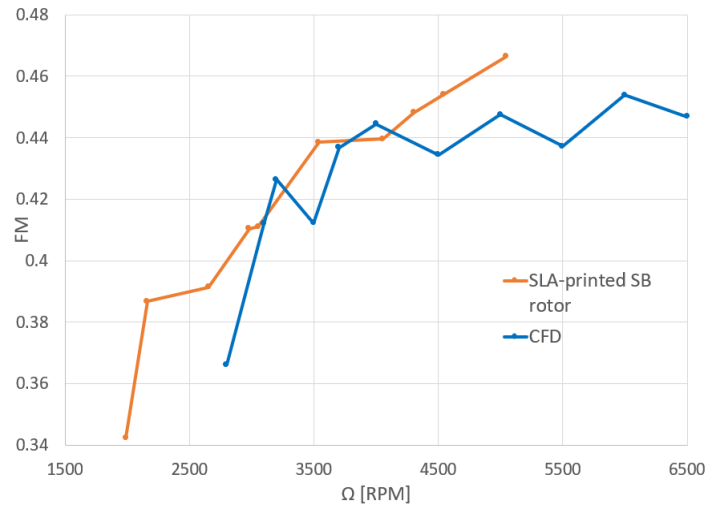


Figure A.11: FM behavior versus rotational speed. Comparison between experimental data and CFD simulations for the SB rotor with 15° root pitch angle

The comparison with results from CFD simulations shows good accordance both for the thrust and the power (see figure A.11 a-b). In particular, the thrust measured by experiment is always higher than the one predicted by the CFD analysis: a cause for this behavior could be the flexibility of the blade, that could generate an actual angle of attack different from the one predicted by computational means. The FM presents similar values, with differences that are below the 5%, see figure A.12.

The second experimental test campaign is realized by putting in rotation the different rotors at 3000 RPM, verifying whether the results are in good accordance with the CFD data.

- SB rotor

The straight bladed rotor tested presents a thrust production of 0.786 N, that is 6.5% higher than the CFD predicted data, while the power is 5.08 W, 9.51% higher than CFD results. This leads to a FM of 0.4105, which is very similar to the 0.409 value found from the CFD (difference around 0.4%). When passing from the SB untwisted rotor to the SB twisted rotor, with a root pitch angle of 22.5°, the CFD result is 0.779 N thrust, while the experiments present a 9% higher thrust of 0.849 N. In this case the power consumption is equal to 5.4 W, 18% lower than the CFD case, so that in term of performance the experimental FM is 3.8% lower than the CFD-predicted.

- SCB rotor

The experimental results for the SCB untwisted rotor with a root pitch angle of 15° are in great accordance with CFD simulations. In fact, the discrepancies for thrust, power and FM are below 2%, with the CFD simulations that slightly overpredicts the rotor FM. When analyzing the twisted case, the differences become more evident, since the thrust is found to be equal to 0.80 N, 16.5% greater than the thrust predicted with the CFD; also the power is found to be 28.5% greater than the simulations. In general, when comparing the FM, the discrepancy is reduced to 1.8%. By analyzing these results, it seems that the operative pitch angle for the blade tested is greater than 15°: this would explain the higher amounts of thrust produced and power required to rotate. This is possible due to the flexibility of the SLA-printed rotor.

- TE1B rotor

In the case of the TE1B rotor, the experiment underpredicts the thrust and power values of about 4.5% with respect to the simulations, while the FM is 2.47% lower. When considering the twisted TE1B rotor, as found also in the SCB case, the experiments presents higher values for thrust, power and FM.

- TE2B rotor

In the case of untwisted blades, the thrust experimentally found is 8.7% higher than the CFD case, and the power is 4.6% higher. This causes the experimental FM value to be equal to 0.444, 8.26% higher than the CFD case. When considering the twisted TE2B rotor the thrust results 5% higher and the power similar, the difference being 0.8%, so that the FM gains a 8.6% increase.

Table 13 resumes all the considerations above made, presenting the actual values of thrust, power and FM with relative discrepancies.

Table 13: Comparison between CFD and experimental results for SB rotor

Rotor	Experimental Thrust	CFD thrust	ΔThrust	Experimental FM	CFD FM	Δ FM
SB 15°	0.786 N	0.738 N	6.5%	0.410	0.409	0.4%
SB twisted 22.5°	0.849 N	0.779 N	9%	0.434	0.451	3.8%
SCB 15°	0.695 N	0.696 N	0.16%	0.385	0.393	1.95%
SCB twisted 22.5°	0.802 N	0.688 N	16.55%	0.387	0.394	1.82%
TE1B 15°	0.702 N	0.737 N	4.8%	0.387	0.397	2.47%
TE1B 22.5°	0.767 N	0.741 N	3.47%	0.414	0.402	2.84%
TE2B 15°	0.849 N	0.780 N	8.78%	0.444	0.410	8.26%
TE2B 22.5°	0.853 N	0.812 N	5.08%	0.455	0.419	8.62%

In most cases, the thrust production found with the CFD simulations underpredicts the values registered during the tests. This fact could be due to the flexibility of the rotors printed in resin, which may cause the blade to vibrate during rotation thus not operating at a constant pitch angle. Moreover, difficulty is found in aligning the rotors in the plane perpendicular to the rotational axis, due to the non-flat surfaces of the rotor hub. The misalignment produced vibrational loads during the tests which may have affected the results. From these considerations it is apparent how the SLA technology, although producing blades with elevated surface quality, should be linked with a stiff structure to avoid the blade deformation during the operational time.

Another consideration that comes from the analysis of the experimental results is the goodness of TE2B rotor, which appear very performant at 3000 RPM, both in its untwisted and twisted configurations, overcoming the performances of the SB rotor.

A.3 CFD extended results

Table 14: Backward curvature – untwisted case - hovering conditions

Untwisted case	θ_0	Ω [RPM]	Thrust [N]	Power [W]	Torque [Nm]	FM
SB rotor	15°	3000	0.738	4.639	0.015	0.409
	17°	3000	0.872	5.549	0.018	0.439
	19°	3000	0.974	6.577	0.021	0.438
	21°	3000	1.093	7.851	0.025	0.435
	25°	3000	1.313	11.364	0.036	0.396
SCB rotor	15°	3000	0.696	4.426	0.014	0.393
	17°	3000	0.817	5.336	0.017	0.414
	19°	3000	0.917	6.267	0.020	0.419
	21°	3000	1.009	7.370	0.023	0.412
	25°	3000	1.255	10.798	0.034	0.390
TE1B rotor	15°	3000	0.737	4.778	0.015	0.397
	17°	3000	0.803	5.387	0.017	0.400
	19°	3000	0.918	6.404	0.020	0.411
	21°	3000	1.023	7.567	0.024	0.409
	25°	3000	1.241	10.799	0.034	0.383
TE2B rotor	15°	3000	0.780	5.028	0.016	0.410
	17°	3000	0.933	6.312	0.020	0.427
	19°	3000	1.064	7.772	0.025	0.423
	21°	3000	1.232	9.749	0.031	0.420
	25°	3000	1.533	15.009	0.048	0.378

Table 15: Backward curvature - twisted case - hovering conditions

Twisted case		Ω [RPM]	Thrust [N]	Power [W]	Torque [Nm]	FM
SB rotor	22.5°	3000	0.779	4.564	0.015	0.451
	24.5°	3000	0.906	5.605	0.018	0.461
	26.5°	3000	1.017	6.662	0.021	0.461
	28.5°	3000	1.107	7.751	0.025	0.450
	32.5°	3000	1.318	10.940	0.035	0.414
SCB rotor	22.5°	3000	0.688	4.333	0.014	0.394
	24.5°	3000	0.830	5.271	0.017	0.429
	26.5°	3000	0.929	6.185	0.020	0.433
	28.5°	3000	1.031	7.321	0.023	0.428
	32.5°	3000	1.223	10.471	0.033	0.387
TE1B rotor	22.5°	3000	0.741	4.746	0.015	0.402
	24.5°	3000	0.841	5.599	0.018	0.412
	26.5°	3000	0.939	6.622	0.021	0.412
	28.5°	3000	1.060	7.772	0.025	0.420
	32.5°	3000	1.258	11.075	0.035	0.381
Te2B rotor	22.5°	3000	0.812	5.227	0.017	0.419
	24.5°	3000	0.950	6.374	0.020	0.435
	26.5°	3000	1.119	8.066	0.026	0.439
	28.5°	3000	1.244	9.850	0.031	0.421

Table 16: Forward curvature - untwisted case - hovering conditions

Untwisted case	θ_0	Ω [RPM]	Thrust [N]	Power [W]	Torque [Nm]	FM
SCF rotor	15°	3000	0.708	4.922	0.016	0.362
	17°	3000	0.824	5.962	0.019	0.376
	19°	3000	0.924	7.017	0.022	0.379
	21°	3000	1.036	8.327	0.027	0.379
	25°	3000	1.182	11.451	0.036	0.336
TE1F rotor	15°	3000	0.673	5.169	0.016	0.320
	17°	3000	0.753	6.042	0.019	0.324
	19°	3000	0.856	7.152	0.023	0.331
	21°	3000	0.952	8.418	0.027	0.330
	25°	3000	1.129	11.375	0.036	0.315
TE2F rotor	15°	3000	0.751	4.744	0.015	0.410
	17°	3000	0.874	5.815	0.019	0.421
	19°	3000	0.983	7.103	0.023	0.411
	21°	3000	1.085	8.760	0.028	0.386
	25°	3000	1.298	12.586	0.040	0.351

Table 17: Forward curvature - twisted case - hovering conditions

Twisted case	θ_0	Ω [RPM]	Thrust [N]	Power [W]	Torque [Nm]	FM
SCF rotor	22.5°	3000	0.683	4.501	0.014	0.375
	24.5°	3000	0.806	5.535	0.018	0.391
	26.5°	3000	0.929	6.641	0.021	0.403
	28.5°	3000	1.032	7.788	0.025	0.403
	32.5°	3000	1.214	10.645	0.034	0.376
TE1F rotor	22.5°	3000	0.694	5.184	0.017	0.334
	24.5°	3000	0.802	6.180	0.020	0.348
	26.5°	3000	0.920	7.372	0.023	0.358
	28.5°	3000	0.997	8.450	0.027	0.352
	32.5°	3000	1.149	11.322	0.036	0.326
TE2F rotor	22.5°	3000	0.876	5.846	0.019	0.420
	24.5°	3000	1.016	7.145	0.023	0.429
	26.5°	3000	1.118	8.597	0.027	0.411
	28.5°	3000	1.213	10.487	0.033	0.381
	32.5°	3000	1.421	14.845	0.047	0.341

